
Multiscale Euclidean Network Trajectories: Second-Moment Geometry, Attribution, and Change Points

Haruka Ezoe

Graduate School of Information Science and Technology
The University of Tokyo

Ryohei Hisano

Graduate School of Information Science and Technology
The University of Tokyo
The Canon Institute for Global Studies

Abstract

A central challenge in dynamic network analysis is to represent temporal evolution in a way that is both geometrically meaningful and statistically identifiable. One approach embeds a sequence of network snapshots as trajectories in a Euclidean space and relates these trajectories to node embeddings. In multilayer and unfolded spectral constructions, however, node embeddings and their underlying latent positions are identifiable only up to general linear transformations. Although this ambiguity preserves edge probabilities, it can distort geometry and invalidate distance based temporal comparisons at both the trajectory and node-levels.

We develop *Multiscale Euclidean Network Trajectories* (MENT), a framework for multiscale temporal trajectories based on *second-moment geometry*. By imposing an isotropic normalization on the anchor latent positions, we reduce the relevant ambiguity to orthogonal transformations and prevent distortion of the second-moment geometry. In this canonical representation, we define a trace variation distance and mode-wise variation distances along orthogonal directions, and use multidimensional scaling to obtain low-dimensional trajectories of time points at both global and mode-wise levels. The resulting trajectories support interpretation and inference. They admit mode-wise decompositions, support attribution of global and mode-wise temporal changes to nodes, and enable change point detection through 1D trajectories. We prove consistency of the proposed unfolded spectral embedding and of the induced temporal trajectories. Experiments on two synthetic and two real dynamic networks illustrate stable and interpretable recovery of temporal structure and show strong performance against existing change point detection baselines.

1 Introduction

Dynamic networks arise in social, communication, biological, and legal systems, where interactions evolve over time. A central goal in dynamic network analysis is not only to detect that a network has changed, but to describe *how* it changed and *which nodes* contributed to the change. Achieving this goal requires a geometry on time. Given a sequence of network snapshots, the key problem is to measure differences between time points in a way that reflects latent structural change and remains statistically identifiable from the observed graphs.

A first line of work represents network evolution through node embeddings. Spectral methods such as adjacency spectral embedding and dynamic extensions including unfolded adjacency spectral embedding (UASE) [1] and unfolded Laplacian spectral embedding [2] provide stable node-level representations across time. These methods are well suited for tracking local changes in node behavior. However, in their multilayer and unfolded spectral constructions, the dynamic latent factors are identifiable only up to a general linear transformation ($GL(d)$) [3]. This ambiguity is harmless for edge probabilities, which depend only on bilinear products, but it is not harmless for geometry: Euclidean norms, distances, and second-moment operators are not invariant under general linear transformations. As a result, unfolded embeddings do not by themselves define an identifiable geometry for comparing time points or attributing temporal change to nodes.

A complementary line of work represents temporal evolution at the level of entire network snapshots. Pairwise dissimilarities between time points can be embedded by classical multidimensional scaling (CMDS), yielding low-dimensional trajectories of network evolution [4–7]. Related network similarity methods, such as DeltaCon and NetSimile, also compare snapshots through global dissimilarity scores [8, 9]. These approaches provide concise summaries of *when* networks differ, but they are less suited to explaining *how* they differ. In particular, Euclidean Mirror summarizes temporal variation through maximum directional variation, which captures a dominant direction for each time pair comparison but does not provide a stable decomposition into persistent structural modes. Similarly, related work on change point detection includes spectral methods for dynamic graphs such as Laplacian Anomaly Detection (LAD), dynamic stochastic block models, graphon estimation methods, latent position and random dot product graph formulations and broader latent variable approaches [10–18]. This line of work is primarily concerned with detecting, localizing, or modeling changes over time, but it typically does not yield a geometry that decomposes those changes into persistent, interpretable components or attributes them to nodes. Thus, even when a change is detected, it often remains unclear *what* type of variation occurred and *which* nodes drove it.

In this paper, we introduce *Multiscale Euclidean Network Trajectories* (MENT), a framework for constructing interpretable temporal trajectories from an identifiable second-moment geometry. We first address the $GL(d)$ identifiability of multilayer and unfolded spectral constructions by imposing a canonical isotropic normalization on the shared anchor latent positions. This reduces the relevant ambiguity to a shared orthogonal transformation ($\mathbb{O}(d)$), which preserves second-moment geometry. In the resulting canonical representation, we define a trace variation distance for global temporal change and mode-wise variation distances along orthogonal directions induced by an aggregated second-moment operator. Applying CMDS to these distances yields low-dimensional trajectories of time points that summarize network evolution globally and by mode. The same geometry provides exact mode-wise and node-level decompositions, enabling attribution of temporal changes to nodes, and supports 1D change point localization along distinct temporal modes [5]. For a compact comparison with UASE, Euclidean Mirror, and LAD, see Table A.2 in Appendix A. Among these methods, only MENT combines an orthogonally identifiable second-moment geometry with full Euclidean realizability, exact mode decomposition, and stable node-level attribution.

We make three contributions. First, we identify $GL(d)$ identifiability as a fundamental obstruction to temporal geometry in unfolded spectral embeddings and show that an isotropic normalization restores the second-moment structure up to $\mathbb{O}(d)$ ambiguity. Second, we develop a multiscale framework based on trace variation and mode-wise variation distances, together with an orthogonal basis induced by the aggregated second-moment operator, and use it to construct temporal trajectories. Third, we show that these distances admit exact mode-wise decompositions, establish consistency for our proposed embedding and the induced temporal trajectories, and connect them to downstream tasks that include attribution and change point detection.

2 Setup and Geometric Problem

We observe a dynamic network over time $\mathcal{T} = \{1, \dots, T\}$ with adjacency matrices $\mathbf{A}(t) \in \mathbb{R}^{n \times n}$ at each $t \in \mathcal{T}$, where n denotes the number of nodes. Assuming that an underlying structure governs the dynamic network, our goal is to (i) construct a representation of the underlying temporal evolution and (ii) estimate it from the observed snapshots. We consider a model in line with multilayer random dot product graph models [3, 1], where edge probabilities are determined by inner products of node specific latent positions. We present a full generation process formulation in Appendix B.

Generative model: At the population level, the underlying structure is modeled via $(\chi, \{\phi(t)\}_{t \in \mathcal{T}}) \in L^2(\Omega; \mathbb{R}^{d(T+1)})$, where anchor χ captures the time-invariant structure, dynamic $\phi(t)$ captures the time-varying structure at time t , and d denotes the latent space dimension. At the finite sample level, the anchor and dynamic latent position matrices $\mathbf{X}, \mathbf{Y}(t) \in \mathbb{R}^{n \times d}$ have rows corresponding to the n nodes, which are i.i.d. copies of χ and $\phi(t)$, respectively. We also assume $\phi(t) = \mathbf{G}(t)^\top \chi$ a.s. for a symmetric matrix $\mathbf{G}(t) = \mathbf{G}(t)^\top$ to model undirected network. Using this, edges are generated independently via

$$\mathbf{P}(t) = \mathbf{X}\mathbf{Y}(t)^\top \in \mathbb{R}^{n \times n}, \quad \mathbf{A}_{ij}(t) \sim \text{Bernoulli}(\mathbf{P}_{ij}(t)) \quad (i < j).$$

At the latent level, the unfolded probability matrix factors are as follows:

$$\mathbf{P} = [\mathbf{P}(1) \mid \cdots \mid \mathbf{P}(T)] = \mathbf{X}\mathbf{Y}^\top \in \mathbb{R}^{n \times nT},$$

where $\mathbf{Y} \in \mathbb{R}^{nT \times d}$ stacks the matrices $\mathbf{Y}(t)$. This completes the generation process.

Population temporal trajectory: To represent the underlying temporal evolution based on random vectors $\{\phi(t)\}_{t \in \mathcal{T}}$, we construct a low-dimensional Euclidean embedding of time, following Athreya et al. [4]. Given a pairwise dissimilarity $d(\cdot, \cdot)$ of random vectors and the corresponding dissimilarity matrix

$$\mathbf{D}_\phi = [d(\phi(t), \phi(s))]_{t, s \in \mathcal{T}},$$

we map the time point into Euclidean space using CMDS [7, 4]. If we write

$$\mathbf{D}_\phi^{(2)} = [d(\phi(t), \phi(s))^2]_{t, s \in \mathcal{T}}, \quad \mathbf{J} = \mathbf{I}_T - \frac{1}{T}\mathbf{1}\mathbf{1}^\top, \quad \mathbf{E}_\phi = -\frac{1}{2}\mathbf{J}\mathbf{D}_\phi^{(2)}\mathbf{J} \in \mathbb{R}^{T \times T},$$

then the matrix \mathbf{E}_ϕ is the centered Gram matrix associated with the pairwise dissimilarities. CMDS yields c -dimensional embedding $\psi(t) \in \mathbb{R}^c$ such that

$$\|\psi(t) - \psi(s)\| \approx d(\phi(t), \phi(s)), \quad t, s \in \mathcal{T}.$$

The above becomes an identity when \mathbf{E}_ϕ is positive semidefinite and $c = \text{rank}(\mathbf{E}_\phi)$. This enables the low-dimensional Euclidean trajectory to effectively summarize the underlying temporal evolution.

Estimation: Following Athreya et al. [4], we construct a consistent estimator based on node embeddings derived from the observed networks. A standard embedding method under the multilayer setting is the UASE [1, 3]¹. We define the unfolded adjacency matrix using column concatenation and compute a rank- d truncated singular value decomposition:

$$\mathbf{A} = [\mathbf{A}(1) \mid \mathbf{A}(2) \mid \cdots \mid \mathbf{A}(T)] \in \mathbb{R}^{n \times nT}, \quad \mathbf{A} \approx \hat{\mathbf{U}}\hat{\mathbf{\Sigma}}\hat{\mathbf{V}}^\top,$$

where $\hat{\mathbf{V}}(t) \in \mathbb{R}^{n \times d}$ denotes the block corresponding to time t . Then, UASE defines the node embedding at time t as

$$\hat{\mathbf{Y}}_{\text{orig}}(t) = \hat{\mathbf{V}}(t)\hat{\mathbf{\Sigma}}^{1/2} \in \mathbb{R}^{n \times d}, \quad t \in \mathcal{T},$$

which recovers latent positions up to a general linear transformation [3]. However, this ambiguity obstructs the consistent estimation of the dissimilarity, as we explain further in Section 3.1. Thus, a node embedding method tailored to the proposed second-moment geometry is essential.

Building on this setup, our contribution is to define a canonical second-moment geometry, together with trace and mode-wise variation distances, that yields statistically identifiable temporal trajectories. This geometry also provides the structure needed for multiscale decomposition, node attribution, and change point localization.

Throughout the paper, all stochastic $\mathcal{O}(\cdot)$ a.s. bounds are understood in the overwhelming probability sense specified in Appendix A: for every $A > 0$, there exist a constant $c_A > 0$ such that, $\Pr\{|X_n| \leq c_A f(n)\} \geq 1 - n^{-A}$ for all sufficiently large n . Since these failure probabilities are summable for any fixed $A > 1$, the bounds also imply the corresponding usual almost sure $\mathcal{O}(\cdot)$ statements by Borel–Cantelli.

¹An alternative is to apply adjacency spectral embedding separately to each snapshot as in Athreya et al. [4]. However, this requires post hoc orthogonal alignment across time (i.e., Procrustes alignment), which can obscure genuine temporal variation by enforcing excessive similarity between snapshots.

3 Multiscale Second-moment Geometry on Time

3.1 Canonicalization of Second-moment Geometry and Modified UASE

The key geometric issue in multilayer and unfolded spectral construction is that the underlying latent factorization is rectangular rather than square. Unlike square random dot product graph factorizations of a single snapshot, this representation is not identifiable up to the orthogonal transformation. Specifically, for any $\mathbf{G} \in \text{GL}(d)$,

$$\mathbf{P} = \mathbf{X}\mathbf{Y}^\top = (\mathbf{X}\mathbf{G})(\mathbf{Y}\mathbf{G}^{-\top})^\top.$$

This general linear transformation leaves the edge probabilities unchanged. Consequently, the population latent object is only identifiable up to a general linear transformation [3]. We summarize this fact in the following proposition.

Proposition 3.1 (GL(d) identifiability). *For any $\mathbf{G} \in \text{GL}(d)$, the population objects $(\chi, \{\phi(t)\}_{t \in \mathcal{T}})$ and $(\mathbf{G}^\top \chi, \{\mathbf{G}^{-1}\phi(t)\}_{t \in \mathcal{T}})$ induce the same distribution on the observed dynamic network.*

This identifiability particularly matters when the temporal geometry is based on second-moments of latent displacements, which is the main operator in this paper. For $t, s \in \mathcal{T}$, define

$$\mathbf{M}_\phi(t, s) := \mathbb{E}[(\phi(t) - \phi(s))(\phi(t) - \phi(s))^\top],$$

where $\mathbf{M}_\phi(t, s) \in \mathbb{R}^{d \times d}$ is the population second-moment matrix of the displacement $\phi(t) - \phi(s)$. To illustrate this, under the transformation $\phi(t) \mapsto \mathbf{G}^{-1}\phi(t)$, the population second-moment matrix transforms as $\mathbf{M}_\phi(t, s) \mapsto \mathbf{G}^{-1}\mathbf{M}_\phi(t, s)\mathbf{G}^{-\top}$. Thus second-moment quantities, such as its trace and spectral norm, and hence the distances and temporal trajectories built from them, are distorted under the general linear transformations. Equivalent latent representations can therefore induce different temporal geometries, unless identifiability is restored up to orthogonal transformations.

To obtain a geometrically meaningful and statistically identifiable framework, we study a canonical parameterization determined by the second-moment of the anchor random vector. This is set using the following assumption.

Assumption 3.2 (Anchor isotropy). The anchor random vector satisfies $\mathbb{E}[\chi\chi^\top] = \mathbf{I}_d$.

Assumption 3.2 is a normalization rather than a modeling restriction. This means that whenever $\mathbb{E}[\chi\chi^\top]$ is invertible, we may whiten the anchor random vector to obtain an equivalent parameterization that satisfies anchor isotropy (Proposition C.1). Under this canonical geometry, the relevant identifiability is restored from general linear transformations up to orthogonal transformations, which preserve the second-moment structure.

This canonicalization also highlights that the original UASE estimator includes distortion because of its GL(d) ambiguity. This motivates us to develop a new estimator. We write the new estimator, modified UASE, as follows:

$$\hat{\mathbf{Y}}_{\text{mod}}(t) := \frac{1}{n^{1/2}} \hat{\mathbf{V}}(t) \hat{\mathbf{\Sigma}} \in \mathbb{R}^{n \times d}, \quad t \in \mathcal{T}.$$

Unlike the original UASE, our modified UASE recovers latent positions up to an orthogonal transformation shared across all snapshots. We summarize this in the following Theorem.

Theorem 3.3 (Modified UASE under canonical geometry). *Assume Assumption 3.2 holds. Then there exists a possibly random orthogonal matrix $\mathbf{W} \in \mathbb{O}(d)$ such that*

$$\sup_{t \in \mathcal{T}} \left\| \hat{\mathbf{Y}}_{\text{mod}}(t) - \mathbf{Y}(t)\mathbf{W} \right\|_2 = \mathcal{O}(\log n) \quad a.s.$$

Theorem 3.3 is the key recovery statement that we use throughout the paper. Although the bound $\mathcal{O}(\log n)$ diverges in absolute terms, it is negligible relative to the typical $\mathcal{O}(n^{1/2})$ scale of the latent position matrices [19], and therefore corresponds to an asymptotically vanishing relative error. Because orthogonal transformations preserve second-moment quantities and the induced distances, this resolves the geometric incompatibility caused by GL(d) ambiguity and provides the basis of our multiscale temporal geometry. The consequences of omitting this modification are illustrated numerically in the experiments in Section 4.

3.2 Multiscale Second-moment Geometry and Interpretation

We now use the second-moment operator to build a multiscale description of temporal variation. In previous studies, researchers focused on using the square root of the spectral norm of the second-moment matrix which they called the maximum directional variation, which summarizes temporal change through the single most variable direction [4]². This quantity is useful as a one-direction summary, but it has two limitations in our setting. First, it retains only the dominant mode of variation and is therefore not suited to a multiscale decomposition of temporal change. Second, distances on a finite set do not generally admit an exact Euclidean realization, unlike our proposed distances. Further discussion, including a counterexample, is in Appendix F.

Therefore, we move from the spectral norm summary of Athreya et al. [4] to distances built from the full second-moment operator. We define a global trace variation distance and mode-wise variation distances along canonical orthogonal directions. These distances preserve the geometric invariance needed for statistical identifiability while retaining the directional information required for meaningful mode decomposition.

Specifically, we introduce a trace variation distance and mode-wise variation distances along orthogonal directions.

Definition 3.4 (Trace and mode-wise variation distances). For $t, s \in \mathcal{T}$, define the trace variation distance as

$$d_{\text{TV}}(\phi(t), \phi(s)) := (\text{tr } \mathbf{M}_\phi(t, s))^{1/2} = \|\phi(t) - \phi(s)\|_{L^2(\Omega; \mathbb{R}^d)}.$$

Given an orthonormal basis $\{\mathbf{u}_k\}_{k=1}^d$, define the k th mode-wise variation distance as

$$d_k(\phi(t), \phi(s)) := (\mathbf{u}_k^\top \mathbf{M}_\phi(t, s) \mathbf{u}_k)^{1/2} = \|(\phi(t) - \phi(s))^\top \mathbf{u}_k\|_{L^2(\Omega; \mathbb{R})}.$$

Unlike maximum directional variation, both $d_{\text{TV}}(\cdot, \cdot)$ and $d_k(\cdot, \cdot)$ are Hilbertian distances. Hence, for any finite set of time points, the associated centered Gram matrices are positive semidefinite and the resulting population trajectories exactly realize these distances. The central fact is that trace variation decomposes exactly across modes, which we summarize in the following theorem.

Theorem 3.5 (Orthogonal decomposition of trace variation). *For the distances defined in Definition 3.4, the following holds.*

$$d_{\text{TV}}(\phi(t), \phi(s))^2 = \sum_{k=1}^d d_k(\phi(t), \phi(s))^2.$$

This identity makes it clear that the mode-wise distances do not introduce a competing notion of change; rather, they decompose the global variation into orthogonal components.

To further exploit this idea and provide a specific example of the choice of orthonormal basis, we define an aggregated second-moment operator. Let $\mathcal{S} \subseteq \mathcal{T} \times \mathcal{T}$ be a user-specified collection of time pairs, and define

$$\mathcal{M}_\phi := \sum_{(t,s) \in \mathcal{S}} \mathbf{M}(\phi(t), \phi(s)) \in \mathbb{R}^{d \times d}.$$

Assuming that this operator has separated eigenvalues, let $\{\mathbf{u}_k\}_{k=1}^d$ denote its orthonormal eigenvectors ordered by decreasing eigenvalue. This yields an orthonormal basis that describes the orthogonal structural directions. The following proposition shows that the aggregated operator orders modes by their cumulative contribution to temporal variation over the selected time pairs.

Proposition 3.6 (Mode importance under aggregation). *For each $k \in \{1, \dots, d\}$,*

$$\lambda_k(\mathcal{M}_\phi) = \sum_{(t,s) \in \mathcal{S}} d_k(\phi(t), \phi(s))^2.$$

It is worth noting that by the variational characterization of eigenvalues, the leading mode maximizes the total squared mode-wise variation distances over \mathcal{S} , and subsequent modes also do this subject

²To be precise, their maximum directional variation includes a Procrustes alignment factor because they did not use a multilayer representation.

to orthogonality. Thus trace variation provides a global measure of change, whereas the mode-wise distances resolve that change into interpretable orthogonal components.

Using this setup, we can finally define multiscale low-dimensional temporal trajectories that are geometrically meaningful and statistically identifiable. We obtain the definition via CMDS. For trace and mode-wise distances, we define

$$\mathbf{D}_{\text{TV}} = [d_{\text{TV}}(\phi(t), \phi(s))]_{t,s \in \mathcal{T}}, \quad \mathbf{D}_k = [d_k(\phi(t), \phi(s))]_{t,s \in \mathcal{T}}, \quad k \in \{1, \dots, d\}.$$

Applying CMDS yields population trajectories $\psi_{\text{TV}}(t), \psi_k(t) \in \mathbb{R}^c$. These provide a global summary of temporal evolution and a mode-wise decomposition of temporal variation, respectively.

3.3 Estimation of Multiscale Temporal Trajectories

Thus far, we have described our framework at the population level. Next, we turn to estimation. The temporal variation of the population random vectors can be estimated using modified UASE $\hat{\mathbf{Y}}_{\text{mod}}(t) \in \mathbb{R}^{n \times d}$ defined in Section 3.1. To achieve this, we introduce an estimate of the population second-moment matrix and define corresponding distances $\hat{d}_{\text{TV}}(\cdot, \cdot)$ and $\hat{d}_k(\cdot, \cdot)$. Specifically, we define the second-moment matrix of embedding displacements as

$$\hat{\mathbf{M}}_{\hat{\mathbf{Y}}}(t, s) := \frac{1}{n} (\hat{\mathbf{Y}}_{\text{mod}}(t) - \hat{\mathbf{Y}}_{\text{mod}}(s))^\top (\hat{\mathbf{Y}}_{\text{mod}}(t) - \hat{\mathbf{Y}}_{\text{mod}}(s)), \quad t, s \in \mathcal{T}.$$

Based on $\hat{\mathbf{M}}_{\hat{\mathbf{Y}}}(t, s)$, we define estimated distances $\hat{d}_{\text{TV}}(\cdot, \cdot)$ and $\hat{d}_k(\cdot, \cdot)$ with an orthonormal basis $\{\hat{\mathbf{u}}_k\}_{k=1}^d$ analogously to their population counterparts, yielding estimated distance matrices $\hat{\mathbf{D}}_{\text{TV}}, \hat{\mathbf{D}}_k \in \mathbb{R}^{T \times T}$ and trajectories $\hat{\psi}_{\text{TV}}, \hat{\psi}_k \in \mathbb{R}^c$. Because orthogonal transformations preserve second-moment quantities and the induced distances, the estimated distances are consistent with their population counterparts, and this consistency propagates through CMDS to the resulting trajectories.

We can prove the consistency of the estimated trajectories by first establishing the distance concentration results for trace and mode-wise variation distances, and then analyzing how CMDS propagates these errors to trajectory estimates. We further characterize how the amplification of the distance estimation errors during this propagation depends on the population structure conditions. We present further details in Appendices E and G. In the following theorem, we summarize the consistency results.

Theorem 3.7 (Consistency of trace and mode-wise trajectories). *Assume that Assumption 3.2 holds and that the node embeddings are obtained via modified UASE. Let \mathbf{E}_{TV} and \mathbf{E}_k be the centered Gram matrices associated with the population distances, and suppose that each is a positive semidefinite matrix of rank c . Then, there exists a possibly random orthogonal matrix $\mathbf{R}_{\text{TV}} \in \mathbb{O}(c)$ such that*

$$\sum_{t=1}^T \|\hat{\psi}_{\text{TV}}(t) - \mathbf{R}_{\text{TV}} \psi_{\text{TV}}(t)\|^2 = O\left(\frac{(\log n)^2}{n}\right) \quad a.s.$$

Moreover, for any fixed $k \in \{1, \dots, d\}$, there exists a possibly random orthogonal matrix $\mathbf{R}_k \in \mathbb{O}(c)$ such that

$$\sum_{t=1}^T \|\hat{\psi}_k(t) - \mathbf{R}_k \psi_k(t)\|^2 = O\left(\frac{(\log n)^2}{n}\right) \quad a.s.$$

Theorem 3.7 shows that the proposed estimated trajectories consistently recover the population trajectories, both globally through trace variation and directionally through the mode-wise decomposition.

3.4 Node Attribution and Change Point Detection

Node attribution: The proposed second-moment geometry admits the principled node attributional interpretation of the temporal trajectories. Both trace variation and mode-wise variation distances admit node-level decompositions. Consequently, displacements in both the trace trajectory and mode-wise trajectories can be traced back to the nodes that drive them. Because the following arguments holds for arbitrary embeddings, we write $\hat{\mathbf{Y}}(t)$ instead of $\hat{\mathbf{Y}}_{\text{mod}}(t)$.

For $t, s \in \mathcal{T}$, we first define the node embedding displacements

$$\hat{\Delta}_i(t, s) := \hat{\mathbf{Y}}_{i:}(t) - \hat{\mathbf{Y}}_{i:}(s) \in \mathbb{R}^d, \quad i \in \{1, \dots, n\}.$$

Then we can show that the exact decomposition holds at the distance level as follows,

$$\begin{aligned} \hat{d}_{\text{TV}}(\hat{\mathbf{Y}}(t), \hat{\mathbf{Y}}(s))^2 &= \frac{1}{n} \sum_{i=1}^n \|\hat{\Delta}_i(t, s)\|^2, \\ \hat{d}_k(\hat{\mathbf{Y}}(t), \hat{\mathbf{Y}}(s))^2 &= \frac{1}{n} \sum_{i=1}^n \langle \hat{\Delta}_i(t, s), \hat{\mathbf{u}}_k \rangle^2, \quad k \in \{1, \dots, d\}. \end{aligned}$$

Thus, the trace variation distance measures the average squared magnitude of node-level change, whereas each mode-wise distance isolates the average squared change along the orthogonal directions $\{\hat{\mathbf{u}}_k\}_{k=1}^d$. Because of the approximation error bound of CMDS, this attributional structure is inherited by the temporal trajectories themselves. This leads to the following theorem.

Theorem 3.8 (Node-level to trajectory-level control for trace and mode-wise trajectories). *Let $\hat{\mathbf{E}}_{\text{TV}}$ and $\hat{\mathbf{E}}_k$ be the centered Gram matrices associated with the estimated distances, and suppose that each has at least c positive eigenvalues. Then, for any $t, s \in \mathcal{T}$,*

$$\left| \|\hat{\psi}_{\text{TV}}(t) - \hat{\psi}_{\text{TV}}(s)\|^2 - \frac{1}{n} \sum_{i=1}^n \|\hat{\mathbf{Y}}_{i:}(t) - \hat{\mathbf{Y}}_{i:}(s)\|^2 \right| \leq 2 \left(\sum_{i=c+1}^T \lambda_i(\hat{\mathbf{E}}_{\text{TV}})^2 \right)^{1/2}.$$

Moreover, for any fixed $k \in \{1, \dots, d\}$ and any $t, s \in \mathcal{T}$,

$$\left| \|\hat{\psi}_k(t) - \hat{\psi}_k(s)\|^2 - \frac{1}{n} \sum_{i=1}^n \langle \hat{\mathbf{Y}}_{i:}(t) - \hat{\mathbf{Y}}_{i:}(s), \hat{\mathbf{u}}_k \rangle^2 \right| \leq 2 \left(\sum_{i=c+1}^T \lambda_i(\hat{\mathbf{E}}_k)^2 \right)^{1/2}.$$

Theorem 3.8 shows that displacements in the trace trajectory recovers aggregate node-level contributions, up to a residual determined by the discarded CMDS spectrum. It also provides the analogous result for mode-wise trajectories. Together, these theorems give the trajectories a precise attributional interpretation. The above theorem is pairwise, which provides a straightforward interpretation, but we can derive a tighter bound for the aggregated version over all time pairs. We show this in Theorem H.3 and H.4 in the Appendix. Furthermore, we can derive a related attribution statement for the maximum directional variation distance considered in previous study [4] (Theorem F.5). However, in Appendix F.3, we highlight that this attribution is substantially less precise than that obtained in this section because it depends on a direction optimized separately for each time pair and therefore does not yield a comparably sharp bound nor admits temporal comparison.

Change point detection: These low-dimensional temporal trajectories also lead naturally to inference on temporal events. In particular, once a trace variation or mode-wise trajectory has been estimated, change point detection can be conducted directly on that trajectory.

For a 1D estimated trajectory $\hat{\psi}(t) \in \mathbb{R}$, define the estimator

$$\hat{t} \in \arg \min_{k \in \mathcal{K}} \min_{\theta} \sum_{t=1}^T (\hat{\psi}(t) - \Psi(t; k, \theta))^2,$$

where $\Psi(t; k, \theta)$ is a piecewise parametric trajectory with candidate knot $k \in \mathcal{K} \subseteq \mathcal{T}$. In particular, piecewise constant models encode 0th order changes and piecewise linear models encode 1st order changes [5]. For a 1D population trajectory $\psi(t) \in \mathbb{R}$, let

$$Q(k) := \min_{\theta} \sum_{t=1}^T (\psi(t) - \Psi(t; k, \theta))^2$$

and let $t^* \in \arg \min_{\mathcal{K}} Q(k)$ denote the population change point. Under the uniqueness and separation assumptions stated in Appendix H.4, the localization error of the estimated change point is controlled by the trajectory estimation error.

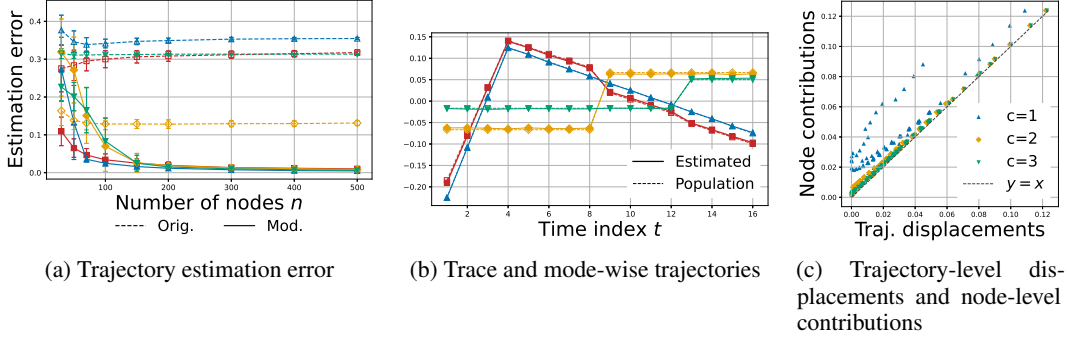


Figure 1: Trajectory recovery and node attribution results on Dataset 1. Panel (a) shows trajectory estimation error for the trace and mode-wise trajectories, comparing the proposed modified UASE with the original UASE. Panel (b) compares the estimated and population trajectories under the modified UASE for one realization of the dataset where the number of nodes is 500. Panel (c) compares displacements of the trace trajectory with aggregated node-level contributions for each time pair (t, s) with $t < s$ using the same data as (b). In panels (a) and (b), the trace variation is depicted in red (square markers), and the three mode-wise components are depicted in blue (triangle-up), orange (diamond), and green (triangle-down), respectively.

Theorem 3.9 (Change point localization). *Under the uniqueness and separation assumptions,*

$$|\hat{t} - t^*| \leq \frac{4}{\alpha D(\theta^*)} \left\{ \left(\sum_{t=1}^T (\hat{\psi}(t) - \psi(t))^2 \right)^{1/2} + Q(t^*)^{1/2} \right\}^2,$$

where, $D(\theta^*)$ is a nonnegative function and α is a positive constant, both of which are determined by the parametric trajectory model.

Theorem 3.9 shows that, once the temporal trajectories are consistently estimated, change point localization can be performed on them. In particular, the trace trajectory detects global structural changes, whereas the mode-wise trajectories allow changes of different orders to be localized along distinct orthogonal directions of temporal evolution.

4 Experiments

We evaluate MENT on two synthetic datasets with known latent structure and change points, and on two real-world datasets. One is a U.S. court opinion citation network [20] and the other is Enron e-mail network [21, 22]. The experiments test four claims: (i) unresolved $GL(d)$ ambiguity distorts temporal geometry, (ii) our proposed embedding consistently recovers trace and mode-wise trajectories, (iii) trajectory-level displacements admit faithful node-level attribution and (iv) mode-wise trajectories improve localization of heterogeneous change points. Both synthetic datasets are dynamic Stochastic Block Models (SBMs) [12] with three equal communities and three orthogonal latent modes. Dataset 1 has one change point per mode, while Dataset 2 has multiple mode specific change points. Full details and additional validation are given in Appendix I.

Synthetic Dataset 1: Figure 1 validates the geometric and attribution claims in a controlled setting. Panel (a) shows that trajectories estimated from the proposed modified UASE converge to their population counterparts for both trace and mode-wise distances. In contrast, the original UASE exhibits a persistent non vanishing bias, confirming that unresolved $GL(d)$ ambiguity distorts the temporal geometry. This is the consequence of Theorems 3.3 and 3.7. Panel (b) shows that the recovered mode-wise trajectories are nearly identical to the population trajectories, and isolate the planted 0th and 1st order changes, whereas the trace trajectory aggregates them into a global summary (Section 3.2). Panel (c) verifies the node attribution identity: trajectory-level displacements closely match the corresponding aggregate node-level contributions for each time pair (Theorem 3.8).

Synthetic Dataset 2: Next, we evaluated the proposed framework on a change point detection task. We used the more challenging synthetic Dataset 2, in which six ground-truth change points occur

Method	$K = 3$		$K = 6$		$K = 9$	
	F1	MAE	F1	MAE	F1	MAE
DeltaCon	0.447	2.09	0.513	2.40	0.579	2.29
LAD	0.667	0.73	0.833	1.26	0.688	1.89
HCDL	0.322	2.42	0.480	2.21	0.532	2.15
Mirror	0.664	0.01	0.573	1.56	0.512	2.08
Two-stage	0.667	0.00	0.815	1.04	0.692	2.07
MENT	0.667	0.00	0.965	0.10	0.800	1.00

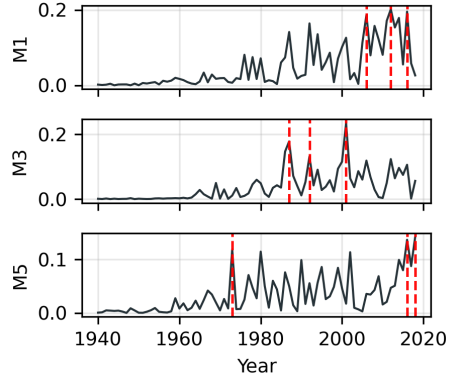


Figure 2: Results of change point detection on synthetic and real world data. Left: F1 and timing MAE across competing methods on Dataset 2. Right: Mode-wise level change point score plots on the U.S. court citation dataset. Dashed red line shows detected change points.

at $t \in \{11, 21, 31, 41, 51, 61\}$ across three modes with heterogeneous signal strengths and change orders. We compared the proposed method against DeltaCon [8], LAD [10], HCDL [16], Euclidean Mirror [4], and the very recently proposed two-stage method of Wang et al. [15]. For each method, we ranked the candidate change points and evaluated the top K performance for $K \in \{3, 6, 9\}$ using the F1 score and timing mean absolute error (MAE), averaged over 100 independent trials. For MENT, we fit a local linear trend model [23] for each mode k to the 1D trajectory $\hat{\psi}_k(t)$. This produces two complementary scores: $s_{k,t}^{(0)}$, which detects level shifts, and $s_{k,t}^{(1)}$, which detects slope changes and we fused the results using normalized scores (see Appendix I.7 for details). All methods are evaluated using the same matching tolerance, minimum separation rule, and top- K protocol. Method specific hyperparameters are tuned by grid search as detailed in Appendix I.7.

The left table in Figure 2 shows that the proposed method performs best overall across all three values of K (see Appendix Table I.3 for results with 95% confidence intervals). At $K = 3$, it matched the best baseline F1 while achieving perfect localization on matched detections. At $K = 6$, which equals the true number of change points, it achieved near perfect recovery (F1 = 0.965, timing MAE = 0.1), substantially outperforming all competitors. It also remained strongest at $K = 9$, where some degree of over selection is unavoidable. Among the competitors, LAD and the two-stage method were the most competitive but still missed weaker mode-specific events. Overall, these results support the claim that multiscale trajectories can improve detection in settings where distinct temporal events occur in different latent modes and are blurred by global summaries. Appendix I provides additional validation of distance recovery, basis sensitivity, trajectory recovery, attribution bounds, dimension robustness, and baseline comparisons.

Real-world interpretation of U.S. court citation dynamics: We conclude with a case study on the U.S. court opinion citation network dataset (See Appendix I.8 for details on how we constructed this dataset). The right panel of Figure 2 shows selected mode-wise level (0th order) change point score plots. In this case study, we focus on $s_{k,t}^{(0)}$ because level shifts correspond naturally to abrupt changes in the co-citation patterns. We also present the detailed node attribution tables in Appendix I.9.

The selected modes reveal several interpretable forms of citation reorganization. Mode 1 shows the broadest restructuring, with its strongest level shifts occurring from the mid-2000s to the mid-2010s. Its attributions separate a broad constitutional standards and rights or remedies neighborhood, including cases such as *City of Cleburne*, *Graham*, *Mapp*, and *Roper*, from a more procedure-specific criminal adjudication and post-conviction neighborhood, including *Stovall*, *Ker*, *Schlup*, and *Cronic*. Mode 3 is more concentrated. Its shifts around the late 1980s, early 1990s, and early 2000s organize Fourth Amendment and police litigation, including encounter, consent, automobile search, search incident, warrant review, detention, and qualified immunity cases. Mode 5 is broader, but provides a useful contrast: its peaks in 1973, 2016, and 2018 link constitutional claims against government action to doctrines governing reviewability, liability, remedies, and punishment. Taken together, the case study suggests that the learned trajectories recover structured shifts in citation patterns corresponding to recognizable doctrinal regimes rather than merely surfacing isolated high citation cases. We provide an additional real-world example using the Enron e-mail dataset in Appendix I.10.

5 Conclusion

We introduced a multiscale second-moment geometric framework for dynamic network trajectories called MENT that resolves the geometric distortion caused by $GL(d)$ identifiability in multilayer and unfolded spectral constructions. The resulting trace variation and mode-wise trajectories support mode decomposition, consistent recovery, node-level attribution, and change point localization, providing an interpretable geometric representation of temporal network evolution. All code accompanying this paper is hosted on <https://github.com/hisanor013/ment>.

6 Acknowledgements

We thank Yuki Takazawa, Ryoma Kondo, Kohei Miyaguchi, Tilmann Altwicker and Zhivko Taushanov for helpful discussions. R.H. is supported by JST FOREST Program (JPMJFR216Q), JST PRESTO Program (JPMJPR2469), Grant-in-Aid for Scientific Research (KAKENHI, JP24K03043), JSPS International Joint Research Program (JRP with SNSF: 20251501), and the UTEC-UTokyo FSI Research Grant Program.

References

- [1] Ian Gallagher, Andrew Jones, and Patrick Rubin-Delanchy. Spectral embedding for dynamic networks with stability guarantees. In *Advances in Neural Information Processing Systems*, volume 34, pages 10158–10170, 2021.
- [2] Haruka Ezoe, Hiroki Matsumoto, and Ryohei Hisano. Unfolded laplacian spectral embedding: A theoretically grounded approach to dynamic network representation. In *Proceedings of the International Conference on Machine Learning*, 2026.
- [3] Andrew Jones and Patrick Rubin-Delanchy. The multilayer random dot product graph. *arXiv*, 2020. arXiv:2007.10455.
- [4] Avanti Athreya, Zachary Lubbets, Youngser Park, and Carey E. Priebe. Euclidean mirrors and dynamics in network time series. *Journal of the American Statistical Association*, 120(550): 1025–1036, 2025.
- [5] Tianyi Chen, Zachary Lubbets, Avanti Athreya, Youngser Park, and Carey E. Priebe. Euclidean mirrors and first-order changepoints in network time series. *arXiv*, 2024. arXiv:2405.11111.
- [6] Runbing Zheng, Avanti Athreya, Marta Zlatic, Michael Clayton, and Carey E. Priebe. Dynamic networks clustering via mirror distance. *arXiv*, 2024. arXiv:2412.19012.
- [7] Ingwer Borg and Patrick J. F. Groenen. *Modern Multidimensional Scaling: Theory and Applications*. Springer Series in Statistics. Springer New York, 2 edition, 2005.
- [8] Danai Koutra, Neil Shah, Joshua T. Vogelstein, Brian Gallagher, and Christos Faloutsos. Delta-Con: A principled massive-graph similarity function with attribution. *ACM Transactions on Knowledge Discovery from Data*, 10(3):1–43, 2016.
- [9] Michele Berlingerio, Danai Koutra, Tina Eliassi-Rad, and Christos Faloutsos. NetSimile: A scalable approach to size-independent network similarity. *arXiv*, 2012. arXiv:1209.2684.
- [10] Shenyang Huang, Yasmeen Hitti, Guillaume Rabusseau, and Reihaneh Rabbany. Laplacian change point detection for dynamic graphs. In *Proceedings of the 26th ACM SIGKDD International Conference on Knowledge Discovery & Data Mining*, pages 349–358, 2020.
- [11] Monika Bhattacharjee, Moulinath Banerjee, and George Michailidis. Change point estimation in a dynamic stochastic block model. *Journal of Machine Learning Research*, 21(107):1–59, 2020.
- [12] Paul W. Holland, Kathryn Blackmond Laskey, and Samuel Leinhardt. Stochastic blockmodels: First steps. *Social Networks*, 5(2):109–137, 1983.

- [13] Zifeng Zhao, Li Chen, and Lizhen Lin. Change-point detection in dynamic networks via graphon estimation. *arXiv*, 2019. arXiv:1908.01823.
- [14] Farida Enikeeva and Olga Klopp. Change-point detection in dynamic networks with missing links. *Operations Research*, 73(5):2417–2429, 2025.
- [15] Fan Wang, Kyle Ritscher, Yik Lun Kei, Xin Ma, and Oscar Hernan Madrid Padilla. Change point localization and inference in dynamic multilayer networks. In *Proceedings of the International Conference on Learning Representations*, 2026.
- [16] Shintaro Fukushima and Kenji Yamanishi. Detecting hierarchical changes in latent variable models. In *Proceedings of the IEEE International Conference on Data Mining*, pages 1028–1033, 2020.
- [17] Rui Luo and Vikram Krishnamurthy. Fréchet-statistics-based change point detection in dynamic social networks. *IEEE Transactions on Computational Social Systems*, 11(2):2863–2871, 2023.
- [18] Yik Lun Kei, Jialiang Li, Hangjian Li, Yanzen Chen, and Oscar Hernan Madrid Padilla. Change point detection in dynamic graphs with decoder-only latent space model. *Transactions on Machine Learning Research*, 2025.
- [19] Terence Tao. *Topics in Random Matrix Theory*, volume 132 of *Graduate Studies in Mathematics*. American Mathematical Society, 2012. ISBN 978-0-8218-7430-1.
- [20] Free Law Project. Bulk legal data. <https://wiki.free.law/c/courtlistener/help/api/bulk-data/bulk-legal-data>, 2025. CourtListener bulk legal data; accessed 2026-04-04.
- [21] Bryan Klimt and Yiming Yang. The enron corpus: A new dataset for email classification research. In *Machine Learning: ECML 2004*, volume 3201 of *Lecture Notes in Computer Science*, pages 217–226. Springer, 2004.
- [22] William W. Cohen. Enron email dataset. <https://www.cs.cmu.edu/~enron/>, 2015. Hosted by Carnegie Mellon University; accessed 2026-04-24.
- [23] Skipper Seabold and Josef Perktold. Statsmodels: Econometric and statistical modeling with python. In *Proceedings of the 9th Python in Science Conference*, pages 92–96, 2010.
- [24] Maximilian Baum, Francesco S. Passino, and Axel Gandy. Doubly unfolded adjacency spectral embedding of dynamic multiplex graphs. *arXiv*, 2024. arXiv:2410.09810.
- [25] Mathieu Bastian, Sébastien Heymann, and Mathieu Jacomy. Gephi: An open source software for exploring and manipulating networks. In *Proceedings of the International AAAI Conference on Web and Social Media*, volume 3, pages 361–362, 2009.
- [26] Mark E. J. Newman. Modularity and community structure in networks. *Proceedings of the National Academy of Sciences*, 103(23):8577–8582, 2006.
- [27] Vincent D. Blondel, Jean-Loup Guillaume, Renaud Lambiotte, and Etienne Lefebvre. Fast unfolding of communities in large networks. *Journal of Statistical Mechanics: Theory and Experiment*, 2008(10):P10008, 2008.
- [28] Mathieu Jacomy, Tommaso Venturini, Sébastien Heymann, and Mathieu Bastian. ForceAtlas2, a continuous graph layout algorithm for handy network visualization designed for the gephi software. *PLoS ONE*, 9(6):e98679, 2014.
- [29] Jack Cushman, Matthew Dahl, and Michael Lissner. eyecite: A tool for parsing legal citations. *Journal of Open Source Software*, 6(66):3617, 2021.
- [30] Hiroki Matsumoto, Takahiro Yoshida, Ryoma Kondo, and Ryohei Hisano. Hypergraph change point detection using adapted cardinality-based gadgets: Applications in dynamic legal structures. In *Complex Networks & Their Applications XIII*, volume 1188 of *Studies in Computational Intelligence*, pages 3–15. Springer Cham, 2025.

- [31] Supreme Court of the United States. *Anderson v. Creighton*. Legal decision, 1987. 483 U.S. 635.
- [32] Tracey Maclin. The decline of the right of locomotion: The fourth amendment on the streets. *Cornell Law Review*, 75(6):1257–1336, 1989.
- [33] Supreme Court of the United States. *California v. Acevedo*. Legal decision, 1991. 500 U.S. 565.
- [34] Supreme Court of the United States. *Florida v. Bostick*. Legal decision, 1991. 501 U.S. 429.
- [35] Supreme Court of the United States. *Saucier v. Katz*. Legal decision, 2001. 533 U.S. 194.
- [36] Paul W. Hughes. Not a failed experiment: Wilson–Saucier sequencing and the articulation of constitutional rights. *University of Colorado Law Review*, 80(2):401–430, 2009.
- [37] Kit Kinports. The supreme court’s quiet expansion of qualified immunity. *Minnesota Law Review Headnotes*, 100(1):62–78, 2016.
- [38] Arne H. Schulz. Enron-mails for MySQL5 and R. <https://github.com/ahr85/enron>, 2012. Auxiliary employee metadata file E-Mails-updated.csv; accessed 2026-04-24.
- [39] U.S. Securities and Exchange Commission. Complaint: Jeffrey k. skilling and richard a. causey. <https://www.sec.gov/litigation/complaints/comp18582.htm>, 2004. Accessed 2026-04-24.
- [40] TIME. Chronology of a collapse. https://content.time.com/time/specials/packages/article/0,28804,2021097_2023262_2023247,00.html, 2002. Part of *Behind the Enron Scandal*; accessed 2026-04-24.
- [41] David Teather and Patrick Wintour. Enron executive may face perjury charge, says investigator. *The Guardian*, <https://www.theguardian.com/business/2002/feb/11/corporatefraud.enron1>, 2002. Published February 11, 2002; accessed 2026-04-24.
- [42] Sam Apple. John arnold made a fortune at enron. now he’s declared war on bad science. *WIRED*, <https://www.wired.com/2017/01/john-arnold-waging-war-on-bad-science/>, 2017. Published January 22, 2017; accessed 2026-04-24.
- [43] Robert K. Herdman. Testimony concerning recent events relating to enron corporation. U.S. Securities and Exchange Commission, <https://www.sec.gov/news/testimony/121201tsrkh.htm>, 2001. Before the Subcommittee on Capital Markets, Insurance and Government Sponsored Enterprises and the Subcommittee on Oversight and Investigation, Committee on Financial Services, U.S. House of Representatives, December 12, 2001; accessed 2026-04-24.
- [44] Jr. Hunt, Isaac C. Testimony concerning the enron bankruptcy, the functioning of energy markets and repeal of the public utility holding company act of 1935. U.S. Securities and Exchange Commission, <https://www.sec.gov/news/testimony/021302tsich.htm>, 2002. Before the Subcommittee on Energy and Air Quality, Committee on Energy and Commerce, U.S. House of Representatives, February 13, 2002; accessed 2026-04-24.
- [45] Matthew Goldstein. Court picks up the tab for enron witnesses. *TheStreet*, <https://www.thestreet.com/markets/court-picks-up-the-tab-for-enron-witnesses-10042313>, 2002. Published September 16, 2002; accessed 2026-04-24.
- [46] Yi Yu, Tengyao Wang, and Richard J. Samworth. A useful variant of the Davis–Kahan theorem for statisticians. *Biometrika*, 102(2):315–323, 2015.
- [47] Joel A. Tropp. An introduction to matrix concentration inequalities. *Foundations and Trends in Machine Learning*, 8(1–2):1–230, 2015.

A Appendix Guide and Notation

This appendix collects the technical material supporting the main text and situates the proposed framework within a broader probabilistic, geometric, and inferential context. Its purpose is fourfold. First, Appendices B, D, E, and F develop the general background for the paper. They introduce the generative model, formalize the Euclidean trajectory construction from temporal distances, and present the abstract error propagation strategy that carries distance estimation error through to trajectory estimation. These sections also clarify the limitations of the Euclidean Mirror approach of Athreya et al. [4], which is based on maximum directional variation (MV). Second, Appendices C, G, and H develop the main technical contributions of the paper in full detail. They formalize the canonical geometric parameterization, develop the trace trajectory and mode-wise trajectory framework, and prove the corresponding consistency, attribution, and change point results summarized in the main text. Third, Appendix I provides the additional experimental details needed to interpret and reproduce the empirical results, including data construction, implementation choices, and supplementary analyses for all four datasets: two synthetic datasets and two real world datasets. Finally, Appendix J contains the detailed proofs of the main propositions, theorems, and corollaries.

For ease of reference, we briefly summarize the contents of the appendix sections below.

Appendix B provides the model setup and clarifies the main inference targets. It specifies the generation model used throughout the paper, including the anchor latent positions, time-varying latent positions, edge probability matrices, and observed adjacency matrices. It also distinguishes the three layers of objects used in the analysis. They are population latent objects, finite sample latent variables, and estimated dynamic embeddings computed from observed graphs. Finally, it explains how these objects feed into the time pair distances, Euclidean trajectories, mode decompositions, node attributions, and change point detection procedures developed in later sections.

Appendix C develops the canonical geometric parameterization in full detail. It makes explicit the $GL(d)$ identifiability of multilayer and unfolded spectral construction, explains why general linear transformation ambiguity distorts second-moment geometry, and introduces anchor isotropy as a canonical normalization. This appendix supplements Section 3.1.

Appendix D formalizes the Euclidean trajectory construction as an abstract map from pairwise temporal dissimilarities to Euclidean coordinates of the time point via CMDS. This section separates the geometric part of the framework from the statistical estimation problem and introduces the general trajectory notation used later.

Appendix E develops the abstract error propagation framework that transfers uniform dissimilarity estimation error to consistency of the trajectories. These results are stated for a generic dissimilarity and serve as a common perturbation template for the concrete distances studied in the paper.

Appendix F clarifies the limitations of the Euclidean Mirror approach based on maximum directional variation (MV) [4]. It first records that MV based trajectories can be consistently estimated under our proposed framework. It then shows that MV remains limited for the multiscale goals of this paper because it summarizes each temporal comparison by a single dominant direction, can yield non Euclidean distance matrices over finite time sets, and provides weaker attribution due to time pair specific maximizing directions.

Appendix G supplements Section 3.3 in the main text. It establishes consistency of the multiscale trajectories by verifying the abstract propagation conditions for trace variation and mode-wise variation distances under modified UASE, and derives the corresponding trajectory consistency results.

Appendix H supplements Section 3.4. It develops the technical results supporting interpretation and inference. In particular, it proves the node-level decomposition identities and node-level to trajectory-level relations underlying attribution, introduces the piecewise trajectory models used for change point detection, and establishes the localization guarantees stated in the main text.

For convenience, Table A.1 collects the main notation used throughout the paper and appendix.

A.1 Comparison with Existing Methods

Table A.2 summarizes the methodological distinction between MENT and the closest related approaches. UASE [1] provides stable dynamic node embeddings, but its underlying latent positions

Table A.1: Summary of notation.

Notation	Meaning
n	Number of nodes.
T	Number of time points.
d	Latent dimension.
$\mathcal{T} = \{1, \dots, T\}$	Time point set.
$\chi \in L^2(\Omega; \mathbb{R}^d)$	Anchor random vector.
$\phi(t) \in L^2(\Omega; \mathbb{R}^d)$	Dynamic random vector at time t .
$\mathbf{X} \in \mathbb{R}^{n \times d}$	Anchor latent position matrix.
$\mathbf{Y}(t) \in \mathbb{R}^{n \times d}$	Dynamic latent position matrix at time t .
$\mathbf{A}(t) \in \mathbb{R}^{n \times n}$	Adjacency matrix at time t .
$\mathbf{P}(t) \in \mathbb{R}^{n \times n}$	Edge probability matrix at time t .
$\mathbf{P}(t) = \mathbf{X}\mathbf{Y}(t)^\top$	Probability matrix factorization.
$\hat{\mathbf{Y}}(t) \in \mathbb{R}^{n \times d}$	Dynamic node embeddings at time t .
$\text{GL}(d)$	General linear group.
$\mathbb{O}(d)$	Orthogonal group.
$\mathbf{M}_\phi(t, s) := \mathbf{M}(\phi(t), \phi(s))$	Population second-moment matrix of latent displacements between times t and s .
$\hat{\mathbf{M}}_{\mathbf{Y}}(t, s) := \hat{\mathbf{M}}(\mathbf{Y}(t), \mathbf{Y}(s))$	Finite sample second-moment matrix between times t and s .
$\hat{\mathbf{M}}_{\hat{\mathbf{Y}}}(t, s) := \hat{\mathbf{M}}(\hat{\mathbf{Y}}(t), \hat{\mathbf{Y}}(s))$	Second-moment matrix of embedding displacements between times t and s .
$d_{\text{TV}}(\mathbf{x}, \mathbf{y})$	Trace variation distance.
$d_k(\mathbf{x}, \mathbf{y})$	Mode-wise variation distance along direction \mathbf{u}_k .
\mathcal{M}	Population aggregated second-moment operator.
$\hat{\mathcal{M}}$	Finite sample aggregated second-moment operator.
\mathbf{u}_k	k th population canonical direction.
$\hat{\mathbf{u}}_k$	k th estimated canonical direction.
$\mathbf{D}^{(2)}$	Squared temporal dissimilarity matrix.
$\mathbf{J} = \mathbf{I}_T - \frac{1}{T}\mathbf{1}\mathbf{1}^\top$	Centering matrix.
$\mathbf{E} = -\frac{1}{2}\mathbf{J}\mathbf{D}^{(2)}\mathbf{J}$	Centered Gram matrix for CMDS.
c	Trajectory dimension.
$\psi(t) \in \mathbb{R}^c$	Population Euclidean trajectory coordinate at time t .
$\hat{\psi}(t) \in \mathbb{R}^c$	Estimated Euclidean trajectory coordinate at time t .
$\hat{\Delta}_i(t, s)$	Node-level embedding displacement between times t and s .
$\ \cdot\ _2$	Euclidean norm for vectors, operator norm for matrices.
$\ \cdot\ _F$	Frobenius norm.
$\ \cdot\ _{2 \rightarrow \infty}$	Two-to-infinity norm.
$\text{tr}(\cdot)$	Matrix trace.
$\lambda_k(\cdot)$	k th eigenvalue, in decreasing order when applicable.

are identifiable only up to a general linear transformation, which is insufficient for second-moment temporal geometry. LAD [10] provides a spectral anomaly score for change point detection, but does not construct an identifiable latent temporal geometry or node-level attribution. Euclidean Mirror [4] constructs time trajectories, but its maximum directional variation summary retains only pair specific dominant directions and therefore does not yield a stable mode-wise attribution geometry. MENT combines these ingredients by constructing an orthogonally identifiable second-moment geometry with exact mode decomposition, stable node-level attribution, and change point detection.

A.2 Probabilistic Notions and Asymptotic Conventions

This section introduces the probabilistic conventions used throughout the paper to quantify the reliability of random approximations. Because the objects studied in the paper are random and depend on finite samples, it is essential to specify a uniform notion of high probability control that is strong enough to support matrix perturbation arguments and geometric constructions.

Some results in the dynamic embedding literature are phrased using almost sure asymptotic notation [3, 1].

Table A.2: Comparison of dynamic network analysis methods.

Property	UASE	LAD	Euclidean Mirror	MENT
Stable node embeddings	Yes	Score	Trajectory	Yes
Identifiable second-moment geometry	No	No	Partial	Yes
Exact Euclidean realizability	No	No	Not in general	Yes
Exact mode decomposition	No	No	No	Yes
Stable node-level attribution	No	No	No (pair-specific)	Yes
Change point detection	Indirect	Yes	Yes	Yes

Definition A.1 ($\mathcal{O}(f)$ almost surely). Let $\{X_n\}$ be a sequence of random variables and let $f(n)$ be a positive function. We say that

$$|X_n| = \mathcal{O}(f(n)) \quad \text{almost surely}$$

if the following holds. For every $A > 0$, there exist a constant $c_A > 0$ and an integer N_A such that, for all $n \geq N_A$,

$$\Pr(|X_n| \leq c_A f(n)) \geq 1 - n^{-A}.$$

This definition provides a sequence of increasingly strong high probability bounds indexed by A . This formulation allows results stated in terms of almost sure rates to be combined cleanly with high probability perturbation arguments, which is essential when propagating error through spectral decompositions and geometric mappings such as CMDS.

B Model Setup and Inference Targets

This section establishes the probabilistic framework underlying the analysis in the main text. The model is standard in spirit and follows multilayer random dot product graph models and Euclidean Mirror constructions used in prior work on dynamic networks [3, 4]. Our contribution is not to introduce a new generative model, but to use this formulation to separate node-level latent structure from time level geometric objects, thereby clarifying which quantities are intrinsic targets of inference and how they enter the trajectory based analysis.

Definition B.1. Fix a finite set of time points $\mathcal{T} = \{1, \dots, T\}$ and a latent space dimension $d \in \mathbb{N}$. Let $(\Omega, \mathcal{F}, \mathbb{P})$ be a probability space. Let $(\chi, \{\phi(t)\}_{t \in \mathcal{T}}) \in L^2(\Omega; \mathbb{R}^{d(T+1)})$ satisfy $\chi^\top \phi(t) \in [0, 1]$ almost surely for all $t \in \mathcal{T}$.

For each $n \in \mathbb{N}$, consider a collection of random undirected graphs $\{G(t)\}_{t \in \mathcal{T}}$ on n vertices. Let $\mathbf{A}(t) \in \{0, 1\}^{n \times n}$ denote the adjacency matrix of $G(t)$.

Let $\mathbf{X} \in \mathbb{R}^{n \times d}$ and $\mathbf{Y}(t) \in \mathbb{R}^{n \times d}$ be random matrices whose rows are i.i.d. copies of χ and $\phi(t)$, respectively. We refer to \mathbf{X} as the anchor latent position matrix and to each $\mathbf{Y}(t)$ as the dynamic latent position matrix at time $t \in \mathcal{T}$.

For each $t \in \mathcal{T}$, define the edge probability matrix

$$\mathbf{P}(t) = \mathbf{X}\mathbf{Y}(t)^\top \in \mathbb{R}^{n \times n}.$$

Assume that, for each $t \in \mathcal{T}$, there exists a (possibly random) symmetric matrix $\mathbf{G}(t) \in \mathbb{R}^{d \times d}$, satisfying $\mathbf{G}(t) = \mathbf{G}(t)^\top$, such that

$$\mathbf{Y}(t) = \mathbf{X}\mathbf{G}(t) \quad \text{almost surely.}$$

Conditional on \mathbf{X} , $\{\mathbf{Y}(t)\}_{t \in \mathcal{T}}$, the edges are generated independently such that

$$\mathbf{A}_{ij}(t) \sim \text{Bernoulli}(\mathbf{P}_{ij}(t)) \quad (1 \leq i < j \leq n),$$

with

$$\mathbf{A}_{ji}(t) = \mathbf{A}_{ij}(t), \quad \mathbf{A}_{ii}(t) = 0.$$

Throughout the paper, we assume that χ and $\phi(t)$ have bounded support and that

$$\mathbb{E}[\chi\chi^\top], \quad \mathbb{E}[\phi(t)\phi(t)^\top]$$

are invertible for all $t \in \mathcal{T}$.

The population latent object $(\chi, \{\phi(t)\}_{t \in \mathcal{T}})$ is fixed and independent of n . It serves as the population-level temporal structure governing network evolution. The analysis therefore involves three layers of objects: the population latent object $(\chi, \{\phi(t)\}_{t \in \mathcal{T}})$, the finite sample latent variables \mathbf{X} and $\{\mathbf{Y}(t)\}_{t \in \mathcal{T}}$, and the estimated dynamic embeddings $\{\hat{\mathbf{Y}}(t)\}_{t \in \mathcal{T}}$ computed from the observed graphs with adjacency matrices $\{\mathbf{A}(t)\}_{t \in \mathcal{T}}$. The goal is not only to estimate latent positions at each time point, but to use their stable recovery to infer the geometry of temporal evolution. In the sections that follow, temporal trajectories, mode decompositions, node attributions, and change point procedures are all constructed from time-to-time dissimilarities computed from these latent or estimated embeddings.

C Canonical Geometry and Modified Unfolded Adjacency Spectral Embedding

This section provides the technical details behind the canonical geometry used in the main text. We make explicit how UASE is tied to a rectangular latent factorization, why this factorization yields $GL(d)$ rather than orthogonal identifiability, and how this ambiguity distorts second-moment geometry.

In prior work [24], a naive combination of the unfolded embedding with a Euclidean Mirror was considered. However, in light of the $GL(d)$ ambiguity described above, such a construction is not theoretically well-founded.

We then show that anchor isotropy selects a canonical population parameterization, restoring identifiability upto orthogonal transformations, and state the modified UASE construction and its orthogonal recovery guarantee.

C.1 $GL(d)$ identifiability and geometric distortion

Proposition 3.1 shows that the population latent objects under the multilayer factorization are intrinsically identifiable only up to a general linear transformation. This is a structural feature of the model and not an artifact of estimation. The $GL(d)$ ambiguity above is harmless for edge probabilities, since the bilinear products $\mathbf{X}\mathbf{Y}(t)^\top$ remain unchanged under paired transformations. For geometry based inference, however, the same ambiguity is consequential.

The difficulty is that second-moment quantities are typically not invariant under $GL(d)$. For $t, s \in \mathcal{T}$, define the finite sample second-moment matrix of latent displacements by

$$\hat{\mathbf{M}}_{\mathbf{Y}}(t, s) := \frac{1}{n} (\mathbf{Y}(t) - \mathbf{Y}(s))^\top (\mathbf{Y}(t) - \mathbf{Y}(s)).$$

Suppose an embedding procedure yields

$$\hat{\mathbf{Y}}(t) \approx \mathbf{Y}(t)\mathbf{G}$$

for some unknown $\mathbf{G} \in GL(d)$. Then the node-averaged squared Euclidean distance between times t and s satisfies

$$\frac{1}{n} \|\hat{\mathbf{Y}}(t) - \hat{\mathbf{Y}}(s)\|_F^2 \approx \frac{1}{n} \|(\mathbf{Y}(t) - \mathbf{Y}(s))\mathbf{G}\|_F^2 = \text{tr}(\mathbf{G}\mathbf{G}^\top \hat{\mathbf{M}}_{\mathbf{Y}}(t, s)).$$

Thus the induced distance is no longer measured in the canonical Euclidean geometry on \mathbb{R}^d , but in the warped metric

$$\langle \mathbf{u}, \mathbf{v} \rangle_{\mathbf{G}} = \mathbf{u}^\top (\mathbf{G}\mathbf{G}^\top) \mathbf{v}.$$

Unless \mathbf{G} is orthogonal, $\mathbf{G}\mathbf{G}^\top \neq \mathbf{I}_d$, and the resulting geometry is anisotropically distorted. Consequently, distance based summaries of temporal evolution, including Euclidean trajectories constructed from time pair dissimilarities, need not recover the intended population geometry if the latent representation is only identifiable up to $GL(d)$.

C.2 Anchor isotropy and canonical geometry

To eliminate this geometric distortion, we adopt a canonical parameterization defined by the second-moment of the anchor random vector, as summarized in Assumption 3.2. This assumption is a normalization rather than a modeling restriction. Whenever the anchor second-moment matrix is invertible, one may reparameterize the model by whitening the anchor random vector.

Proposition C.1 (Whitening to anchor isotropy). *Let $(\chi, \{\phi(t)\}_{t \in \mathcal{T}})$ be the population latent object defined in Definition B.1. Then there exists a population latent object $(\chi', \{\phi'(t)\}_{t \in \mathcal{T}})$ that satisfies Assumption 3.2 and induces the same distribution over the observed dynamic network.*

Proof. Since $E[\chi\chi^\top]$ is positive definite, define $\mathbf{G} := E[\chi\chi^\top]^{-1/2}$, so that $\mathbf{G}^\top E[\chi\chi^\top] \mathbf{G} = \mathbf{I}_d$.

Define the transformed variables

$$\chi' = \mathbf{G}^\top \chi, \quad \phi'(t) = \mathbf{G}^{-1} \phi(t).$$

Then

$$E[\chi' \chi'^\top] = \mathbf{G}^\top E[\chi\chi^\top] \mathbf{G} = \mathbf{I}_d,$$

so Assumption 3.2 holds.

By Proposition 3.1, the transformed latent object $(\chi', \{\phi'(t)\}_{t \in \mathcal{T}})$ induces the same distribution as the original one. \square

No data driven whitening is performed at the sample level. Rather, Assumption 3.2 fixes a canonical population parameterization. Under this parameterization, the identifiability is restored from general linear transformations upto orthogonal transformations, which preserve Euclidean second-moment geometry.

D Euclidean Trajectories from Time Pair Dissimilarities

This section formalizes the Euclidean trajectory construction used throughout the paper. The construction takes a matrix of pairwise temporal dissimilarities as input and applies classical multidimensional scaling (CMDS) to obtain a Euclidean embedding of the time point.

D.1 Abstract Dissimilarities and CMDS Trajectories

We begin by introducing an abstract notion of pairwise dissimilarity between random vectors and its finite sample analogue, which can also be used as an estimator.

Definition D.1. Let $\mathbf{x}, \mathbf{y} \in L^2(\Omega, \mathbb{R}^d)$. Let

$$d(\mathbf{x}, \mathbf{y}) \geq 0$$

denote a symmetric dissimilarity function that admits a finite sample analogue. For matrices $\mathbf{X}, \mathbf{Y} \in \mathbb{R}^{n \times d}$, let

$$\hat{d}(\mathbf{X}, \mathbf{Y})$$

denote the corresponding finite sample dissimilarity computed from finite samples.

At this stage, no specific structure is imposed on d beyond symmetry and the existence of a finite sample counterpart. Concrete choices of dissimilarity will be introduced in later sections.

Definition D.2 (Population dissimilarity matrices and trajectories [4, 5]). The population dissimilarity matrix induced by the population latent object $(\chi, \{\phi(t)\}_{t \in \mathcal{T}})$ is defined as

$$\mathbf{D}_\phi := [d(\phi(t), \phi(s))]_{t, s \in \mathcal{T}}.$$

Let $\mathbf{D}_\phi^{(2)}$ denote the elementwise square of \mathbf{D}_ϕ . Define the centering matrix

$$\mathbf{J} := \mathbf{I}_T - \frac{1}{T} \mathbf{1}\mathbf{1}^\top.$$

The population zero-skeleton trajectory (i.e., zero-skeleton mirror) [5], that is the Euclidean embedding of the time point, is obtained by CMDS. Specifically, let

$$\mathbf{E}_\phi = -\frac{1}{2}\mathbf{J}\mathbf{D}_\phi^{(2)}\mathbf{J},$$

and define $\psi(t) \in \mathbb{R}^c$ for $t = 1, \dots, T$ such that

$$(\psi(1), \dots, \psi(T))^\top = \arg \min_{\mathbf{Z} \in \mathbb{R}^{T \times c}} \|\mathbf{E}_\phi - \mathbf{Z}\mathbf{Z}^\top\|_F^2.$$

Definition D.3 (Finite sample dissimilarity matrices and estimated trajectories). The finite sample dissimilarity matrix induced by the latent position matrices $\mathbf{Y}(t)$ is defined as

$$\hat{\mathbf{D}}_{\mathbf{Y}} := [\hat{d}(\mathbf{Y}(t), \mathbf{Y}(s))]_{t,s \in \mathcal{T}}.$$

The estimated dissimilarity matrix induced by the dynamic embeddings $\hat{\mathbf{Y}}(t)$ is defined as

$$\hat{\mathbf{D}}_{\hat{\mathbf{Y}}} := [\hat{d}(\hat{\mathbf{Y}}(t), \hat{\mathbf{Y}}(s))]_{t,s \in \mathcal{T}}.$$

Let $\hat{\mathbf{D}}_{\hat{\mathbf{Y}}}^{(2)}$ denote the elementwise square of $\hat{\mathbf{D}}_{\hat{\mathbf{Y}}}$. The estimated zero-skeleton trajectory is obtained by CMDS as

$$(\hat{\psi}(1), \dots, \hat{\psi}(T))^\top = \arg \min_{\mathbf{Z} \in \mathbb{R}^{T \times c}} \|\hat{\mathbf{E}}_{\hat{\mathbf{Y}}} - \mathbf{Z}\mathbf{Z}^\top\|_F^2, \quad \hat{\mathbf{E}}_{\hat{\mathbf{Y}}} = -\frac{1}{2}\mathbf{J}\hat{\mathbf{D}}_{\hat{\mathbf{Y}}}^{(2)}\mathbf{J}.$$

D.2 Population and estimated trajectories

From this perspective, it is useful to view the overall construction as operating along two coupled axes: a horizontal axis capturing statistical approximation of dissimilarities, and a vertical axis capturing the geometric mirror map applied at either the population or embedding level. Schematically, this is represented as

$$\begin{array}{ccccc} \mathbf{D}_\phi & \longrightarrow & \hat{\mathbf{D}}_{\mathbf{Y}} & \longrightarrow & \hat{\mathbf{D}}_{\hat{\mathbf{Y}}} \\ & & \downarrow & & \downarrow \\ & & (\mathbf{E}_\phi, \psi) & & (\hat{\mathbf{E}}_{\hat{\mathbf{Y}}}, \hat{\psi}) \end{array}$$

The horizontal arrows correspond to statistical approximation steps, separating intrinsic temporal geometry from finite sample variability. The first approximation replaces the population dissimilarity matrix \mathbf{D}_ϕ with $\hat{\mathbf{D}}_{\mathbf{Y}}$, the dissimilarity matrix computed from the finitely sampled latent positions $\mathbf{Y}(t)$. This step isolates the effect of finite node sampling, in which expectations over the latent position distribution are replaced by empirical averages across nodes. Even if latent positions were directly observed, this approximation would still be required and introduces stochastic error that must be controlled uniformly over all time pairs.

The second approximation replaces $\hat{\mathbf{D}}_{\mathbf{Y}}$ with $\hat{\mathbf{D}}_{\hat{\mathbf{Y}}}$, the dissimilarity matrix computed from estimated dynamic embeddings. This step captures error arising from spectral estimation and from model nonidentifiability. In particular, without additional normalization, unfolded spectral embeddings recover latent positions only up to a general linear transformation, which can induce systematic distortion in distance based quantities. The canonical normalization ensures that this approximation preserves the relevant Euclidean geometry.

The vertical arrows correspond to purely geometric operations. Given any time pair dissimilarity matrix, population or sample, the centered Gram matrices \mathbf{E}_ϕ and $\hat{\mathbf{E}}_{\hat{\mathbf{Y}}}$ are obtained by applying the centering operator to the squared dissimilarities. The mirror embeddings ψ and $\hat{\psi}$ are then defined as low rank Euclidean realizations of these Gram matrices. No additional statistical assumptions enter at this stage.

Viewed in this way, all randomness and estimation error enter exclusively through the dissimilarity matrices, while the mirror construction itself is a deterministic geometric map. This separation allows consistency of the mirror to be established by first controlling dissimilarity estimation error and then propagating that error through multidimensional scaling.

E From Distance Estimation Error to Trajectory Error

This section develops a general framework for propagating error from estimated time pair dissimilarities to the resulting Euclidean trajectory embeddings. The analysis separates the problem into two stages: first, controlling the error of the estimated squared dissimilarity matrix, and second, propagating this matrix level error through the CMDS map. This abstraction allows the same perturbation argument to be reused for maximum directional variation, trace variation, and mode-wise variation distances.

The first stage concerns the accuracy of the estimated dissimilarity matrix. Since Euclidean trajectories are obtained by applying CMDS to the entire squared dissimilarity matrix, we begin by imposing uniform control over all time pairs, which will later be translated into Frobenius norm control. The following assumptions formalize two distinct sources of error that arise in estimation from observed graphs.

First, Assumption E.1 isolates the error arising from finite node sampling and averaging by treating the latent positions $\mathbf{Y}(t)$ as observed.

Assumption E.1. Let $f(n)$ be a positive function. Assume $d(\phi(t), \phi(s))$ is finite for all $t, s \in \mathcal{T}$, and

$$\sup_{t, s \in \mathcal{T}} \left| \hat{d}(\mathbf{Y}(t), \mathbf{Y}(s))^2 - d(\phi(t), \phi(s))^2 \right| = \mathcal{O}(f(n)) \quad \text{a.s.}$$

Next, Assumption E.2 captures the additional error introduced by edge sampling and estimating latent positions via dynamic embeddings.

Assumption E.2. Let $g(n)$ be a positive function.

$$\sup_{t, s \in \mathcal{T}} \left| \hat{d}(\hat{\mathbf{Y}}(t), \hat{\mathbf{Y}}(s))^2 - \hat{d}(\mathbf{Y}(t), \mathbf{Y}(s))^2 \right| = \mathcal{O}(g(n)) \quad \text{a.s.}$$

Together, these assumptions yield uniform control over all entries of the squared dissimilarity matrix. This entrywise control implies Frobenius norm control of the matrix error, which is required for CMDS.

Proposition E.3. Assume Assumptions E.1 and E.2. Then,

$$\left\| \hat{\mathbf{D}}_{\hat{\mathbf{Y}}}^{(2)} - \mathbf{D}_{\phi}^{(2)} \right\|_F = \mathcal{O}(f(n) + g(n)) \quad \text{a.s.}$$

Proposition E.3 provides a Frobenius norm control of the estimated squared dissimilarity matrix. Since CMDS is obtained by double centering this squared dissimilarity matrix to form a Gram matrix, such control implies a corresponding perturbation of the centered Gram matrix.

The second stage propagates the matrix-level error through the CMDS map that defines the Euclidean trajectory. We first establish a bound on the trajectory coordinates in terms of the dissimilarity matrix error using perturbation theory for CMDS, which relates perturbations of the centered Gram matrix to perturbations of the resulting trajectory. The purpose of this step is to make the leading constant explicit: although the trajectory error vanishes as the dissimilarity error tends to zero, its magnitude is governed by the conditioning of the population structure. We therefore isolate this dependence before combining with the Frobenius norm error bound from the first stage, which only specifies the convergence rate and does not track such constants.

Proposition E.4. Suppose that \mathbf{E}_{ϕ} has exactly r positive eigenvalues and that $\hat{\mathbf{E}}_{\hat{\mathbf{Y}}}$ has at least r positive eigenvalues. For $1 \leq a \leq b \leq r$, let $\psi(t; a, b), \hat{\psi}(t; a, b) \in \mathbb{R}^{b-a+1}$ denote the subvectors corresponding to the a -th through b -th coordinates of $\psi(t), \hat{\psi}(t) \in \mathbb{R}^r$, respectively.

Let λ_i denote the i -th largest eigenvalue of \mathbf{E}_{ϕ} . Define the spectral gap and the conditioning number

$$\text{gap}(a, b) := \min\{\lambda_{a-1} - \lambda_a, \lambda_b - \lambda_{b+1}\}, \kappa(a, b) := \frac{\lambda_a}{\min\{\text{gap}(a, b), \lambda_b\}}$$

where $\lambda_0 = \infty$ and $\lambda_{r+1} = -\infty$, and assume $\text{gap}(a, b) > 0$.

Then, as $\|\mathbf{D}_\phi^{(2)} - \hat{\mathbf{D}}_{\hat{\mathbf{Y}}}^{(2)}\|_F \rightarrow 0$,

$$\begin{aligned} & \min_{\mathbf{R} \in \mathbb{O}(b-a+1)} \left(\sum_{t=1}^T \|\hat{\psi}(t; a, b) - \mathbf{R}\psi(t; a, b)\|^2 \right)^{1/2} \\ &= \frac{2\kappa(a, b)}{\lambda_a^{1/2}} \|\mathbf{D}_\phi^{(2)} - \hat{\mathbf{D}}_{\hat{\mathbf{Y}}}^{(2)}\|_F + O\left(\|\mathbf{D}_\phi^{(2)} - \hat{\mathbf{D}}_{\hat{\mathbf{Y}}}^{(2)}\|_F^2\right). \end{aligned}$$

This proposition identifies the leading term of the trajectory error and makes its constant explicit. In particular, the error is smaller when (i) the leading eigenvalue λ_a is large, and (ii) the spectral gap $\text{gap}(a, b)$ and the smallest eigenvalue λ_b are not too small relative to λ_a . This ratio is captured by the conditioning number $\kappa(a, b)$, so that the leading constant scales proportionally to $\kappa(a, b)/\lambda_a^{1/2}$.

Combining the two stage propagation argument, we obtain the following theorem.

Theorem E.5. *Assume Assumptions E.1 and E.2, such that $f(n), g(n) \rightarrow 0$. Assume that \mathbf{E}_ϕ has exactly r positive eigenvalues, and that $\text{gap}(a, b) > 0$ for $1 \leq a \leq b \leq r$.*

Then there exists a possibly random orthogonal matrix $\mathbf{R} \in \mathbb{O}(b-a+1)$ such that

$$\left(\sum_{t=1}^T \|\hat{\psi}(t; a, b) - \mathbf{R}\psi(t; a, b)\|^2 \right)^{1/2} = \mathcal{O}(f(n) + g(n)) \quad a.s.$$

The result of Theorem E.5 applies in several settings. When the full trajectory of dimension r is used, $\text{gap}(1, r) > 0$ always holds, and $\kappa(1, r) = \lambda_1/\lambda_r$. When truncating to $c < r$ dimensions, $\kappa(1, c) = \lambda_1/(\lambda_c - \lambda_{c+1})$, highlighting the importance of the spectral gap. In particular, when $c = 1$, the result yields a 1D trajectory, which is essential for the change point analysis in the subsequent section.

Together, Proposition E.3, Proposition E.4, and Theorem E.5 provide the template used in the rest of the appendix. For each specific dissimilarity, it remains only to verify the two uniform controls in Assumptions E.1 and E.2. The corresponding trajectory consistency result then follows from the same CMDS perturbation argument.

F Limitations of Euclidean Mirror with Maximum Directional Variation

This section clarifies why the maximum directional variation (MV) distance used in the Euclidean Mirror construction of Athreya et al. [4] is not sufficient for the multiscale goals of this paper. The MV distance is based on the spectral norm of the second-moment matrix of latent displacement, and therefore captures only the largest direction of temporal variation between two time points. This makes it effective as a dominant change summary, but it also discards subordinate directions that may correspond to distinct and interpretable temporal events.

We first instantiate the abstract trajectory consistency framework from Appendix D for the MV distance, showing that MV based trajectories can be consistently estimated under the canonical normalization. We then show that this consistency does not remove the intrinsic limitations of the MV construction in that it compresses temporal variation into a single dominant direction, does not generally yield an exact Euclidean realization over a finite set of time points, and provides weaker attribution because the maximizing direction can vary across time pairs. These limitations motivate the trace variation and mode-wise variation distances developed in the main text.

Throughout this section, all population distances $d(\cdot, \cdot)$ and finite sample distances $\hat{d}(\cdot, \cdot)$ refer to $d_{\text{MV}}(\cdot, \cdot)$ and $\hat{d}_{\text{MV}}(\cdot, \cdot)$ defined below. Since modified UASE produce longitudinally stable embeddings, no additional Procrustes alignment across time is required [1].

F.1 Consistency and Attribution for MV Based Trajectories

We first introduce a population level notion of the second-moment matrix of the difference between random vectors. Let $\mathbf{x}, \mathbf{y} \in L^2(\Omega; \mathbb{R}^d)$ be random vectors. The population second-moment matrix of the difference between \mathbf{x} and \mathbf{y} is defined as

$$\mathbf{M}(\mathbf{x}, \mathbf{y}) := \mathbb{E}[(\mathbf{x} - \mathbf{y})(\mathbf{x} - \mathbf{y})^\top].$$

As a finite sample analogue, we define the second-moment matrix of the difference between data matrices. Let $\mathbf{X}, \mathbf{Y} \in \mathbb{R}^{n \times d}$. The finite sample second-moment matrix of the difference between \mathbf{X} and \mathbf{Y} is defined as

$$\hat{\mathbf{M}}(\mathbf{X}, \mathbf{Y}) := \frac{1}{n} (\mathbf{X} - \mathbf{Y})^\top (\mathbf{X} - \mathbf{Y}).$$

Definition F.1 (Maximum directional variation distance and its finite sample counterpart). Let $\mathbf{x}, \mathbf{y} \in L^2(\Omega; \mathbb{R}^d)$. The maximum directional variation (MV) distance between \mathbf{x} and \mathbf{y} is defined as

$$d_{\text{MV}}(\mathbf{x}, \mathbf{y}) := \|\mathbf{M}(\mathbf{x}, \mathbf{y})\|_2^{1/2} = \sup_{\|\mathbf{u}\|=1} \|(\mathbf{x} - \mathbf{y})^\top \mathbf{u}\|_{L^2(\Omega; \mathbb{R})}.$$

Let $\mathbf{X}, \mathbf{Y} \in \mathbb{R}^{n \times d}$. The finite sample maximum directional variation (MV) distance between $\mathbf{X}, \mathbf{Y} \in \mathbb{R}^{n \times d}$ is defined as

$$\hat{d}_{\text{MV}}(\mathbf{X}, \mathbf{Y}) := \left\| \hat{\mathbf{M}}(\mathbf{X}, \mathbf{Y}) \right\|_2^{1/2} = \frac{1}{n^{1/2}} \|\mathbf{X} - \mathbf{Y}\|_2.$$

This distance quantifies the maximal directional variation induced by the difference between two random vectors or data matrices.

We next verify that the two abstract assumptions required for Theorem E.5 hold for the MV distance.

Proposition F.2. *With d_{MV} and \hat{d}_{MV} , Assumption E.1 is satisfied with $f(n) = n^{-1/2} \log n$.*

Proposition F.3. *Assume that Assumption 3.2 holds, and that the dynamic embeddings $\hat{\mathbf{Y}}(t)$ are obtained via modified UASE. Then, for the distances $d_{\text{MV}}(\cdot, \cdot)$ and $\hat{d}_{\text{MV}}(\cdot, \cdot)$, the embeddings $\hat{\mathbf{Y}}(t)$ satisfy Assumption E.2 with $g(n) = n^{-1/2} \log n$.*

Let $\hat{\psi}_{\text{MV}}$ be the CMDS embedding obtained from the dissimilarity matrix with entries $\hat{d}_{\text{MV}}(\hat{\mathbf{Y}}(t), \hat{\mathbf{Y}}(s))$. Then, applying Theorem E.5 with these rates yields the following consequence.

Corollary F.4. *Assume that Assumption 3.2 holds, and that the dynamic embeddings $\hat{\mathbf{Y}}(t)$ are obtained via modified UASE. Suppose \mathbf{E}_ϕ is a positive semidefinite matrix of rank c . Then, there exists a possibly random orthogonal matrix $\mathbf{R} \in \mathbb{O}(c)$ such that*

$$\sum_{t=1}^T \|\hat{\psi}_{\text{MV}}(t) - \mathbf{R} \psi_{\text{MV}}(t)\|^2 = O\left(\frac{(\log n)^2}{n}\right) \quad a.s.$$

We now state node-level to trajectory-level control for Euclidean trajectories constructed from $\hat{d}_{\text{MV}}(\cdot, \cdot)$. To avoid ambiguity, we index each trajectory by its underlying dissimilarity. Let $\hat{\mathbf{E}}_{\text{MV}}$ denote the centered Gram matrices associated with the estimated distances. The next theorem provides a node-level to trajectory-level control for MV based trajectories, showing that trajectory distances can be sandwiched by averages of node-level squared displacements, up to a CMDS truncation residual.

Theorem F.5. *Suppose $\hat{\mathbf{E}}_{\text{MV}}$ has at least c positive eigenvalues. Then, for any $t, s \in \mathcal{T}$,*

$$\left| \|\hat{\psi}_{\text{MV}}(t) - \hat{\psi}_{\text{MV}}(s)\|^2 - \frac{1}{n} \sup_{\|\mathbf{u}\|=1} \sum_{i=1}^n \left\{ \left(\hat{\mathbf{Y}}_{i:}(t) - \hat{\mathbf{Y}}_{i:}(s) \right)^\top \mathbf{u} \right\}^2 \right| \leq 2 \left(\sum_{i=c+1}^T \lambda_i(\hat{\mathbf{E}}_{\text{MV}})^2 \right)^{1/2}.$$

In particular,

$$\begin{aligned} & \frac{1}{nd} \sum_{i=1}^n \left\| \hat{\mathbf{Y}}_{i:}(t) - \hat{\mathbf{Y}}_{i:}(s) \right\|^2 - 2 \left(\sum_{i=c+1}^T \lambda_i(\hat{\mathbf{E}}_{\text{MV}})^2 \right)^{1/2} \\ & \leq \|\hat{\psi}_{\text{MV}}(t) - \hat{\psi}_{\text{MV}}(s)\|^2 \\ & \leq \frac{1}{n} \sum_{i=1}^n \left\| \hat{\mathbf{Y}}_{i:}(t) - \hat{\mathbf{Y}}_{i:}(s) \right\|^2 + 2 \left(\sum_{i=c+1}^T \lambda_i(\hat{\mathbf{E}}_{\text{MV}})^2 \right)^{1/2}. \end{aligned}$$

F.2 Metric Properties and Non-Euclidean Realizability

We show that the quantities $d_{\text{MV}}(\mathbf{x}, \mathbf{y})$ and $\hat{d}_{\text{MV}}(\mathbf{X}, \mathbf{Y})$ define metrics on $L^2(\Omega; \mathbb{R}^d)$ (up to almost sure equivalence) and $\mathbb{R}^{n \times d}$, respectively. The argument follows that of Athreya et al. [4], but is considerably simpler since no Procrustes alignment is required in the present setting.

Proof. Non-negativity and symmetry are immediate.

Identity of indiscernibles. For any $\mathbf{x}, \mathbf{y} \in L^2(\Omega; \mathbb{R}^d)$,

$$\begin{aligned} d_{\text{MV}}(\mathbf{x}, \mathbf{y}) = 0 &\iff \forall \mathbf{u} \in \mathbb{R}^d, \|(\mathbf{x} - \mathbf{y})^\top \mathbf{u}\|_{L^2(\Omega; \mathbb{R})} = 0 \\ &\iff \forall \mathbf{u} \in \mathbb{R}^d, \mathbf{u}^\top (\mathbf{x} - \mathbf{y}) = 0 \quad \text{almost surely} \\ &\iff \mathbf{x} = \mathbf{y} \quad \text{almost surely.} \end{aligned}$$

For $\mathbf{X}, \mathbf{Y} \in \mathbb{R}^{n \times d}$, it follows immediately that

$$\hat{d}_{\text{MV}}(\mathbf{X}, \mathbf{Y}) = 0 \iff \|\mathbf{X} - \mathbf{Y}\|_2 = 0 \iff \mathbf{X} = \mathbf{Y}.$$

Triangle inequality. Let $\mathbf{x}, \mathbf{y}, \mathbf{z} \in L^2(\Omega; \mathbb{R}^d)$. For any unit vector $\mathbf{u} \in \mathbb{R}^d$ with $\|\mathbf{u}\|_2 = 1$, Minkowski's inequality in $L^2(\Omega; \mathbb{R})$ yields

$$\|(\mathbf{x} - \mathbf{z})^\top \mathbf{u}\|_{L^2(\Omega; \mathbb{R})} \leq \|(\mathbf{x} - \mathbf{y})^\top \mathbf{u}\|_{L^2(\Omega; \mathbb{R})} + \|(\mathbf{y} - \mathbf{z})^\top \mathbf{u}\|_{L^2(\Omega; \mathbb{R})}.$$

Taking the supremum over all such unit vectors \mathbf{u} , we obtain

$$d_{\text{MV}}(\mathbf{x}, \mathbf{z}) \leq d_{\text{MV}}(\mathbf{x}, \mathbf{y}) + d_{\text{MV}}(\mathbf{y}, \mathbf{z}).$$

For $\mathbf{X}, \mathbf{Y}, \mathbf{Z} \in \mathbb{R}^{n \times d}$, the triangle inequality of the spectral norm implies

$$\hat{d}_{\text{MV}}(\mathbf{X}, \mathbf{Z}) = \frac{1}{n^{1/2}} \|\mathbf{X} - \mathbf{Z}\|_2 \leq \frac{1}{n^{1/2}} \|\mathbf{X} - \mathbf{Y}\|_2 + \frac{1}{n^{1/2}} \|\mathbf{Y} - \mathbf{Z}\|_2 = \hat{d}_{\text{MV}}(\mathbf{X}, \mathbf{Y}) + \hat{d}_{\text{MV}}(\mathbf{Y}, \mathbf{Z}).$$

□

However, MV distances used in the Euclidean Mirror construction of Athreya et al. [4] on a finite set cannot, in general, be realized exactly by any trajectory in Euclidean space. Here is a concrete example.

Fix latent dimension $d = 2$ and time point set $\mathcal{T} = \{1, 2, 3, 4\}$. Let $(\Omega, \mathcal{F}, \mathbb{P})$ be given by $\Omega = \{\omega_1, \omega_2\}$, $\mathbb{P}(\{\omega_1\}) = \mathbb{P}(\{\omega_2\}) = 0.5$. Define random vectors $\chi \in L^2(\Omega; \mathbb{R}^2)$, $\phi(t) \in L^2(\Omega; \mathbb{R}^2)$, $t \in \mathcal{T}$ by specifying their realizations as follows:

$$\chi(\omega_1) = (\sqrt{2}, 0), \quad \chi(\omega_2) = (0, \sqrt{2}),$$

and for $t \in \{1, 2, 3, 4\}$,

$$\begin{aligned} \phi_1(\omega_1) &= (1/8, 0), & \phi_1(\omega_2) &= (0, 1/8), \\ \phi_2(\omega_1) &= (1/8, 0), & \phi_2(\omega_2) &= (0, 1/4), \\ \phi_3(\omega_1) &= (1/4, 0), & \phi_3(\omega_2) &= (0, 1/8), \\ \phi_4(\omega_1) &= (1/8, 0), & \phi_4(\omega_2) &= (0, 3/8). \end{aligned}$$

Then $(\chi, \{\phi(t)\}_{t \in \mathcal{T}})$ satisfies the assumptions in Definition B.1.

The population distance matrix is

$$\mathbf{D}_\phi = \frac{1}{8\sqrt{2}} \begin{pmatrix} 0 & 1 & 1 & 2 \\ 1 & 0 & 1 & 1 \\ 1 & 1 & 0 & 2 \\ 2 & 1 & 2 & 0 \end{pmatrix},$$

thus the exact eigenvalues of the centered Gram matrix are:

$$\lambda_1 = \frac{5 + 3\sqrt{3}}{512}, \quad \lambda_2 = \frac{1}{256}, \quad \lambda_3 = -\frac{3\sqrt{3} - 5}{512}, \quad \lambda_4 = 0$$

Since it has a negative eigenvalue λ_3 , it is not positive semidefinite. Therefore, this distance matrix cannot be embedded in a Euclidean space.

F.3 Interpretive Limitations of the MV Distance

The preceding results show that MV based trajectories are statistically well behaved under the canonical normalization. Nevertheless, the MV distance has intrinsic limitations for the multiscale goals of this paper.

First, MV depends only on the largest eigenvalue of the second-moment matrix of latent position differences. It therefore summarizes each pairwise temporal comparison by the magnitude of its most pronounced directional variation. This makes MV useful for detecting dominant changes, but it discards subordinate directions that may correspond to distinct structural events. Consequently, higher CMDS coordinates obtained from MV distances generally lack a stable mode-wise interpretation, since the distance itself does not identify persistent lower order directions of variation.

Second, MV provides weaker attribution. The node-level to trajectory-level control in Theorem F.5 relates MV trajectory distances to node-level displacement only through directions optimized separately for each time pair (t, s) . Because these maximizing directions can vary across time pairs, the resulting attribution is not temporally consistent. The alternative uniform comparison is also loose in higher dimensions due to the factor $1/d$. Thus MV does not support the kind of stable node-level decomposition needed for interpretable temporal analysis.

Third, although $d_{MV}(\cdot, \cdot)$ and $\hat{d}_{MV}(\cdot, \cdot)$ are valid metrics, Section F.2 shows that the induced distance matrix over a finite set of time points need not be Euclidean. Therefore, CMDS may only provide an approximate realization of MV distances, and the resulting coordinates should be interpreted as an approximation to the MV distance structure rather than as an exact temporal geometry.

These limitations motivate the trace variation and mode-wise variation distances developed in the main text, which retain the full second-moment structure, admit stable orthogonal decompositions, and provide sharper attributional interpretations.

G Consistency of Multiscale Euclidean Trajectories

This section applies the abstract error propagation framework of Appendix E to the trace variation and mode-wise variation distances used in the main text. The only points to verify are the two uniform controls in Assumptions E.1 and E.2. Once these are established, trajectory consistency follows directly from Theorem E.5.

G.1 Application to the trace variation distance

We begin by defining the trace variation distance and its finite sample counterpart.

Definition G.1 (Trace variation distance and its finite sample counterpart). Let $\mathbf{x}, \mathbf{y} \in L^2(\Omega; \mathbb{R}^d)$. The trace variation (TV) distance between \mathbf{x} and \mathbf{y} is defined as

$$d_{TV}(\mathbf{x}, \mathbf{y}) := (\text{tr} \mathbf{M}(\mathbf{x}, \mathbf{y}))^{1/2} = \|\mathbf{x} - \mathbf{y}\|_{L^2(\Omega; \mathbb{R}^d)}.$$

Let $\mathbf{X}, \mathbf{Y} \in \mathbb{R}^{n \times d}$. The finite sample trace variation (TV) distance between $\mathbf{X}, \mathbf{Y} \in \mathbb{R}^{n \times d}$ is defined as

$$\hat{d}_{TV}(\mathbf{X}, \mathbf{Y}) := \left(\text{tr} \hat{\mathbf{M}}(\mathbf{X}, \mathbf{Y}) \right)^{1/2} = \frac{1}{n^{1/2}} \|\mathbf{X} - \mathbf{Y}\|_F.$$

By construction, $d_{TV}(\cdot, \cdot)$ and $\hat{d}_{TV}(\cdot, \cdot)$ coincide with the $L^2(\Omega; \mathbb{R}^d)$ -induced distance and scaled Frobenius distances, respectively. Consequently, they define metrics on $L^2(\Omega; \mathbb{R}^d)$ (up to almost sure equivalence) and on $\mathbb{R}^{n \times d}$. Since both distances are induced by inner products, the corresponding Gram matrices are positive semidefinite. As a consequence, there exists a Euclidean Mirror of sufficiently high dimension such that these distances are exactly realized.

We first verify the two abstract assumptions for the trace variation distance.

Proposition G.2. *With the distance $d_{TV}(\cdot, \cdot)$ and $\hat{d}_{TV}(\cdot, \cdot)$, Assumption E.1 is satisfied with $f(n) = n^{-1/2} \log n$.*

This proposition shows that the finite sample trace variation distance computed from sampled latent positions concentrates uniformly around its population counterpart at the stated rate.

We next verify the embedding level stability condition under canonical normalization. The anchor isotropy assumption ensures that the modified unfolded adjacency spectral embedding is identifiable up to an orthogonal transformation, which is sufficient for preserving Euclidean distance geometry.

Proposition G.3. *Assume that Assumption 3.2 holds, and that the dynamic embeddings $\hat{\mathbf{Y}}(t)$ are obtained via modified UASE. Then, with the distance $d_{\text{TV}}(\cdot, \cdot)$ and $\hat{d}_{\text{TV}}(\cdot, \cdot)$, the embeddings satisfy Assumption E.2 with $g(n) = n^{-1/2} \log n$.*

Together, Propositions G.2 and G.3 verify the two abstract assumptions required to control the error of the Euclidean trajectory constructed from trace variation distances. Applying Theorem E.5 with these rates yields the following consequence. The following corollary is the first part of Theorem 3.7 in the main text.

Corollary G.4. *Assume that Assumption 3.2 holds, and that the dynamic embeddings $\hat{\mathbf{Y}}(t)$ are obtained via modified UASE. Suppose \mathbf{E}_ϕ is a positive semidefinite matrix of rank c . Then, there exists a possibly random orthogonal matrix $\mathbf{R} \in \mathbb{O}(c)$ such that*

$$\sum_{t=1}^T \|\hat{\psi}_{\text{TV}}(t) - \mathbf{R}\psi_{\text{TV}}(t)\|^2 = O\left(\frac{(\log n)^2}{n}\right) \quad a.s.$$

This corollary establishes strong consistency of the trace variation Euclidean trajectory: up to an orthogonal transformation, the estimated trajectory coordinates converge almost surely to their population counterparts at an explicit rate. As a result, the trace trajectory provides a stable and geometrically meaningful representation of global temporal network evolution.

G.2 Application to the mode-wise variation distances

We now verify the same abstract assumptions for the mode-wise variation distances. Compared to the trace variation case, the main additional feature is that the distance $d_k(\cdot, \cdot)$ and its finite sample counterpart $\hat{d}_k(\cdot, \cdot)$ explicitly depend on the choice of orthonormal bases $\{\mathbf{u}_k\}_{k=1}^d$ and $\{\hat{\mathbf{u}}_k\}_{k=1}^d$. The selection of an appropriate orthonormal basis, along with its finite sample counterpart is crucial, and the eigenvectors of the aggregated second-moment matrix is a natural and principled choice.

We begin by defining the mode-wise variation distance and its finite sample counterpart.

Definition G.5 (Mode-wise variation distance and its finite sample counterpart). Fix an orthonormal basis $\{\mathbf{u}_k\}_{k=1}^d$ of \mathbb{R}^d . Let $\mathbf{x}, \mathbf{y} \in L^2(\Omega; \mathbb{R}^d)$. The k th mode-wise variation distance between \mathbf{x} and \mathbf{y} is defined as

$$d_k(\mathbf{x}, \mathbf{y}) := (\mathbf{u}_k^\top \mathbf{M}(\mathbf{x}, \mathbf{y}) \mathbf{u}_k)^{1/2} = \|(\mathbf{x} - \mathbf{y})^\top \mathbf{u}_k\|_{L^2(\Omega; \mathbb{R})}.$$

Similarly, fix an orthonormal basis $\{\hat{\mathbf{u}}_k\}_{k=1}^d$. Let $\mathbf{X}, \mathbf{Y} \in \mathbb{R}^{n \times d}$. The finite sample k th mode-wise variation distance between $\mathbf{X}, \mathbf{Y} \in \mathbb{R}^{n \times d}$ is defined as

$$\hat{d}_k(\mathbf{X}, \mathbf{Y}) := \left(\hat{\mathbf{u}}_k^\top \hat{\mathbf{M}}(\mathbf{X}, \mathbf{Y}) \hat{\mathbf{u}}_k \right)^{1/2} = \frac{1}{n^{1/2}} \|(\mathbf{X} - \mathbf{Y}) \hat{\mathbf{u}}_k\|.$$

By construction, $d_k(\cdot, \cdot)$ and $\hat{d}_k(\cdot, \cdot)$ define pseudometrics on $L^2(\Omega; \mathbb{R}^d)$ and on $\mathbb{R}^{n \times d}$, respectively. Specifically,

$$\begin{aligned} d_k(\mathbf{x}, \mathbf{y}) = 0 &\Leftrightarrow (\mathbf{x} - \mathbf{y})^\top \mathbf{u}_k = 0 \text{ almost surely,} \\ \hat{d}_k(\mathbf{X}, \mathbf{Y}) = 0 &\Leftrightarrow (\mathbf{X} - \mathbf{Y}) \hat{\mathbf{u}}_k = 0. \end{aligned}$$

As with the trace variation distance, for each mode k , there exists a Euclidean Mirror of sufficiently high dimension such that these distances are exactly realized.

Definition G.6 (Aggregated directional variation basis and its finite sample counterpart). Fix a finite set of time points $\mathcal{T} = \{1, \dots, T\}$ and a collection of time pairs $\mathcal{S} \subseteq \mathcal{T} \times \mathcal{T}$. Here \mathcal{S} is user-specified (e.g., all pairs, adjacent pairs, or pairs within a temporal window) and determines the global orthogonal mode basis.

For each $t \in \mathcal{T}$, let $\mathbf{y}(t) \in L^2(\Omega; \mathbb{R}^d)$ be a random vector. Define the aggregated second-moment matrix

$$\mathcal{M} := \sum_{(t,s) \in \mathcal{S}} \mathbf{M}(\mathbf{y}(t), \mathbf{y}(s)) \in \mathbb{R}^{d \times d}.$$

Assuming that \mathcal{M} has d positive, separated eigenvalues, we set \mathbf{u}_k as the eigenvector corresponding to the k th largest eigenvalue.

Similarly, for each $t \in \mathcal{T}$, let $\mathbf{Y}(t) \in \mathbb{R}^{n \times d}$. Define the finite sample aggregated second-moment matrix

$$\hat{\mathcal{M}} := \sum_{(t,s) \in \mathcal{S}} \hat{\mathbf{M}}(\mathbf{Y}(t), \mathbf{Y}(s)) \in \mathbb{R}^{d \times d}.$$

Assuming that $\hat{\mathcal{M}}$ has d positive, separated eigenvalues, we set $\hat{\mathbf{u}}_k$ as the eigenvector corresponding to the k th largest eigenvalue. Note that $\hat{\mathbf{u}}_k$ are left singular vectors of the $d \times n|\mathcal{S}|$ matrix constructed by vertically concatenating $\frac{1}{n^{1/2}}(\mathbf{Y}(t) - \mathbf{Y}(s))$ for all $(t, s) \in \mathcal{S}$.

Henceforth, we adopt this orthonormal basis $\{\mathbf{u}_k\}_{k=1}^d$ and its finite sample counterpart $\{\hat{\mathbf{u}}_k\}_{k=1}^d$ for the mode-wise variational distances.

We first verify the population to sample stability condition for the mode-wise variation distances.

Proposition G.7. *With the distance $d_k(\cdot, \cdot)$ and $\hat{d}_k(\cdot, \cdot)$, Assumption E.1 is satisfied with $f(n) = n^{-1/2} \log n$.*

This result shows that, for each fixed mode k , the finite sample mode-wise variation distance concentrates uniformly around its population counterpart at the same rate as the trace variation distance.

We next verify the embedding level stability condition under canonical normalization.

Proposition G.8. *Assume that Assumption 3.2 holds, and that the dynamic embeddings $\hat{\mathbf{Y}}(t)$ are obtained via modified UASE. Then, with the distance $d_k(\cdot, \cdot)$ and $\hat{d}_k(\cdot, \cdot)$, the embeddings satisfy Assumption E.2 with $g(n) = n^{-1/2} \log n$.*

Together, Propositions G.7 and G.8 verify that the two abstract assumptions required by the trajectory consistency theorem continue to hold for each mode-wise distance.

As in the TV case, applying Theorem E.5 with these rates provides trajectory-level error bounds for the mode- k trajectory $\hat{\psi}_k$ for each fixed $k \in \{1, \dots, d\}$. This is the latter part of Theorem 3.7 in the main text.

Corollary G.9. *Assume that Assumption 3.2 holds, and that the dynamic embeddings $\hat{\mathbf{Y}}(t)$ are obtained via modified UASE. Suppose \mathbf{E}_ϕ is a positive semidefinite matrix of rank c . Then, there exists a possibly random orthogonal matrix $\mathbf{R} \in \mathbb{O}(c)$ such that*

$$\sum_{t=1}^T \|\hat{\psi}_k(t) - \mathbf{R}\psi_k(t)\|^2 = O\left(\frac{(\log n)^2}{n}\right) \quad a.s.$$

This corollary establishes strong consistency of each mode-wise Euclidean trajectory. Taken together with the trace variation case, these results show that the proposed framework supports stable and interpretable trajectory representations both globally and along individual orthogonal modes of temporal variation.

H Extensions: Node Attribution and Change Point Detection

This section supplements Section 3.4 by providing further details on two extensions of the multiscale Euclidean trajectory framework. The first is a node-level attribution theory showing how trace and mode-wise temporal variation decompose into contributions from individual nodes. The second is a change point framework showing how 1D Euclidean trajectories can be used to localize level and slope changes along specific structural modes.

H.1 Node-level attributions

Adding to the node-level attribution discussion in the main text, we highlight two additional observations.

First, the contribution of node i to the trace variation decomposes exactly into contributions along individual modes. Since $\{\hat{\mathbf{u}}_k\}_{k=1}^d$ forms an orthonormal basis of \mathbb{R}^d , each node-wise difference admits the exact orthogonal decomposition

$$\|\hat{\Delta}_i\|^2 = \sum_{k=1}^d \langle \hat{\Delta}_i, \hat{\mathbf{u}}_k \rangle^2.$$

This identity shows that the mode decomposition holds not only at the distance and trajectory level but also at the node-level.

Second, we highlight that attribution of mode-wise variation retain sign information. Compared to the trace variation approach, in which node attribution is represented by the squared norm, the mode-wise variation represents node attribution as a squared inner product. Unlike the norm, the inner product inherently preserves sign information. Consequently, the sign of the attribution may convey additional information beyond the magnitude of the contribution alone. This will be further verified in the additional experiments; see Appendix I.4.

H.2 Node-level to trajectory-level guarantees for multi-mode trajectories

We now establish node-level to trajectory-level relationships for Euclidean trajectories constructed from the trace variation distance $\hat{d}_{\text{TV}}(\cdot, \cdot)$ and from the mode-wise distances $\hat{d}_k(\cdot, \cdot)$. These results formalize how node-level variation aggregates into distances in the corresponding trajectory embeddings, thereby providing a precise link between local structural change and trajectory-level geometric representations of time.

The following results relate local node-level variation to distances in the corresponding Euclidean trajectories. The residual spectral terms on the right hand sides quantify the truncation error incurred when embedding the trajectories in a fixed dimension c , and vanish when the associated centered Gram matrices is a positive semidefinite matrix of rank c . The following Theorem corresponds to the first half of Theorem 3.8 in the main text.

Theorem H.1. *Suppose $\hat{\mathbf{E}}_{\text{TV}}$ has at least c positive eigenvalues. Then for any $t, s \in \mathcal{T}$,*

$$\left| \|\hat{\psi}_{\text{TV}}(t) - \hat{\psi}_{\text{TV}}(s)\|^2 - \frac{1}{n} \sum_{i=1}^n \|\hat{\mathbf{Y}}_{i:}(t) - \hat{\mathbf{Y}}_{i:}(s)\|^2 \right| \leq 2 \left(\sum_{i=c+1}^T \lambda_i(\hat{\mathbf{E}}_{\text{TV}})^2 \right)^{1/2}.$$

This result shows that distances in the trace trajectory recover the average squared magnitude of node-level position changes, up to a residual term determined by the truncated eigenvalues of the centered Gram matrix. Thus, global temporal distances in the trajectory faithfully reflect aggregate local variation when the trajectory dimension is sufficiently large. The following Theorem corresponds to the latter part of Theorem 3.8 in the main text.

Theorem H.2. *Suppose $\hat{\mathbf{E}}_k$ has at least c positive eigenvalues. Then for any $t, s \in \mathcal{T}$,*

$$\left| \|\hat{\psi}_k(t) - \hat{\psi}_k(s)\|^2 - \frac{1}{n} \sum_{i=1}^n \langle \hat{\mathbf{Y}}_{i:}(t) - \hat{\mathbf{Y}}_{i:}(s), \hat{\mathbf{u}}_k \rangle^2 \right| \leq 2 \left(\sum_{i=c+1}^T \lambda_i(\hat{\mathbf{E}}_k)^2 \right)^{1/2}.$$

Analogously, this theorem shows that distances in the k th mode-wise trajectory approximate the aggregated node-level variation along the corresponding mode. Together, Theorems H.1 and H.2 establish that multi-mode Euclidean trajectories provide geometrically faithful summaries of node-level temporal change, both globally and along individual structural dimensions, with explicit control over the error introduced by dimensional truncation.

Here, we establish a tighter bound for the aggregated error.

Theorem H.3. *Suppose $T \geq 2$ and $\hat{\mathbf{E}}_{\text{TV}}$ has at least c positive eigenvalues. Then,*

$$\sum_{t < s} \left| \|\hat{\psi}_{\text{TV}}(t) - \hat{\psi}_{\text{TV}}(s)\|^2 - \frac{1}{n} \sum_{i=1}^n \|\hat{\mathbf{Y}}_{i:}(t) - \hat{\mathbf{Y}}_{i:}(s)\|^2 \right|^2 \leq 4(T-1) \left(\sum_{i=c+1}^T \lambda_i(\hat{\mathbf{E}}_{\text{TV}})^2 \right).$$

Theorem H.4. *Suppose $T \geq 2$ and $\hat{\mathbf{E}}_k$ has at least c positive eigenvalues. Then,*

$$\sum_{t < s} \left| \|\hat{\psi}_k(t) - \hat{\psi}_k(s)\|^2 - \frac{1}{n} \sum_{i=1}^n \left\langle \hat{\mathbf{Y}}_{i:}(t) - \hat{\mathbf{Y}}_{i:}(s), \hat{\mathbf{u}}_k \right\rangle^2 \right|^2 \leq 4(T-1) \left(\sum_{i=c+1}^T \lambda_i(\hat{\mathbf{E}}_k)^2 \right).$$

H.3 Change point order and 1D trajectory geometry

We adopt the notion of change point order introduced by Chen et al. [5], which is defined through finite differences of a latent position process. This notion provides a principled way to distinguish different types of temporal change according to the level at which nonstationarity occurs.

Let $\{X(t)\}_{t \in \mathbb{Z}}$ be a latent position process taking values in a Hilbert space, and let $\delta > 0$ be a fixed lag. The first order difference is defined as

$$\Delta_\delta X(t) = X(t) - X(t - \delta),$$

with higher order differences defined recursively.

In Chen et al. [5], a change point at time τ is said to be of order k if the distribution of the k th order finite difference $\Delta_\delta^{(k)} X(t)$ changes at τ . A 0th order change point corresponds to a distributional change in the latent positions $X(t)$ themselves, while a 1st order change point corresponds to a change in the distribution of the latent increments $X(t) - X(t - \delta)$.

In Chen et al. [5], these change point definitions are linked to geometry through the Euclidean trajectory construction. Although the increments $X(t) - X(t - \delta)$ are not directly embedded, Chen et al. [5] show that under a random walk latent position model the increment structure determines the time pair squared dissimilarity matrix

$$d^2(t, s) = \mathbb{E}[\|X(t) - X(s)\|^2].$$

When latent increments are distributionally stationary within regimes but change across regimes, this squared distance grows quadratically in $|t - s|$ within each regime, with regime dependent coefficients. Applying CMDS to this dissimilarity matrix yields a Euclidean embedding of time whose leading coordinate is piecewise linear, with slope changes at 1st order change points. By contrast, 0th order change points manifest as jumps in the trajectory embedding.

In the present work, we construct multiple Euclidean trajectories from a single dynamic network time series, each corresponding to a resolved mode of temporal variation. Let $\psi_k(t)$ denote the one-dimensional Euclidean trajectory obtained with the k th mode-wise variation distance. The notion of change point order is unchanged from Chen et al. [5]; the key difference is that the mode-wise resolution allows multiple change points, potentially of different orders, to be identified simultaneously along distinct directions of temporal variation.

Definition H.5 (0th and 1st order of change points).

- (1) A time τ is a *0th order change point in mode k* if $\psi_k(t)$ is piecewise constant in t with a jump at τ .
- (2) A time τ is a *1st order change point in mode k* if $\psi_k(t)$ is piecewise linear in t with a change in slope at τ .

This definition provides a direct geometric realization of change point order. A jump in $\psi_k(t)$ corresponds to an abrupt change in the latent structure along mode k , while a change in slope corresponds to a change in the rate of latent evolution along that mode. The contribution of the present framework is not to redefine change point order, but to express it mode-wise manner through one-dimensional Euclidean trajectories rather than the full latent process, thereby allowing change points of different orders to occur simultaneously along distinct orthogonal modes of temporal variation.

H.4 Change Point Estimation and Localization

In this subsection, we formalize the definition of a change point and introduce the corresponding estimator based on 1D Euclidean trajectories. Throughout, let $\psi(t)$ denote a 1D population trajectory and let $\hat{\psi}(t)$ denote its estimated counterpart obtained from observed data.

Definition H.6. Let $\mathcal{K} \subseteq \{2, \dots, T\}$ be the set of candidate knot locations, and let $k \in \mathcal{K}$. Let θ denote a parameter set. Let $\Psi_L(\cdot; k, \theta)$ and $\Psi_R(\cdot; k, \theta)$ be parametric functions before and after k , respectively. We define a piecewise function

$$\Psi(t; k, \theta) = \begin{cases} \Psi_L(t; k, \theta), & t < k, \\ \Psi_R(t; k, \theta), & t \geq k. \end{cases}$$

Example (0th order case). Let $\mathcal{K}^{(0)} = \{2, \dots, T\}$ and $\theta = (a_L, a_R)$ with $a_L \neq a_R$. Define

$$\Psi_L^{(0)}(t; k, \theta) = a_L, \quad \Psi_R^{(0)}(t; k, \theta) = a_R.$$

This specification models a 0th order change point through a discontinuous jump in the trajectory coordinate at time k .

Example 2 (1st order case). Let $\mathcal{K}^{(1)} = \{2, \dots, T-1\}$ and $\theta = (a, b_L, b_R)$ with $b_L \neq b_R$. Define

$$\Psi_L^{(1)}(t; k, \theta) = a + b_L t, \quad \Psi_R^{(1)}(t; k, \theta) = a + b_L k + b_R(t - k).$$

This formulation enforces continuity of $\Psi^{(1)}(\cdot; k, \theta)$ at the knot $t = k$ while allowing a change in slope, corresponding to a 1st order change point.

A time point $t^* \in \mathcal{K}$ is a change point if $\psi(t)$ is well approximated by $\Psi(t; t^*, \theta^*)$ for some parameter set θ^* .

For each candidate $k \in \mathcal{K}$, fit the best piecewise function with a knot at k by minimizing

$$\hat{Q}(k) := \min_{\theta} \sum_{t=1}^T \left(\hat{\psi}(t) - \Psi(t; k, \theta) \right)^2.$$

over θ . We then define

$$\hat{t} \in \arg \min_{k \in \mathcal{K}} \hat{Q}(k).$$

Before turning to estimation error, we emphasize the separation of roles between trajectory estimation and change point modeling. The results below treat the estimated trajectory $\hat{\psi}(t)$ as noisy observations of an underlying population trajectory $\psi(t)$. All stochastic error enters exclusively through the discrepancy between $\hat{\psi}$ and ψ , which is controlled by the Euclidean trajectory consistency results established earlier. Conditional on this trajectory-level error, change point estimation is analyzed as a deterministic approximation problem for piecewise parametric functions. This separation allows change point guarantees to be derived independently of the specific embedding or dissimilarity construction, provided uniform control of the trajectory estimation error is available.

We now analyze how estimation error in the trajectory coordinates propagates to error in the estimated change point. The goal of this subsection is to formalize conditions under which the population change point is identifiable and to quantify how deviations between estimated and population trajectory representations translate into localization error for the estimated change point.

We begin by formalizing identifiability of the population change point and the associated best fitting model. The following assumption ensures that the population objective admits a unique minimizer in both the change point location and the model parameters, ruling out ambiguity in the target of inference.

Assumption H.7. Suppose

$$Q(k) := \min_{\theta} \sum_{t=1}^T (\psi(t) - \Psi(t; k, \theta))^2.$$

is uniquely minimized at $t^* \in \mathcal{K}$ and

$$\min_{\theta} \sum_{t=1}^T (\psi(t) - \Psi(t; t^*, \theta))^2$$

has a unique minimizer θ^* .

This assumption ensures that, at the population level, there is a single change point and a single best fitting model describing the temporal structure on either side of the change.

The next assumption quantifies how rapidly the population objective deteriorates as the candidate change point moves away from the true location. This condition imposes a linear separation bound, ensuring that the population objective provides sufficient curvature to distinguish nearby change point locations.

Assumption H.8. Let $D(\theta^*)$ be a nonnegative function. There exist a constant $\alpha > 0$ such that for all $k \in \mathcal{K}$,

$$\min_{\theta} \sum_{t=1}^T (\Psi(t; t^*, \theta^*) - \Psi(t; k, \theta))^2 \geq \alpha D(\theta^*) |k - t^*|.$$

Assumption H.8 provides a linear separation condition for the population objective around the true change point. Together with uniqueness, it allows deviations of the estimation objective to be translated into localization error for the estimated change point.

These assumptions leads to Theorem 3.9 in the main text. It shows that change point error is controlled by the trajectory estimation error together with the approximation error of the chosen piecewise model.

Remark. The bound separates two sources of error. The first term reflects estimation error in the trajectory coordinates, capturing the discrepancy between estimated and population trajectories. The second term captures approximation error of the change point model itself, reflecting how well the chosen parametric form $\Psi(\cdot; k, \theta)$ approximates the true population trajectory. In later sections, trajectory consistency results are used to control the first term explicitly, thereby yielding concrete localization rates for the estimated change point.

We now verify that the separation condition in Assumption H.8 holds for the 0th and 1st order change point models introduced above. These results ensure that the abstract localization theorem applies to the concrete parametric models used for change point inference in one-dimensional Euclidean trajectories.

Proposition H.9. Let $\Psi = \Psi^{(0)}$ and assume Assumption H.7. Suppose that $\theta^* = (a_L^*, a_R^*)$ with $a_L^* \neq a_R^*$. Then, Assumption H.8 holds with

$$D(\theta^*) := |a_L^* - a_R^*|^2.$$

This proposition shows that, for a 0th order change point model, identifiability is driven by the magnitude of the level shift across the change point: larger jumps yield stronger separation and hence more precise localization.

Proposition H.10. Let $\Psi = \Psi^{(1)}$ and assume Assumption H.7. Suppose that $\theta^* = (a^*, b_L^*, b_R^*)$ with $b_L^* \neq b_R^*$. Then, Assumption H.8 holds with

$$D(\theta^*) := |b_L^* - b_R^*|^2.$$

Analogously, for a 1st order change point model, separation is governed by the difference in slopes across the change point. This ensures that deviations from the true change point incur a linearly increasing penalty in the population objective.

We now combine these separation results with the trajectory consistency bounds developed earlier. Specifically, when the dynamic embeddings $\tilde{\mathbf{Y}}(t)$ are obtained via the modified UASE construction, we can quantify the localization error of a 0th or 1st order change point detected from the one-dimensional Euclidean trajectory associated with a fixed mode-wise variation distance.

With Theorems 3.9 and E.5, Propositions G.7, G.8 in hand, we obtain the following corollary.

Corollary H.11. *Assume Assumption 3.2 holds and $\hat{Y}(t)$ is obtained via the modified UASE. Assume that $\lambda_1(\mathbf{E}_\phi), \lambda_1(\mathbf{E}_\phi) - \lambda_2(\mathbf{E}_\phi) > 0$. Assume H.7, and the change point is of 0th or 1st order.*

Then, for every $A > 0$, there exist constants $C_A > 0$ and integers N_A such that, for all $n \geq N_A$,

$$|\hat{t} - t^*| \leq \frac{4}{\alpha D(\theta^*)} \left\{ C_A \frac{\log n}{n^{1/2}} + Q(t^*)^{1/2} \right\}^2.$$

with probability at least $1 - n^{-A}$.

Note that the sign ambiguity of the estimated Euclidean trajectory does not affect 0th or 1st order change point localization: both $\hat{\psi}$ and $-\hat{\psi}$ yield the same estimated \hat{t} .

This result completes the link between trajectory consistency and change point estimation. The bound shows that the error in the estimated change point location is controlled by the trajectory estimation error through the ℓ_2 deviation $\sum_t (\hat{\psi}(t) - \psi(t))^2$, together with the intrinsic separation $D(\theta^*)$ of the underlying change point model. In particular, under anchor isotropy and the modified UASE construction, the change point estimator is consistent whenever the corresponding mode-wise Euclidean trajectory is consistent. The dependence on the spectral gaps of \mathbf{E}_ϕ reflects the stability of the temporal geometry in the selected mode and is unavoidable in mode-wise change point analysis.

I Additional Experimental Details

This section provides the full experimental details omitted from the main text due to space constraints. It describes the complete synthetic data generation procedure, the construction of the real world legal citation network, implementation details for all methods and baselines, and additional quantitative and qualitative results. These supplementary experiments are organized around the papers main claims, including canonical geometry, multiscale trajectory recovery, exact node attribution, change point detection, and interpretability on real world data.

I.1 Synthetic Datasets

The two synthetic datasets were generated according to the process described in Appendix B. They can be viewed as dynamic stochastic block models (SBM) [12] with three equally sized communities. We set the number of latent modes to 3 and let $\{e_k\}_{k=1}^3$ denote the standard basis of \mathbb{R}^3 . The anchor random vector is sampled as

$$\chi = \sqrt{3} e_k \quad \text{with probability } \frac{1}{3}, \quad k \in \{1, 2, 3\},$$

and, conditional on χ , the dynamic random vector at time t is defined by

$$\phi(t) = \frac{1}{3} \mathbf{B}(t) \chi,$$

where $\mathbf{B}(t) \in \mathbb{R}^{3 \times 3}$ is a time-varying block probability matrix. This yields a dynamic SBM with uniform community proportions. The network structure is decomposed into the orthonormal modes

$$\mathbf{u}_1 = \frac{1}{\sqrt{3}}(1, 1, 1), \quad \mathbf{u}_2 = \frac{1}{\sqrt{6}}(1, 1, -2), \quad \mathbf{u}_3 = \frac{1}{\sqrt{2}}(1, -1, 0),$$

where \mathbf{u}_1 captures global connectivity, \mathbf{u}_2 captures separation between community 3 and communities 1 and 2, and \mathbf{u}_3 captures separation between communities 1 and 2. Let $\xi_k(t)$ denote the strength of mode k at time t . The block probability matrix is defined as

$$\mathbf{B}(t) = \sum_{k=1}^3 \xi_k(t) \mathbf{u}_k \mathbf{u}_k^\top.$$

Under this parametrization, the 1D mode-wise trajectory coincides with $\xi_k(t)$ up to a parallel shift specific to each k , together with a possible sign ambiguity. Each $\xi_k(t)$ is chosen to exhibit either a 0th order or 1st order change point, with the change points occurring at different times across modes. Since the population trajectories are known, this benchmark allows direct evaluation of geometric distortion, mode recovery, node attribution, and change point localization against the ground truth.

We construct two synthetic datasets with distinct ground truth trajectories using the basis defined above, each tailored to a specific experimental objective. Dataset 1 is used exclusively to empirically validate our theoretical results under controlled conditions that exactly match their assumptions. In particular, each mode contains a single change point, which is a standard simplifying assumption in change point localization. By contrast, Dataset 2 is designed for comparison with existing state-of-the-art change point detection methods and features more complex temporal dynamics in order to assess robustness beyond these assumptions.

Dataset 1 (Single change point per mode): We show the mode strength $\xi_k(t)$ in the left panel of Figure I.1, with $T = 16$ time points. For this dataset, the ordering of the modes by their contribution to temporal variation is exactly the same as the basis ordering. In other words, mode k corresponds to \mathbf{u}_k for $k = 1, 2, 3$. Each mode contains a single change point, summarized as follows.

- Mode 1 (\mathbf{u}_1): a 1st order change point at $t_1^* = 4$,
- Mode 2 (\mathbf{u}_2): a 0th order change point at $t_2^* = 9$,
- Mode 3 (\mathbf{u}_3): a 0th order change point at $t_3^* = 13$.

To validate the convergence of our proposed estimators, we generate networks with the following numbers of nodes:

$$n \in \{30, 50, 70, 100, 150, 200, 300, 400, 500\},$$

and produce 100 independent realizations for each n .

Dataset 2 (Multiple change points per mode): The underlying mode strength is shown in the right panel of Figure I.1, with $T = 70$ time points. We can confirm that each mode-wise trajectory contains multiple change points. We fix the number of nodes at $n = 500$ and generate 100 independent realizations. Unlike Dataset 1, the correspondence between the mode indices and the basis vectors is not aligned, and each mode exhibits multiple change points of varying order. Specifically, the modes are defined as follows:

- Mode 1 (\mathbf{u}_3): 0th order change points at $t_{1,1}^* = 31$ and $t_{1,2}^* = 61$,
- Mode 2 (\mathbf{u}_2): a 0th order change point at $t_{2,1}^* = 21$ and a 1st order change point at $t_{2,2}^* = 51$,
- Mode 3 (\mathbf{u}_1): a 1st order change point at $t_{3,1}^* = 11$ and a 0th order change point at $t_{3,2}^* = 41$.

To provide an intuitive, plain language view of how the network evolves over time for both datasets, we visualize each network snapshot using Gephi [25] in Figure I.2. At every time point, communities are detected via modularity maximization [26, 27] and nodes are colored according to the resulting partition. Node positions are computed independently at each snapshot using the ForceAtlas2 layout [28], yielding visually interpretable representations of local and global connectivity structure. Because both community detection and layout are recomputed separately for each time point, node colors and positions are not intended to be directly comparable across time. The visualizations serve solely as qualitative references for the evolving network structure that is later summarized by the proposed variation and mirror based metrics.

I.2 Additional Results for Canonical Second-moment Geometry

First, using Dataset 1, we examine whether (i) the $GL(d)$ ambiguity affects the preservation of latent geometry, and (ii) the choice of basis affects the consistent recovery of mode-wise distances and trajectories, and in particular whether a canonical basis enables successful recovery. Our primary goal is trajectory recovery. However, as discussed in Section D.2, we begin by evaluating distance preservation, since accurate trajectory estimation relies on the faithful recovery of pairwise distances and therefore provides a natural way to verify that each step of the procedure successfully estimates the latent structure.

To assess geometric preservation, we compare three distance matrices:

- the estimated distance matrix $\hat{\mathbf{D}}_{\hat{\mathbf{Y}}}$,
- the finite sample distance matrix $\hat{\mathbf{D}}_{\mathbf{Y}}$, which serves as an intermediate ground truth, and

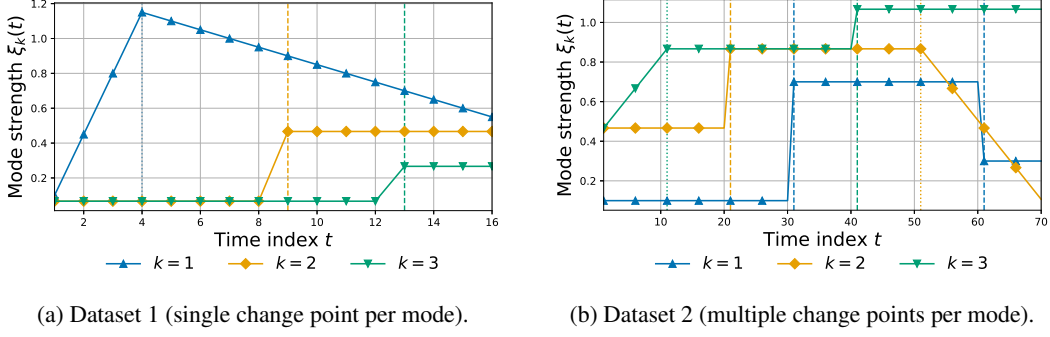
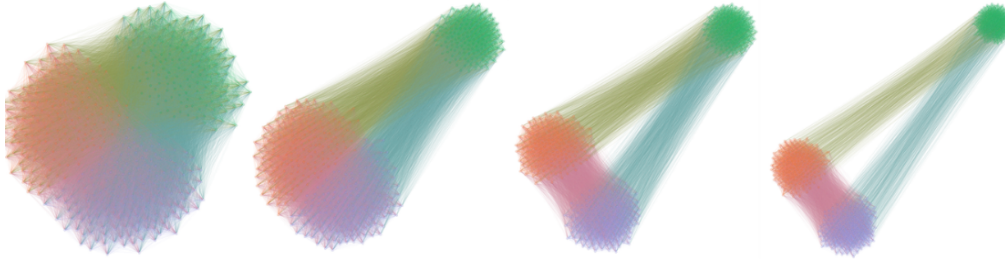
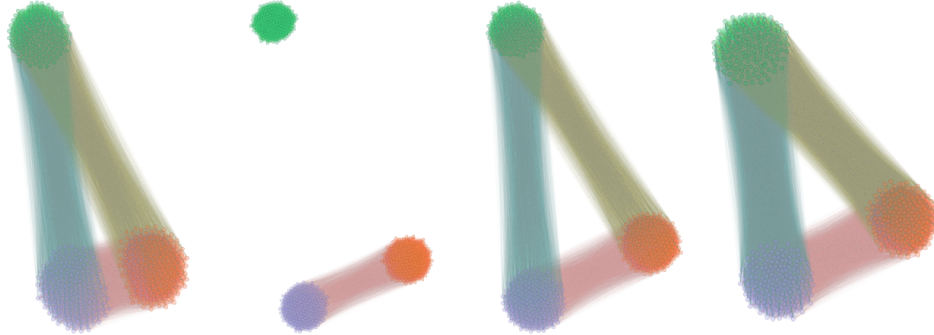


Figure I.1: Mode strengths $\xi_k(t)$ for the two datasets. Vertical segments indicate change points for the corresponding mode; dashed lines mark a jump in ξ_k (order 0) and dotted lines mark a change in slope (order 1).



(a) Dataset 1 ($t = 6, 10, 14, 16$). The modularity scores are 0.178, 0.312, 0.45 and 0.497 respectively.



(b) Dataset 2 ($t = 15, 35, 55, 70$). The modularity scores are 0.458, 0.624, 0.567 and 0.446 respectively.

Figure I.2: Visualization of network evolution (both with $n = 500$). Nodes are colored by communities detected via modularity maximization, and layouts are computed independently at each time point using ForceAtlas2.

- the population distance matrix \mathbf{D}_ϕ , which represents the target geometry.

We compare two methods: (i) the original UASE [1] and (ii) our proposed modified UASE. We consider three types of distances: the MV distance (Definition F.1), the TV distance, and the mode-wise distance. For the mode-wise analysis, we distinguish between representations under (i) a canonical basis and (ii) a fixed standard basis. Since basis selection requires multiple modes, this distinction is relevant only for mode-wise distances.

For the modified UASE, we measure geometric error using the Frobenius norm between squared distance matrices:

$$\left\| \hat{\mathbf{D}}_{\hat{\mathbf{Y}}}^{(2)} - \hat{\mathbf{D}}_{\hat{\mathbf{Y}}}^{(2)} \right\|_F, \quad \left\| \hat{\mathbf{D}}_{\hat{\mathbf{Y}}}^{(2)} - \mathbf{D}_\phi^{(2)} \right\|_F,$$

where $\hat{\mathbf{D}}_{\mathbf{Y}}^{(2)}$ denote the elementwise square of $\hat{\mathbf{D}}_{\mathbf{Y}}$.

For the original UASE, we account for the $GL(d)$ ambiguity by allowing an optimal global scaling:

$$\min_{r>0} \left\| \hat{\mathbf{D}}_{\mathbf{Y}}^{(2)} - r \hat{\mathbf{D}}_{\mathbf{Y}}^{(2)} \right\|_F, \quad \min_{r>0} \left\| \hat{\mathbf{D}}_{\mathbf{Y}}^{(2)} - r \mathbf{D}_{\phi}^{(2)} \right\|_F.$$

We then evaluate trajectory reconstruction up to sign, and up to scaling as well for the original UASE. For the modified UASE, the error is defined as

$$\min_{s \in \{\pm 1\}} \sum_{t=1}^T (\hat{\psi}(t) - s \psi(t))^2,$$

where the sign ambiguity is removed by optimizing over $s \in \{\pm 1\}$.

For each method, we evaluate both distance reconstruction accuracy and trajectory reconstruction accuracy. We report the mean \pm standard deviation over 100 independent trials for all experiments using Dataset 1.

Figure I.3 shows the results for finite sample geometric recovery. The original UASE exhibits persistent distortion across all distance types, as indicated by the dashed lines, which do not converge to 0. In contrast, the proposed method substantially reduces this mismatch and achieves stable convergence to 0 for the MV, TV, and mode-wise distances when the latter are expressed in the canonical basis, as shown in Figure I.3 (a) to (c). Figure I.3 (d), however, shows that the standard basis also fails to converge. This highlights that $GL(d)$ transformations can distort geometric structure and underscores the importance of Theorem 3.3.

We next examine whether the estimated embedding also recovers the population geometry accurately. Figure I.4 compares the estimated distance matrix $\hat{\mathbf{D}}_{\mathbf{Y}}$ with the population distance matrix \mathbf{D}_{ϕ} , providing a direct assessment of population level recovery. We observe the same qualitative pattern. Both the original UASE and the mode-wise representation obtained using the standard basis fail to converge to 0.

Having established the importance of geometric recovery, we finally report trajectory reconstruction results in Figure I.5. The solid lines in Figure I.5 (a) to (c) show that the proposed method achieves consistent convergence for the MV, TV, and all mode-wise trajectories. By contrast, the original UASE and the mode-wise trajectories based on the standard basis again fail to converge, as shown by the dashed lines in Figure I.5 (a) to (d).

To visually compare how these distortions appear in each trajectory, Figure I.6 compares the MV, TV, and mode-wise trajectories under the canonical basis, with the original UASE shown in the top row, that is, Figure I.6 (a) to (c), and the proposed method shown in the bottom row, that is, Figure I.6 (d) to (f). The dashed lines represent the population trajectories, whereas the solid lines show the estimated trajectories. Under the proposed method, the mode-wise trajectories clearly recover the distinct temporal structures embedded in the latent process. In particular, the 0th and 1st order variations are separated into different modes, enabling a more fine grained view of the temporal dynamics.

At the same time, Figure I.6 (a), (b), (d), and (e) show that the MV and TV trajectories aggregate these changes into a single global summary, thereby compressing multiple sources of variation. As a result, weaker but meaningful temporal changes that are visible in the mode-wise representation are attenuated in the global trajectories.

For the original UASE, although the overall temporal patterns are roughly preserved, noticeable distortions remain, as shown in Figure I.6 (a) to (c). In particular, the mode-wise trajectories exhibit inconsistencies in alignment and ordering across modes, suggesting that the relative importance of the latent components is not reliably recovered. This behavior is consistent with the geometric distortions induced by the $GL(d)$ ambiguity.

These results lead to three main findings: (i) the $GL(d)$ ambiguity induces geometric distortion in both the global structure, as measured by the MV and TV distances, and the mode-wise structure, (ii) the proposed method resolves this issue at the global level, enabling consistent recovery of MV and TV geometry and trajectories, and (iii) the proposed method successfully recovers mode-wise geometry and trajectories under a canonical basis, showing that consistent mode-wise recovery becomes achievable with an appropriate choice of basis.

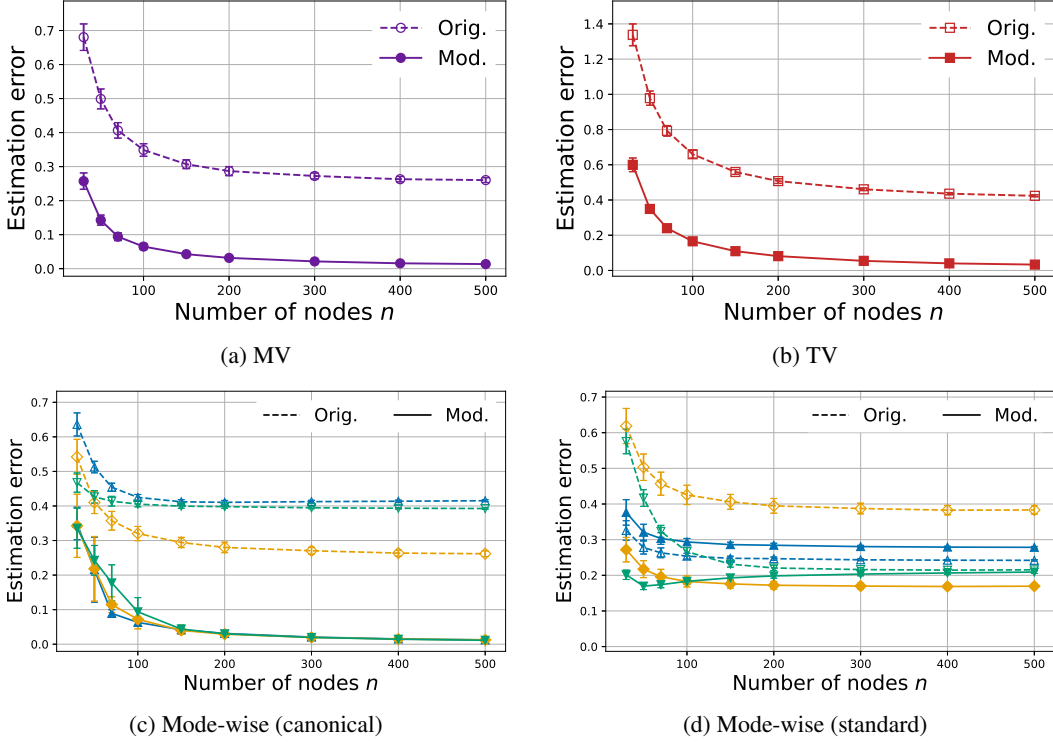


Figure I.3: Convergence of the estimation error between the finite sample distance matrix $\hat{\mathbf{D}}_{\mathbf{Y}}$ and the estimated distance matrix $\hat{\mathbf{D}}_{\mathcal{Y}}$, comparing the original UASE and the proposed modified UASE. This evaluates geometric distortion induced by the embedding across MV, TV, and mode-wise distances under canonical and standard bases.

I.3 Mode Decomposition of Trace Variation

Theorem 3.5 establishes an exact decomposition at the distance level. Since the trajectories are constructed to approximate these distances, we expect a corresponding decomposition to also appear at the trajectory-level. We verify this using Dataset 1.

We measure temporal change at each time point by taking the difference between consecutive trajectory values and then taking its squared norm. We visualize these quantities in two ways: (i) line plots for the trace trajectory with trajectory dimensions $c = 1$ and $c = 3$, and (ii) a stacked plot for the mode-wise trajectories, where the contributions of the individual modes are aggregated. The case $c = 3$ corresponds to the intrinsic dimensionality required to reconstruct the population distance in Dataset 1.

Figure I.7 shows the results. The temporal variation captured by the trace trajectory, shown in the line plots, closely aligns with the aggregated variation of the mode-wise trajectories, shown in the bar chart. In particular, we observe that

$$\|\psi_{\text{TV}}(t+1) - \psi_{\text{TV}}(t)\|_2^2 \approx \sum_{k=1}^3 \|\psi_k(t+1) - \psi_k(t)\|_2^2,$$

indicating that the variation of the trace trajectory is well explained by the sum of the mode-wise variations. This provides empirical evidence that the trajectory construction preserves not only distances, but also their decomposition structure.

When only the 1D representation is used, as shown by the solid line, the magnitude of variation decreases, although the overall temporal pattern remains broadly consistent with the sum of the mode-wise variations. By contrast, the 3-dimensional representation exhibits much closer quantitative agreement with the sum of the mode-wise variations. This confirms that the proposed construction

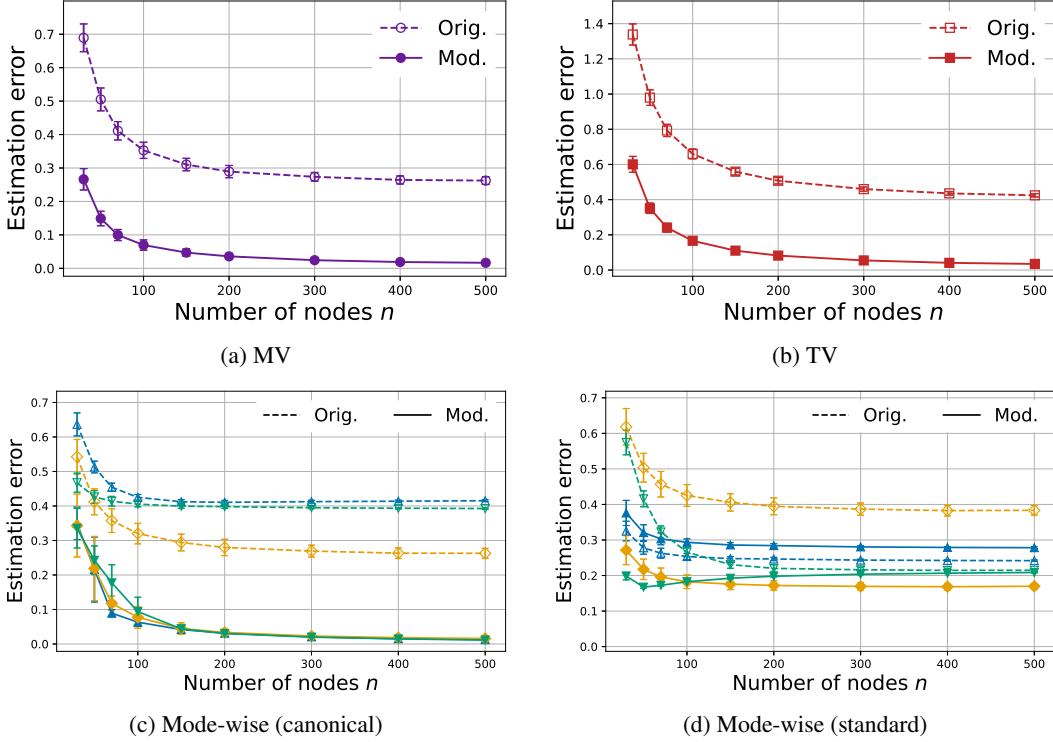


Figure I.4: Convergence of the estimation error between the population distance matrix \mathbf{D}_ϕ and the estimated distance matrix $\hat{\mathbf{D}}_{\hat{\mathbf{Y}}}$, comparing the original UASE and the proposed modified UASE. This evaluates recovery of intrinsic geometry across MV, TV, and mode-wise distances under canonical and standard bases.

preserves a coherent decomposition of temporal variation at the trajectory-level, consistent with the exact decomposition at the distance level.

I.4 Additional Results for Node Attribution

In this subsection, we verify the node attribution results summarized in Theorem 3.8 in the main text. Theorem 3.8 states that the discrepancy between trajectory differences and aggregated node-level attributions is uniformly bounded over all time pairs (t, s) by a term determined by the CMDS residual. To verify this numerically, we aggregate attribution magnitudes at the node-level by averaging across nodes:

$$\frac{1}{n} \sum_{i=1}^n \|\hat{\mathbf{Y}}_{i:}(t) - \hat{\mathbf{Y}}_{i:}(s)\|^2, \quad \frac{1}{n} \sum_{i=1}^n \left| \left\langle \hat{\mathbf{Y}}_{i:}(t) - \hat{\mathbf{Y}}_{i:}(s), \hat{\mathbf{u}}_k \right\rangle \right|^2.$$

Figure I.8 presents scatter plots over all time pairs (t, s) with $t < s$. The trajectory-level variation and the corresponding aggregated node-level attribution exhibit strong agreement, indicating that variations measured in trajectory space are well explained by local node-level contributions.

We next examine a stronger aggregate version of this result. Theorems H.3 and H.4 in the Appendix establish a tighter upper bound for the aggregated discrepancies across all time pairs (t, s) with $t < s$. Figure I.9 shows the aggregated discrepancy between trajectory-level variation and node-level attribution as a function of the trajectory dimension c . This allows us to assess whether the upper bounds derived in Theorems H.3 and H.4 are loose. The dashed line shows the theoretical upper bound, while the solid line shows the empirical error. As the trajectory dimension c increases, the alignment between trajectory differences and aggregated node-level attributions improves, consistent with the theoretical prediction.

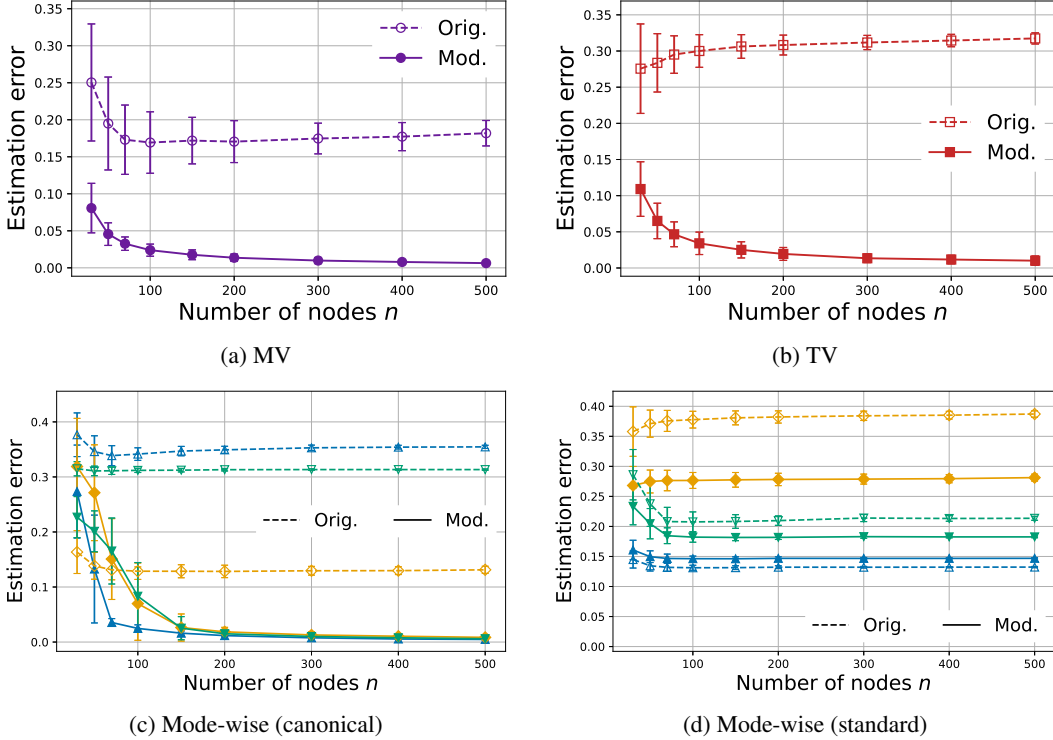


Figure I.5: Convergence of trajectory estimation error between the population and estimated trajectories, comparing the original UASE and the proposed modified UASE across MV, TV, and mode-wise cases under canonical and standard bases.

Having verified these identities numerically, we next examine whether the recovered node-level attributions also reflect the expected structural patterns. We use the estimated embeddings to visualize node-level contributions to the TV and mode-wise trajectories, as shown in Figure I.10. Each node is positioned using a t-SNE projection of the 3-dimensional modified UASE embedding. At each time point t , the size of a node marker is proportional to the magnitude of its attribution:

$$\|\hat{\mathbf{Y}}_{i:}(t) - \hat{\mathbf{Y}}_{i:}(t-1)\|^2 \quad (\text{TV}), \quad \left| \left\langle \hat{\mathbf{Y}}_{i:}(t) - \hat{\mathbf{Y}}_{i:}(t-1), \hat{\mathbf{u}}_k \right\rangle \right|^2 \quad (\text{mode-wise}).$$

For the mode-wise visualizations, color encodes the sign of the inner product, with red indicating positive values and blue indicating negative values, whereas for TV all nodes are shown in gray.

The recovered patterns closely match the synthetic ground truth. For mode 1, all nodes contribute with signs corresponding to increases or decreases in global connectivity strength. For mode 2, nodes in communities 1 and 2 exhibit signs opposite to those in community 3. For mode 3, communities 1 and 2 contribute with opposite signs, reflecting their pairwise separation. By contrast, the TV attribution aggregates these effects. Nodes with large contributions in one or more modes appear prominent, indicating that the trace trajectory reflects the combined magnitude of the mode-wise variations.

Taken together, these results demonstrate that node-level attributions provide a faithful decomposition of trajectory variation. Moreover, they capture meaningful structural patterns at the node-level while aggregating consistently to explain the variations observed in trajectory space, in agreement with the theoretical guarantees.

I.5 Localization Theorem

We next empirically verify the localization guarantee in Theorem 3.9. Dataset 1 is designed so that each population mode-wise trajectory contains a single change point, either of order 0 or order 1. Thus, for each mode, the population target is a well defined 1D change point. We estimate

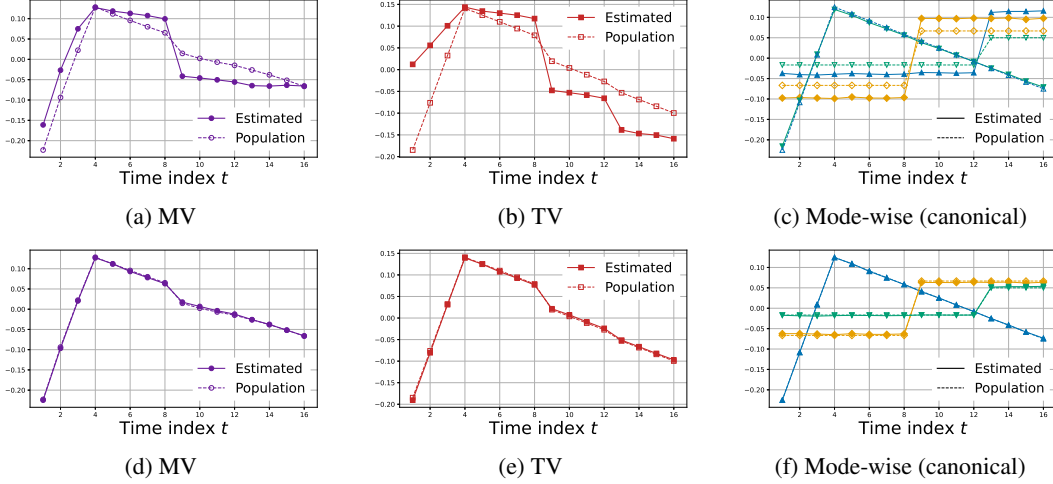


Figure I.6: Multiscale trajectories estimated by the original UASE (top row) and the proposed modified UASE (bottom row). Columns correspond to MV, TV, and mode-wise distances under a canonical basis. The mode-wise trajectories separate distinct temporal components at the mode level, while MV and TV trajectories provide global summaries. In contrast, the original UASE exhibits distortions in mode-wise trajectories, including inconsistencies in alignment and ordering across modes. Solid lines denote estimated trajectories, while dashed lines denote the corresponding population trajectories. Note that trajectories are invariant up to sign, and the signs have been adjusted for better visual interpretability.

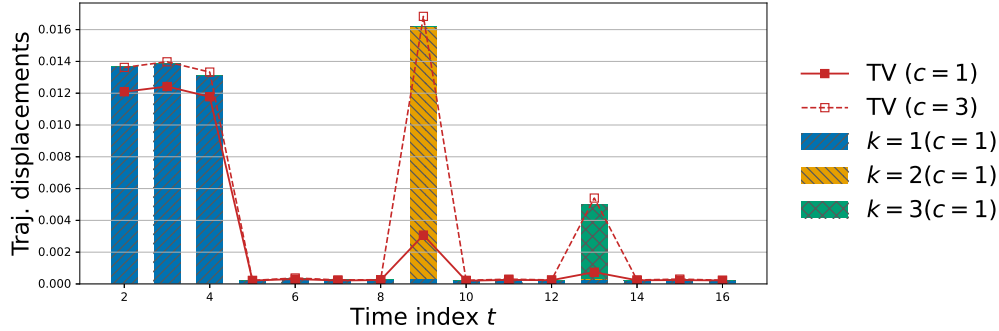


Figure I.7: Decomposition of temporal variation under the proposed modified UASE. Line plots show the squared temporal differences of the trace trajectory for dimensions $c = 1$ and $c = 3$. The stacked plot shows the sum of squared temporal differences of the mode-wise trajectories. The 3-dimensional case ($c = 3$) closely matches the aggregated mode-wise variation, while the 1D ($c = 1$) case underestimates the magnitude but broadly preserves the overall temporal pattern.

the corresponding change point time by minimizing the trajectory fitting criterion introduced in Section 3.4, and compare the proposed modified UASE with the original UASE.

Figure I.11 summarizes the results. The top row shows detection accuracy, while the bottom row shows localization error. The dashed lines indicate that the original UASE fails to detect the ground truth change points for Mode 1 and Mode 3, as shown in Figure I.11 (a), (c), (d), and (f). Although it appears to achieve higher accuracy and lower localization error for Mode 2, strong performance in only a subset of modes is insufficient when the goal is to accurately localize the full set of mode specific change points. By contrast, the solid lines show that the proposed modified UASE recovers the change points for all modes.

These results demonstrate that accurate change point detection critically depends on faithful recovery of mode-wise geometry across all modes. The original UASE suffers from geometric distortion due to the unresolved $GL(d)$ ambiguity, which leads to inconsistent performance across modes. By resolving this ambiguity, the proposed method achieves stable convergence and enables reliable

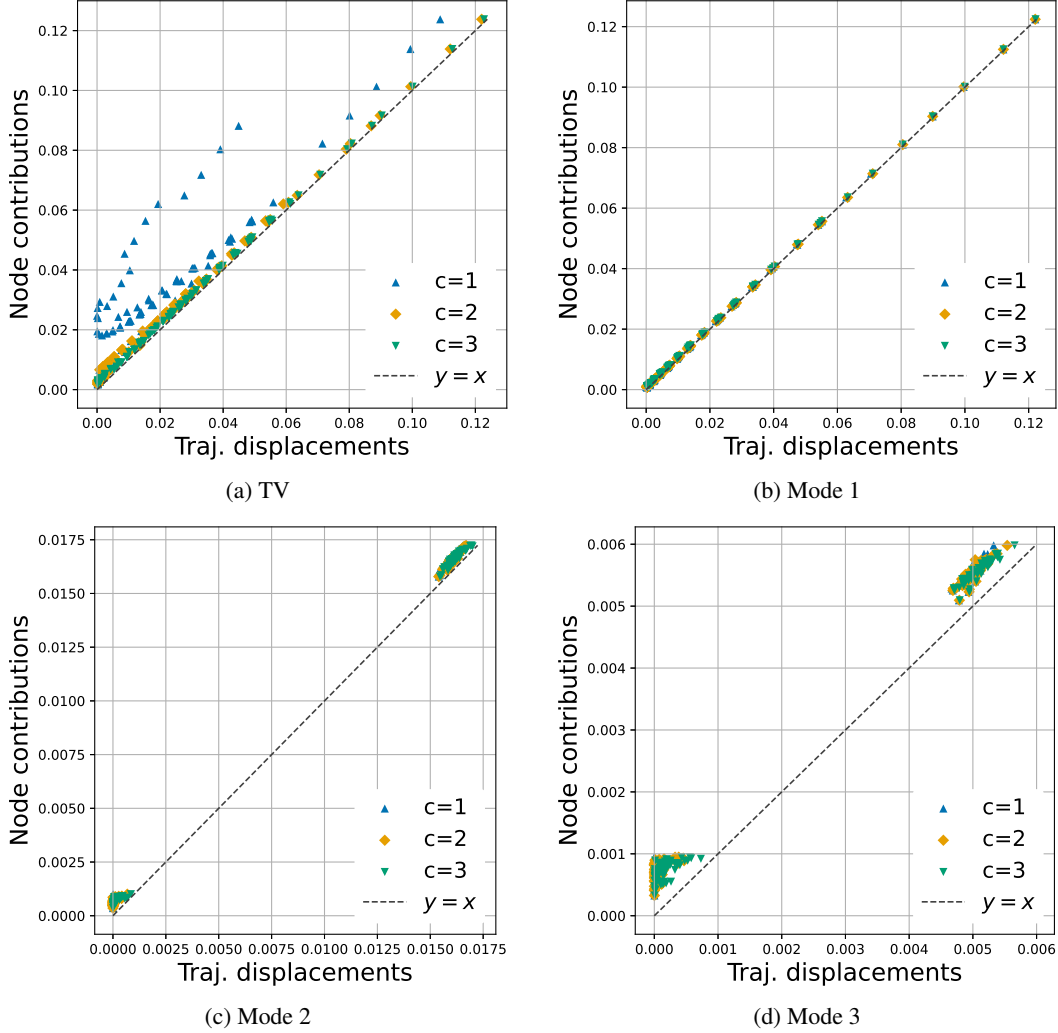


Figure I.8: Pairwise comparison between trajectory differences and aggregated node-level attributions over all time pairs (t, s) with $t < s$. Each panel corresponds to a different trajectory type (TV or mode-wise), where the mode-wise results are computed under the canonical basis. The horizontal axis shows the trajectory-level variation, and the vertical axis shows the corresponding aggregated node-level attribution. Results are shown for trajectory dimensions $c = 1, 2, 3$.

localization of mode specific temporal discontinuities, with detection accuracy converging to 1 and localization error converging to 0 across all modes.

I.6 Additional Results for the Effect of Overestimating the Embedding Dimension

In the main text, we assume that the embedding dimension d_{emb} is equal to the true latent dimension d_{lat} . In practice, however, the latent dimension is typically unknown and must be estimated or selected, potentially resulting in a misspecified embedding dimension. In particular, overestimating the embedding dimension can introduce noisy components that do not capture the underlying latent structure. In this section, we study the effect of choosing $d_{\text{emb}} > d_{\text{lat}}$.

We briefly note that when $d_{\text{emb}} < d_{\text{lat}}$, the embedding induces a spectral truncation of the latent position matrix. If the contribution from singular values beyond the top d_{emb} components is small, then the resulting trajectories remain well estimated. Moreover, the d_{emb} mode-wise trajectories correspond to the population trajectories associated with the leading modes. We do not pursue this case further, as underestimation may discard relevant signal components, whereas overestimation

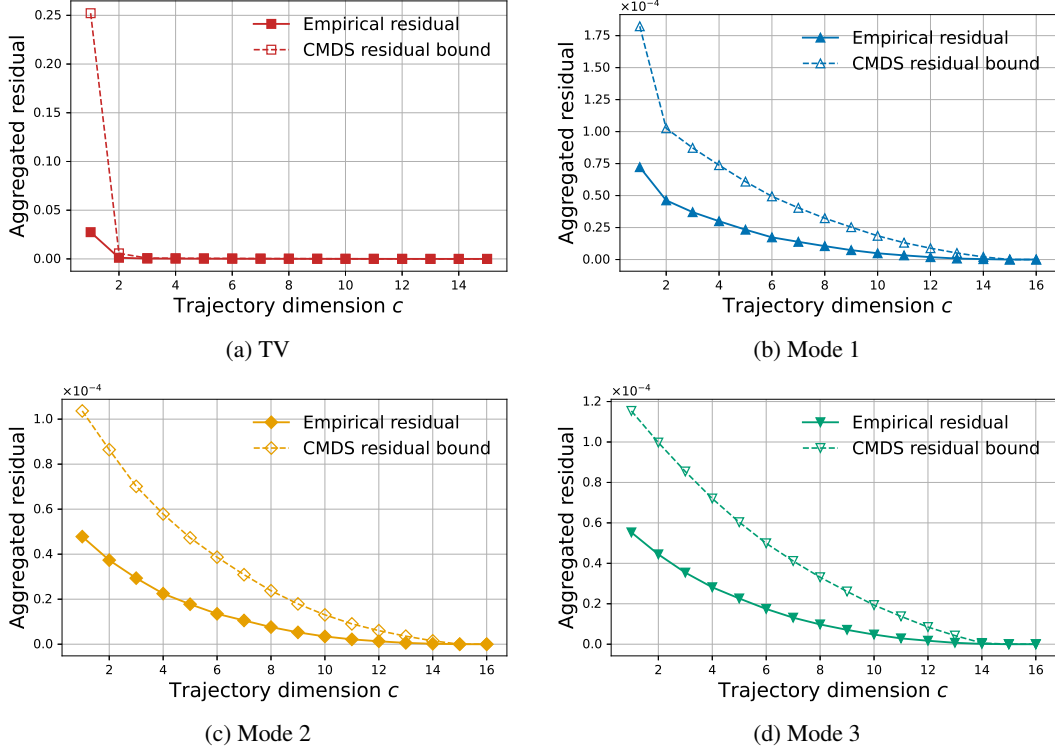


Figure I.9: Aggregated discrepancy between trajectory-level variation and node-level attribution as a function of the trajectory dimension c . The empirical residual (solid line) is compared with the theoretical upper bound (dashed line) from Theorems H.3 and H.4. Each panel corresponds to a different trajectory type (TV or mode-wise), where the mode-wise results are computed under the canonical basis.

only introduces additional error, which we show below to be asymptotically negligible for trajectory estimation.

A misspecified embedding dimension can affect both the estimated pairwise distances and the resulting trajectories, since noise introduced by the additional dimensions propagates through the estimation procedure. In particular, overestimating the embedding dimension gives rise to additional mode-wise trajectories that do not correspond to any population trajectories.

At a high level, overestimating the embedding dimension has only a limited effect, because the embedding admits a signal to noise decomposition under the modified UASE. The leading d_{lat} coordinates capture the latent structure, whereas the remaining dimensions are dominated by noise. Consequently, the estimated distances and trajectories constructed from the embeddings are effectively governed by the signal component, with the contribution of the additional dimensions vanishing asymptotically.

To formalize this intuition, we analyze the structure of the embedding and its effect on the second-moment of the displacements. We partition $\hat{\mathbf{Y}}(t) = (\hat{\mathbf{Y}}_1(t), \hat{\mathbf{Y}}_2(t))$ into its first d_{lat} coordinates and its remaining coordinates. Building on the analysis of Jones and Rubin-Delanchy [3], the modified UASE admits a signal to noise decomposition: there exists a possibly random orthogonal matrix $\mathbf{W} \in \mathbb{O}(d_{\text{lat}})$ such that

$$\sup_{t \in \mathcal{T}} \|\hat{\mathbf{Y}}_1(t) - \mathbf{Y}(t)\mathbf{W}\|_2 = \mathcal{O}(\log n) \quad \text{a.s.},$$

and

$$\sup_{t \in \mathcal{T}} \|\hat{\mathbf{Y}}_2(t)\|_2 = \mathcal{O}((\log n)^{1/2}) \quad \text{a.s.}$$

Although these bounds diverge in absolute terms, they are negligible compared to the $\mathcal{O}(n^{1/2})$ scale of the latent positions, implying that the leading d_{lat} dimensions consistently recover the latent

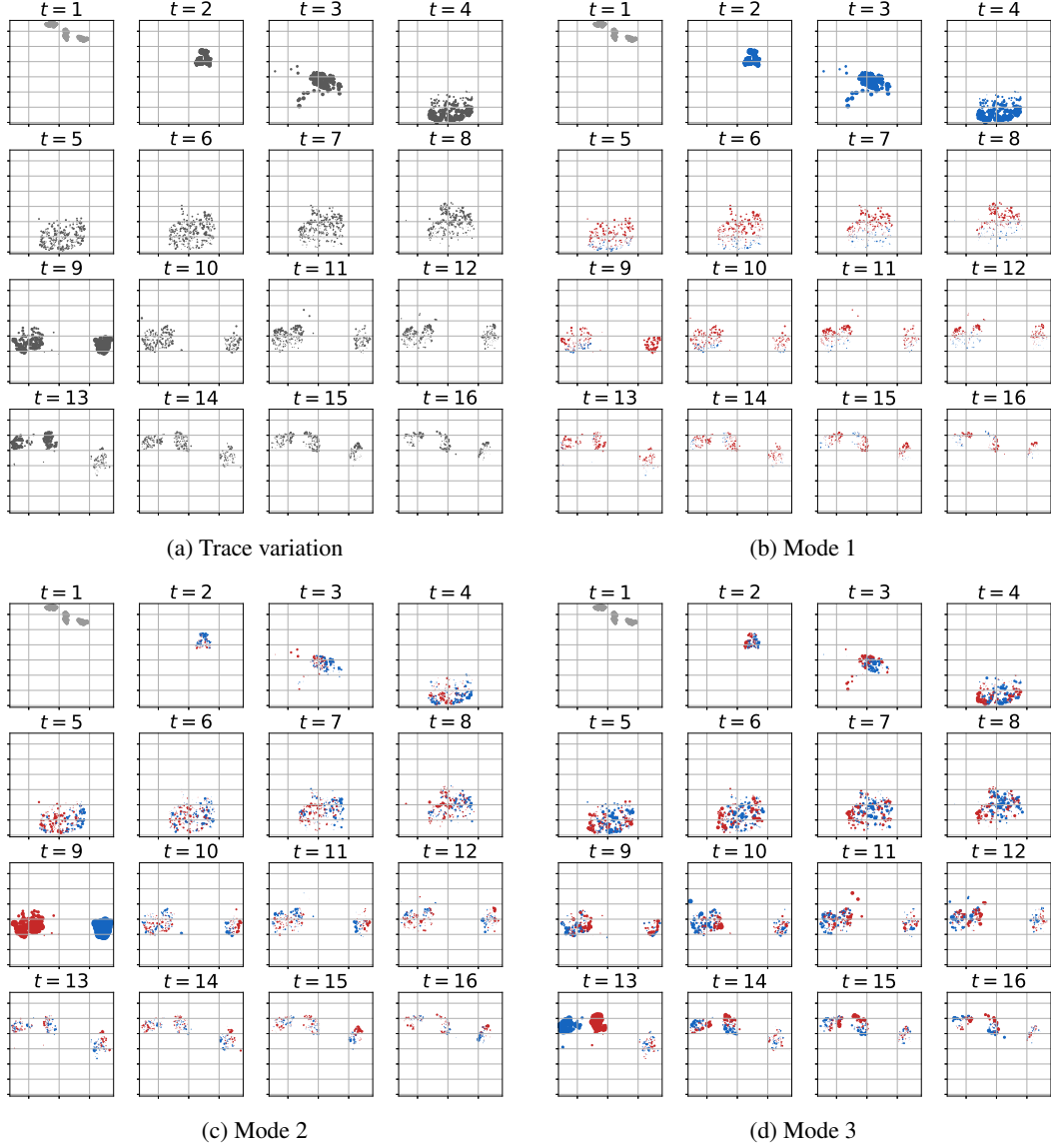


Figure I.10: Node-level attribution visualizations. Node size is proportional to the corresponding magnitude. For canonical modes, color encodes sign (red: positive, blue: negative). At $t = 1$, node sizes are uniform and colors are gray since no value is defined.

position matrix up to orthogonal transformation, while the remaining dimensions are asymptotically dominated by noise.

We now examine the second-moment of displacements, which is used in the main text to capture changes in the latent structure. Let $\Delta_1 := \hat{\mathbf{Y}}_1(t) - \hat{\mathbf{Y}}_1(s)$ and $\Delta_2 := \hat{\mathbf{Y}}_2(t) - \hat{\mathbf{Y}}_2(s)$. Then, the second-moment of displacements can be expressed as

$$\frac{1}{n}(\hat{\mathbf{Y}}(t) - \hat{\mathbf{Y}}(s))^\top (\hat{\mathbf{Y}}(t) - \hat{\mathbf{Y}}(s)) = \frac{1}{n} \begin{pmatrix} \Delta_1^\top \Delta_1 & \Delta_1^\top \Delta_2 \\ \Delta_2^\top \Delta_1 & \Delta_2^\top \Delta_2 \end{pmatrix}.$$

Using the bounds above, we obtain

$$\frac{1}{n} \Delta_1^\top \Delta_1 = \mathcal{O}(1) \quad \text{a.s.}, \quad \frac{1}{n} \Delta_1^\top \Delta_2 = \mathcal{O}(n^{-1/2}(\log n)^{1/2}) \quad \text{a.s.}, \quad \frac{1}{n} \Delta_2^\top \Delta_2 = \mathcal{O}(n^{-1} \log n) \quad \text{a.s.}$$

Thus, only the top left block remains asymptotically non negligible, and it converges to the population second-moment matrix of dimension d_{lat} , preserving the latent structure.

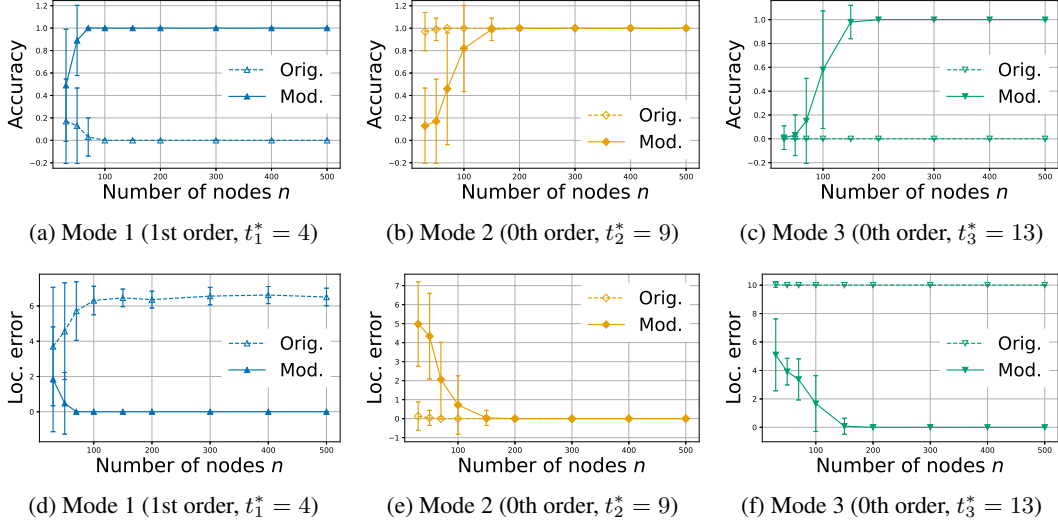


Figure I.11: Change point detection performance for each mode and evaluation metric. The top row shows detection accuracy, and the bottom row shows localization error $|\hat{t}_k - t_k^*|$. Each column corresponds to a mode-specific ground-truth change point.

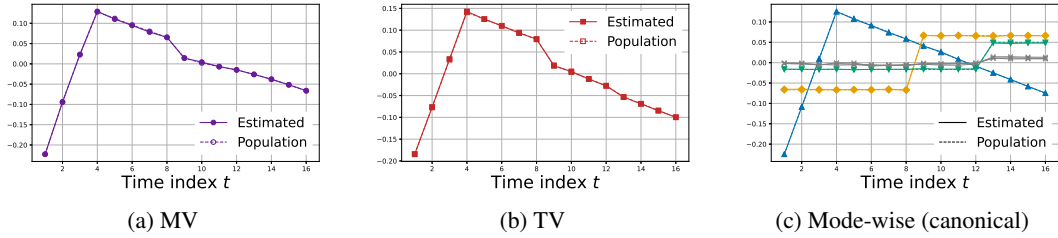


Figure I.12: Multiscale trajectories estimated by the modified UASE with embedding dimension $d_{\text{emb}} = 6$ and latent dimension $d_{\text{lat}} = 3$. The columns correspond to MV, TV, and mode-wise trajectories under a canonical basis. The leading three mode-wise trajectories capture the latent structure, while the remaining three are nearly flat, reflecting their noise-dominated nature. Note that trajectories are invariant up to sign, and the signs have been adjusted for better visual interpretability.

This implies that the effective dimensionality of the second-moment matrix is asymptotically d_{lat} . Consequently, the mode-wise trajectories corresponding to the latent structure can still be consistently estimated. In contrast, the additional trajectories induced by the excess dimensions have vanishing magnitude and therefore appear nearly flat, reflecting their noise dominated nature.

To illustrate this behavior, we conduct an experiment based on Dataset 1. The resulting trajectories are shown in Figure I.12. The network has the same latent structure as Dataset 1 and contains $n = 800$ nodes. We set the embedding dimension to $d_{\text{emb}} = 6$, while the true latent dimension is $d_{\text{lat}} = 3$.

The TV and MV trajectories, as well as the leading three mode-wise trajectories, are consistent with the population trajectories. In contrast, the remaining three mode-wise trajectories are nearly flat, reflecting their noise dominated nature. These results confirm that overestimating the embedding dimension introduces additional trajectories that do not carry meaningful signal, while leaving the estimation of the true latent structure largely unaffected.

I.7 Comparison of Multiple Change Point Detection Performance

We compare our proposed method with several competing approaches on Dataset 2. Relative to Dataset 1, this setting is substantially more challenging because it contains multiple temporal events with heterogeneous types and signal strengths. In particular, each of the three mode strengths shown in the right panel of Figure I.1 contains two change points, yielding six ground truth events overall

at

$$t \in \{11, 21, 31, 41, 51, 61\}.$$

This design tests not only whether a method can detect the presence of change, but also whether it can localize several distinct events accurately over an extended time horizon.

We compare against five baselines, namely DeltaCon [8], Laplacian Anomaly Detection (LAD) [10], the HCDL framework of Fukushima and Yamanishi [16], Euclidean Mirror [4], and the recent two stage localization and inference procedure of Wang et al. [15]. Taken together, these methods cover a range of approaches to dynamic graph change detection, including graph similarity based statistics, spectral anomaly measures, hierarchical latent diagnostics, geometric trajectory summaries, and dedicated localization procedures.

For each method, we convert the output into a ranked list of candidate change times and evaluate top K detection performance for $K \in \{3, 6, 9\}$. For methods that produce a single score sequence, we retain only strict local peaks. A time point is kept only when its score is larger than those of its two immediate neighbors, so boundary points and flat plateaus are excluded. The remaining candidates are ranked by score, and the top K are selected, with earlier times used to break ties. We also impose a minimum separation of two time units between selected candidates to avoid counting nearby peaks as distinct detections. Predicted and true change times are then matched using a tolerance window of two time units, so any prediction within ± 2 of a true change is counted as a match. From these matches, we compute the F1 score and the absolute timing error. All results are averaged over 100 trials.

For methods that produce multiple score sequences, we first fuse stream specific candidates into a single ranked list. For HCDL, and for each value of K , we take the top K candidates from each of the three level-specific streams. To make scores comparable across streams, we rescale each nominated score by dividing it by the median score of its own stream. We then pool the nominated times across streams, merge duplicate time points, and assign each merged candidate the largest fused score among its duplicates. The fused candidates are ranked globally, after which the final top K are selected subject to the same minimum separation of four time units. This yields a single set of estimated change points that is evaluated using exactly the same protocol as for the other methods.

For the proposed method, we construct change point scores from the mode-wise temporal trajectories and then fuse candidates across modes and change point orders. For each embedding mode k , let $\hat{\psi}_k(t)$ denote the associated 1D trajectory. We consider two types of changes in this trajectory: a 0th order change, corresponding to an shift in level, and a 1st order change, corresponding to a change in slope. Both scores are obtained from a local linear trend state space model fitted separately to each mode-wise trajectory. After centering $\hat{\psi}_k(t)$ and scaling it to unit variance, we fit

$$\begin{aligned} \hat{\psi}_k(t) &= L_{k,t} + \epsilon_{k,t}, & \epsilon_{k,t} &\sim \mathcal{N}(0, \sigma_{\epsilon,k}^2), \\ L_{k,t} &= L_{k,t-1} + B_{k,t-1} + \eta_{k,t}, & \eta_{k,t} &\sim \mathcal{N}(0, \sigma_{\eta,k}^2), \\ B_{k,t} &= B_{k,t-1} + \zeta_{k,t}, & \zeta_{k,t} &\sim \mathcal{N}(0, \sigma_{\zeta,k}^2), \end{aligned}$$

where $L_{k,t}$ is the local level and $B_{k,t}$ is the local slope of the k th trajectory. The disturbances $\eta_{k,t}$ and $\zeta_{k,t}$ represent innovations in the level and slope, respectively, between times $t - 1$ and t . We estimate the model parameters and initial state by maximum likelihood using the unobserved components implementation of Seabold and Perktold [23], and then apply Kalman smoothing to obtain the posterior mean disturbances

$$\hat{\eta}_{k,t} = \mathbb{E}[\eta_{k,t} \mid \hat{\psi}_k(1), \dots, \hat{\psi}_k(T)], \quad \hat{\zeta}_{k,t} = \mathbb{E}[\zeta_{k,t} \mid \hat{\psi}_k(1), \dots, \hat{\psi}_k(T)].$$

Let σ_k denote the standard deviation used before normalizing $\hat{\psi}_k(t)$. We define the 0th order and 1st order change point scores for mode k as

$$s_{k,t}^{(0)} = |\sigma_k \hat{\eta}_{k,t}|, \quad s_{k,t}^{(1)} = |\sigma_k \hat{\zeta}_{k,t}|.$$

Thus, $s_{k,t}^{(0)}$ measures the magnitude of a level innovation in the k th trajectory at time t , whereas $s_{k,t}^{(1)}$ measures the magnitude of a slope innovation. We interpret these as the level (i.e., 0th order) and slope (i.e., 1st order) change point scores for mode k .

Table I.3: Performance comparison across different values of K . Values in brackets denote 95% confidence intervals.

Method	$K = 3$		$K = 6$		$K = 9$	
	F1	MAE	F1	MAE	F1	MAE
DeltaCon	0.447 [0.444, 0.451]	2.090 [2.027, 2.147]	0.513 [0.492, 0.535]	2.400 [2.293, 2.512]	0.579 [0.565, 0.592]	2.289 [2.227, 2.352]
LAD	0.667 [0.667, 0.667]	0.733 [0.707, 0.760]	0.833 [0.833, 0.833]	1.257 [1.213, 1.300]	0.688 [0.679, 0.699]	1.888 [1.834, 1.942]
HCDL	0.322 [0.293, 0.351]	2.420 [2.280, 2.560]	0.480 [0.455, 0.505]	2.208 [2.112, 2.303]	0.532 [0.511, 0.553]	2.149 [2.092, 2.209]
Mirror	0.664 [0.660, 0.667]	0.007 [0.000, 0.020]	0.573 [0.557, 0.590]	1.562 [1.490, 1.635]	0.512 [0.500, 0.525]	2.076 [2.017, 2.136]
Two-stage	0.667 [0.667, 0.667]	0.000 [0.000, 0.000]	0.815 [0.798, 0.830]	1.037 [1.007, 1.070]	0.692 [0.677, 0.707]	2.073 [2.027, 2.120]
MENT	0.667 [0.667, 0.667]	0.000 [0.000, 0.000]	0.965 [0.952, 0.978]	0.095 [0.058, 0.135]	0.800 [0.800, 0.800]	1.002 [0.960, 1.046]

We then fuse candidates across the trajectory based score sequences. Each sequence contributes candidates given by strict local peaks. For a given K , we take the top K candidates from each sequence and pool them. Because the raw score scales may differ between the 0th order and 1st order families, we compute one shared median score within the 0th order family and one shared median score within the 1st order family, and rescale each sequence by the corresponding family median. The remaining fusion and evaluation steps are the same as those used for HCDL.

For each competing method, we tuned the hyperparameters that affect change point detection, excluding parameters fixed uniformly across all methods, such as the minimum separation rule and the timing tolerance. We performed a grid search over these method specific hyperparameters and report the best-performing configuration. For HCDL [16], we varied the half window parameter over $h \in \{2, 3, 4, 5, 6, 7, 8\}$, while fixing the maximum number of clusters to $K = 10$, which is sufficiently large for the three block synthetic networks. The mean F_1 across $K \in \{3, 6, 9\}$ peaked at $h = 6$ and decreased on both sides, so we use $h = 5$ in the experiments. For LAD [10], we swept the (short, long) window pair $(w_{\text{short}}, w_{\text{long}}) \in (3, 7), (4, 8), (5, 9)$ (burn-in = w_{long}) and fixed the number of singular values to $r = n - 1 = 499$; we cap $w_{\text{long}} < 10$ to avoid straddling the 10 timestamp inter change point spacing. The best mean F_1 was attained at $(5, 9)$. For DeltaCon [8], we used the exact implementation, since the faster approximation is intended for substantially larger networks and may introduce unnecessary approximation error at the present scale. For the two stage method of Wang et al. [15], we report results for $K \in \{3, 6, 9\}$. For the proposed method, we fixed the embedding dimension to $d = 3$. This matches the true latent dimension in the synthetic experiments, and Appendix I.6 shows that moderate overestimation of the embedding dimension does not substantially affect recovery of the relevant latent structure.

Table I.3 reports the mean results with 95% bootstrap confidence intervals. The proposed method achieves the strongest overall performance across all three values of K . At $K = 3$, it matches LAD in F1 score while achieving perfect localization accuracy among the matched detections. At $K = 6$, which coincides with the true number of change points, it attains near perfect recovery with an F1 score of 0.965 and a timing MAE of 0.1, substantially outperforming all competing methods (See also Figure I.13). Even at $K = 9$, where some degree of over selection is unavoidable, it remains the best performing approach under both metrics.

Among the baselines, LAD is one of the most competitive. This is likely because it leverages information from multiple singular values, which is broadly consistent with the multi component nature of our setting. However, because LAD summarizes these components through an aggregated spectral anomaly score rather than a canonical mode-wise temporal geometry, it is less effective at separating distinct latent directions of change. Consequently, it can miss change points that are weak in the aggregate score but clear along a specific mode. This behavior is evident in Figure I.14, where LAD fails to identify the change point at time 50.

Another strong competitor is the two stage method of Wang et al. [15], which was developed for change point localization and inference in dynamic multilayer random dot product graphs. The method first uses seeded binary segmentation with CUSUM statistics to obtain preliminary candidate change points, and then refines these candidates using low rank tensor estimation. This second stage is important. Under the dynamic multilayer RDPG model, the expected CUSUM tensor has a low rank structure induced by shared node latent positions and time-varying layer specific connectivity matrices. As a result, the refinement step can denoise the local change signal by pooling information across nodes, layers, and low rank tensor factors. This explains why the method is a

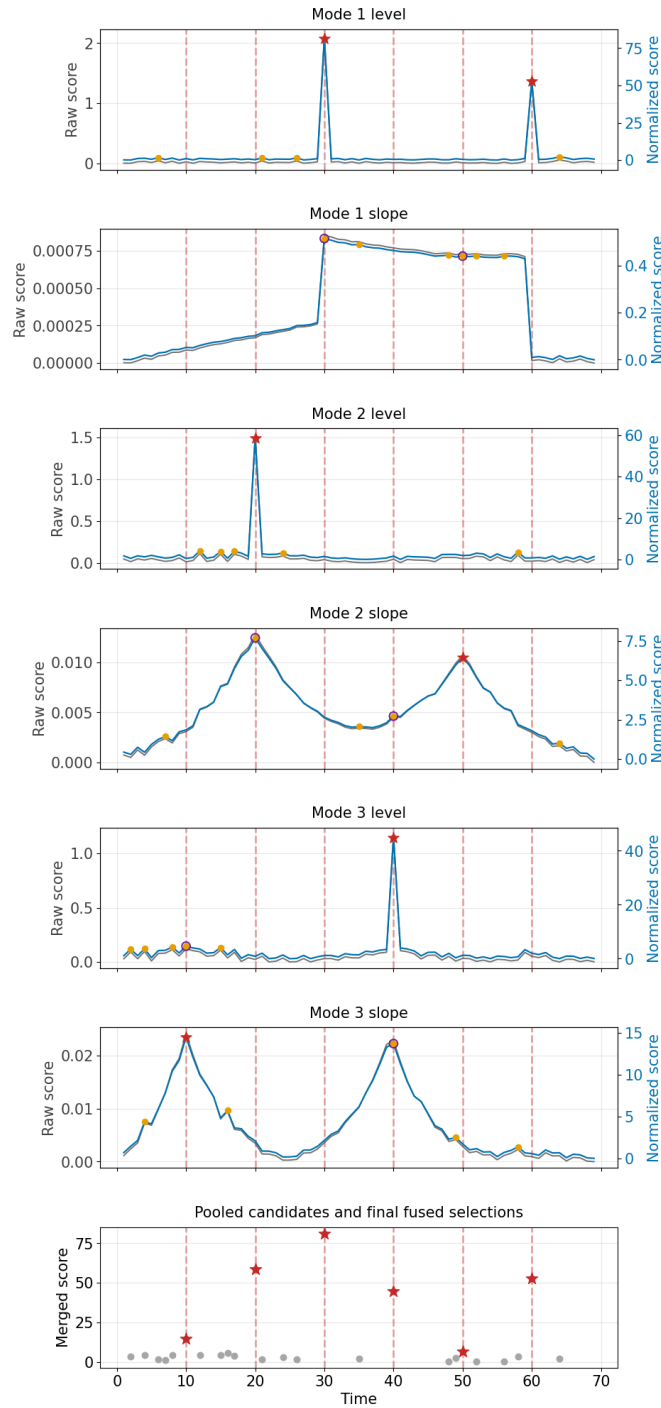


Figure I.13: Change points detected by MENT for Dataset 2. In each of the top panels, the gray curve shows the raw score for one stream. When the fusion mode uses normalized stream scores, the blue curve shows the normalized score used for fusion. Orange circles denote that streams top-K candidate changepoints. Red stars mark candidate times that are selected in the final fused top-K and for which the current stream provides the winning score. Purple hollow circles mark candidate times that are selected globally but whose winning score comes from a different stream. Vertical red dashed lines indicate the final fused changepoints. The bottom panel shows the pooled candidate set obtained by taking the union of the per-stream top-K candidates and merging them by the fusion rule; red stars indicate the final selected changepoints.

strong baseline in our experiments, even though our synthetic setting is organized around mode-wise temporal variation rather than multilayer tensor shifts.

In our experiments, the two stage method recovers most of the major events, but it can miss or mislocalize weaker mode specific changes. This is consistent with the difference between the two objectives. The two stage method is designed to localize coherent low-rank shifts in the probability tensor, whereas our method explicitly decomposes temporal variation into canonical mode-wise trajectories. Thus, when multiple changes occur along different latent directions with heterogeneous signal strengths, the proposed multiscale trajectory representation can separate events that may be partially merged or attenuated in a shared low-rank tensor localization procedure.

Because the two stage method is not naturally a score based peak picking method, we do not display a per time score curve for it. Instead, we evaluate it according to its native output that is the refined candidate change points produced by its two stage procedure. For this reason, when reporting top- K performance, we use the ranked candidate locations returned by the method directly, rather than forcing it into the same local-peak selection protocol used for single score baselines.

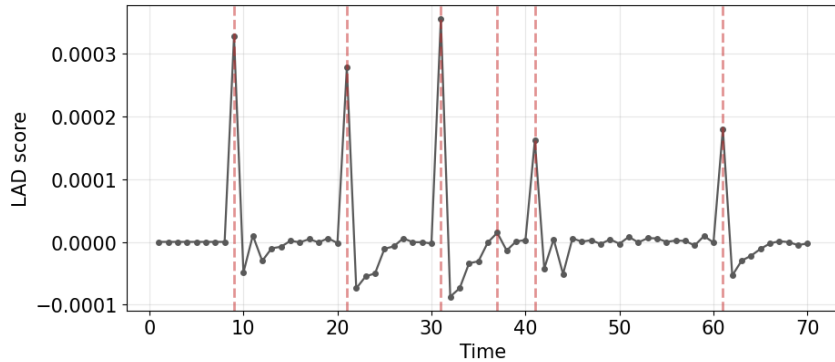


Figure I.14: Change points detected by LAD for Dataset 2. The gray curve shows the raw score. Vertical red dashed lines indicate the detected change points.

The weaker performance of Euclidean Mirror is also consistent with its design. Since it primarily tracks the direction of maximal variation, it tends to emphasize only the dominant mode of temporal change. As a result, more subtle or secondary modes are easily overlooked. This can be seen in Figure I.15, where the method appears to respond mainly to the first mode.

HCDL is more structured than single score methods because it targets changes at different levels of a latent variable model (See Figure I.16). However, these levels do not correspond to the geometric modes of temporal variation that drive our setting. As a result, when multiple heterogeneous events occur across different population trajectories, HCDL is less naturally aligned with precise eventwise localization than the proposed multiscale trajectory method.

DeltaCon performs worse in this setting because it is designed as a pairwise graph similarity measure rather than a multievent localization method. It summarizes the difference between consecutive graphs through a single global affinity based score, which is effective for detecting whether a change occurred but is less well suited for separating several distinct structural events over time. As a result, changes arising from different latent modes can be blended into one aggregate signal, making weaker events harder to localize accurately (See Figure I.17).

Overall, these results show that the proposed multiscale trajectory construction not only detects the presence of multiple changes reliably, but also localizes them more accurately than competing approaches in this challenging heterogeneous setting.

We also report the computational complexity of the compared methods in Table I.18. The proposed MENT procedure has the same leading order time complexity as the spectral embedding based baselines, such as LAD and Euclidean Mirror, namely $O(n^2dT)$. Its space complexity is $O(ndT)$, reflecting the storage of time-indexed embeddings used to construct the multiscale trajectories. Thus, MENT remains computationally comparable to the strongest embedding based competitors while providing additional mode-wise decomposition, attribution, and change point localization capabilities.

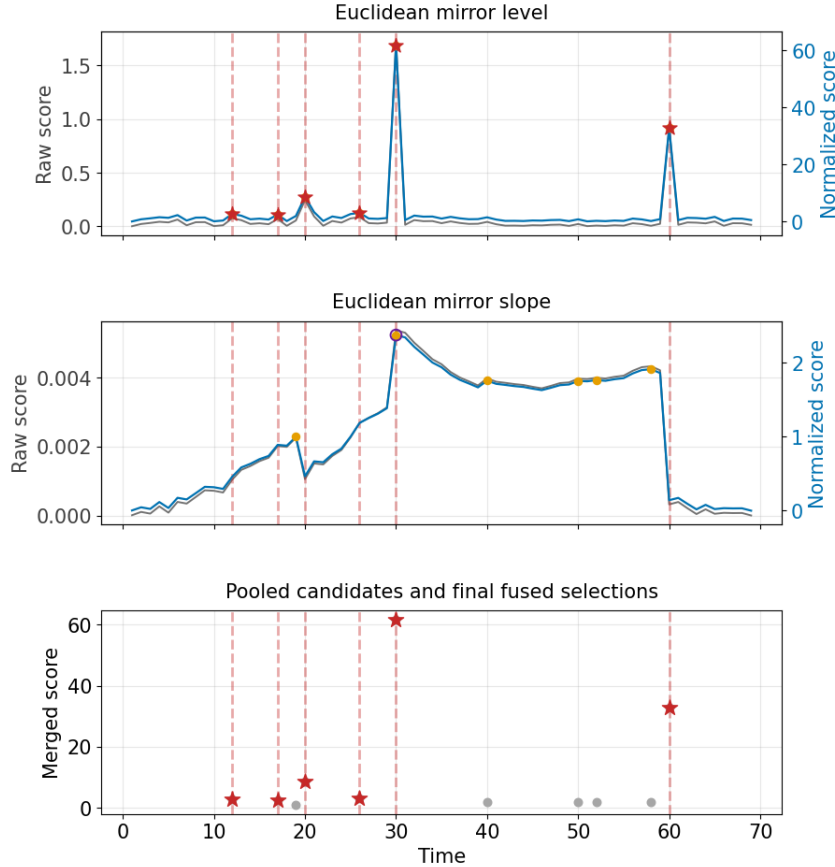


Figure I.15: Change points detected by Euclidean Mirror for Dataset 2. The gray curve shows the raw score for one stream. The blue curve shows the normalized score used for fusion. Orange circles denote that streams top- K candidate change points. Red stars mark candidate times that are selected in the final fused top K and for which the current stream provides the winning score. Purple hollow circles mark candidate times that are selected globally but whose winning score comes from a different stream. Vertical red dashed lines indicate the final fused change points. The bottom panel shows the pooled candidate set obtained by taking the union of the per stream top K candidates and merging them by the fusion rule. Red stars indicate the final selected change points.

All reported runs were executed on a single CPU workstation with two Intel Xeon Gold 6338 CPUs, 64 physical cores in total, 2.0 TiB of RAM, and no GPU. The machine ran Ubuntu 20.04 with Linux 5.15. The code was run with Python 3.13.1, NumPy/SciPy, and the OpenBLAS 0.3.31 LP64 backend. BLAS thread counts were left at their default settings. The largest run, the U.S. court opinions experiment with $T = 80$, $n = 9399$, and 16,716,425 edge instances, took 27.5 minutes end to end; its largest persisted artifact was 67.7 GB. The Enron experiment with $T = 165$, $n = 150$, and 14,500 edge instances took 83 seconds end to end, with a largest persisted artifact of 1.3 GB. The synthetic Dataset 2 run with $T = 70$, $n = 500$, and 2,488,628 edge instances took 17 seconds end to end, with a largest persisted artifact of 0.8 GB. Peak resident memory was not directly recorded.

I.8 Construction of the Real-World Legal Citation Network

We construct the legal citation network from the CourtListener bulk case law snapshots, which are released as quarterly CSV exports of the underlying database rather than as incremental updates [20]. We use the opinion clusters and opinions tables from the May 6, 2024 bulk release. The opinion clusters table provides metadata for groups of related opinions, including filing dates, while the opinions table provides the corresponding opinion texts.

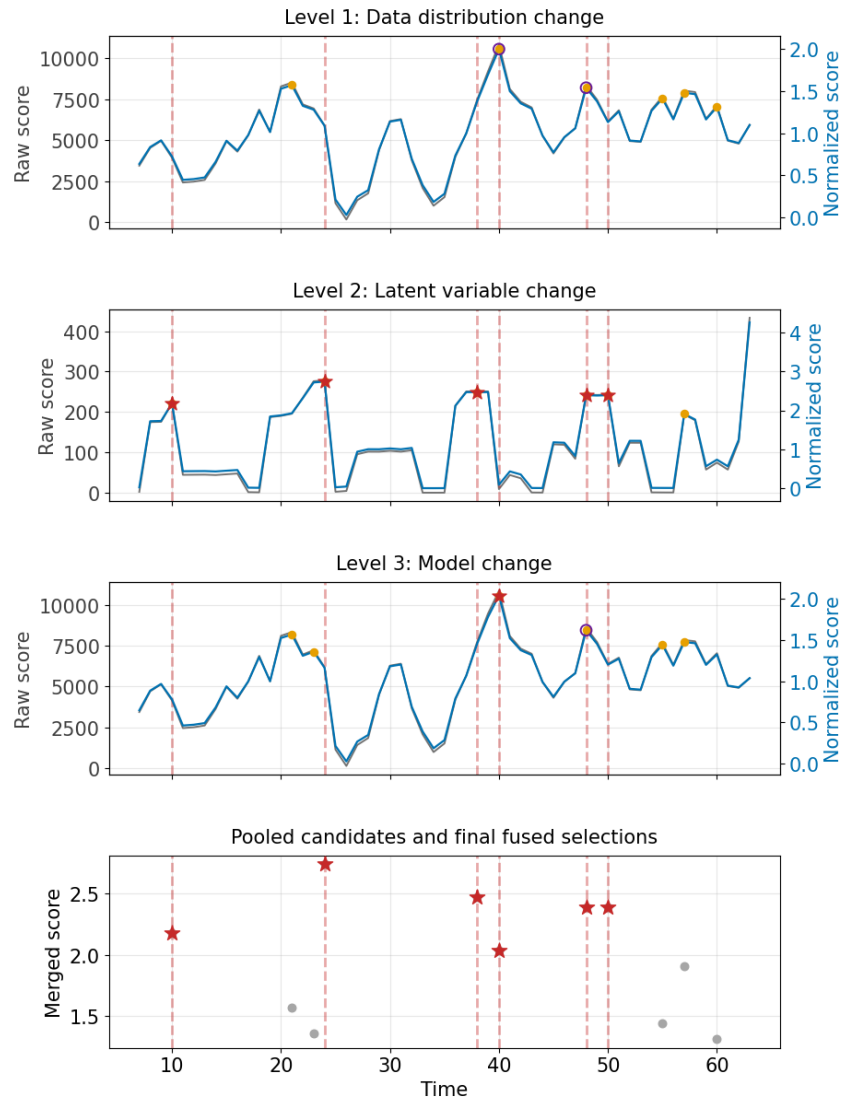


Figure I.16: Change points detected by HCDL for Dataset 2. Gray lines show raw scores, blue lines show normalized fusion scores, orange circles show per level top K candidates, red stars show final fused selections attributed to the current level, and purple hollow circles show globally selected candidates whose winning score comes from another level. Red dashed vertical lines mark the final fused changepoints. The bottom panel summarizes the merged pooled candidates and final selections.

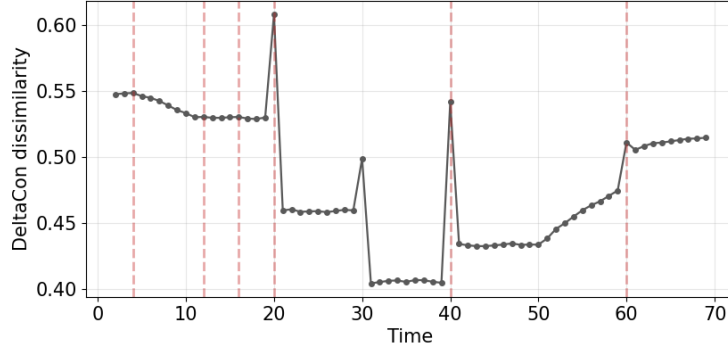


Figure I.17: Change points detected by DeltaCon for Dataset 2. The gray curve shows the raw score. Vertical red dashed lines indicate the detected change points.

Method	Time Complexity	Space Complexity
DeltaCon	$O(mT)$	$O(m)$
LAD	$O(n^2 dT)$	$O(nd)$
HCDL	$O(n^2 K^2 hT)$	$O(nK)$
Mirror	$O(n^2 dT)$	$O(ndT)$
Two stage	$O(n^3)$	$O(n^2)$
MENT	$O(n^2 dT)$	$O(ndT)$

Figure I.18: Computational complexity comparison of the compared methods. Here, T , n and m represent the number of time points, the number of nodes, and the maximum number of edges per snapshot. d , K and h represent the embedding dimension, the maximum number of clusters and the window size. We assume that $n \gg T, d, K, h$.

The preprocessing pipeline has three main stages. First, we extract the mapping from each opinion to its parent opinion cluster and the filing date associated with that cluster, linking each opinion level text record to filing time metadata. Second, we process the opinion texts to extract legal references. For each opinion, we select the first available substantive text field among the available plain text, HTML, and XML fields, after cleaning the text and requiring a minimum length of 1,000 characters. We then apply `eyecite` [29] to identify legal citations and retain only normalized references passing strict filtering rules. Case citations are required to match a reporter style pattern, statutory citations are required to contain both a section symbol and a digit, and non-substantive citation strings such as “Id.” and “supra” are removed. We also separately extract references to U.S. constitutional amendments and normalize them to canonical forms, such as “U.S. Const. amend. XIV”. Opinions are retained only if they contain at least two extracted references in total, counting both legal citations and amendment references.

The resulting intermediate object is an opinion level reference dataset. Each source opinion is associated with its filing date, a deduplicated set of normalized cited authorities, and any normalized constitutional amendment references.

The full set of authorities cited at least once across the entire corpus is heavy tailed and contains a long tail of essentially singleton references that carry little signal for a temporal embedding. We therefore impose two complementary restrictions on the data before constructing the network. First, we restrict the set of admissible authorities (i.e. candidate nodes). We partition the corpus into ten year filing windows and, within each window, retain only the top 1,000 most frequently cited authorities by raw within-window citation count. The union of these per decade top 1,000 sets defines the candidate authority pool, which is fixed across all years. Each opinion’s cited authority set is then intersected with this pool, and any opinion left with fewer than two surviving references is discarded.

Following Matsumoto et al. [30], we then treat the set of authorities cited by each opinion (after the restrictions above) as a hyperedge. Aggregating these hyperedges by filing year yields a yearly legal

citation hypergraph. Finally, we apply clique expansion within each yearly hypergraph to obtain an undirected network for each year.

We focus on the period 1939–2018, yielding 80 yearly snapshots. In aggregate, the network contains roughly 9.4k distinct authorities, on the order of 3.2M distinct undirected co-citation pairs, and about 1.7×10^7 edge instances when summed with multiplicity across years. Individual yearly snapshots are large, locally clustered graphs, each typically containing a few thousand active authorities and on the order of 10^5 edges. Both the active node set and the edge count grow over time as more case law is filed.

All code needed to reproduce the dataset construction is provided in the supplementary material. Because the resulting network files are large, they are not included in the supplementary archive. We will make them available online upon acceptance.

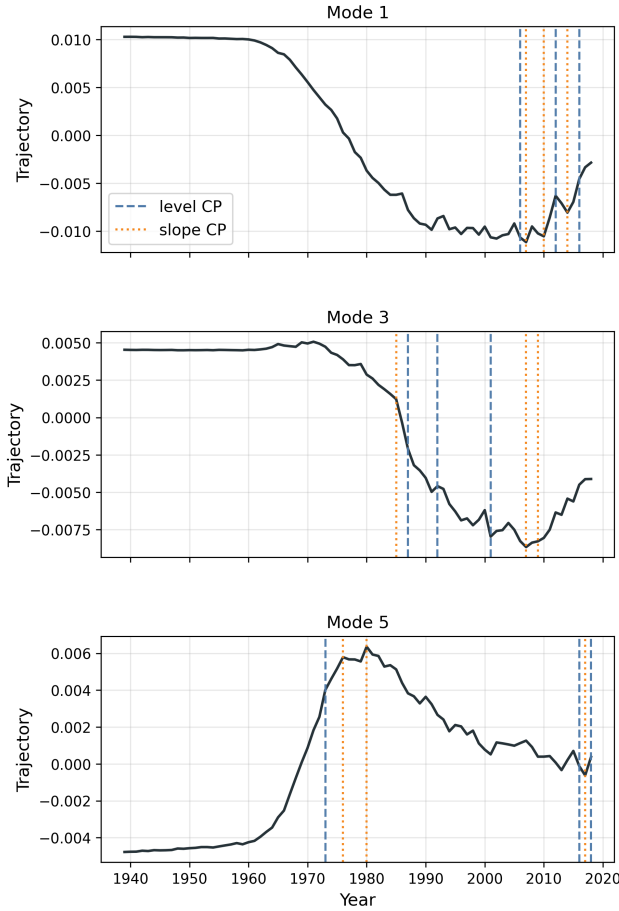


Figure I.19: Trajectories of the selected modes for the U.S. Court opinions data.

I.9 Detailed Analysis of the Real World Legal Citation Network

This section explains how we interpret the legal citation modes shown in the main text. Each learned mode has a positive side and a negative side. For mode k and a time comparison (t, s) , we define the signed node attribution of reporter node i by

$$\hat{a}_{i,k}(t, s) = \frac{1}{\sqrt{n}} \left\langle \hat{\mathbf{Y}}_i(t) - \hat{\mathbf{Y}}_i(s), \hat{\mathbf{u}}_k \right\rangle.$$

These attributions decompose the squared mode-wise variation:

$$\hat{d}_k(\hat{\mathbf{Y}}(t), \hat{\mathbf{Y}}(s))^2 = \sum_{i=1}^n \hat{a}_{i,k}(t, s)^2.$$

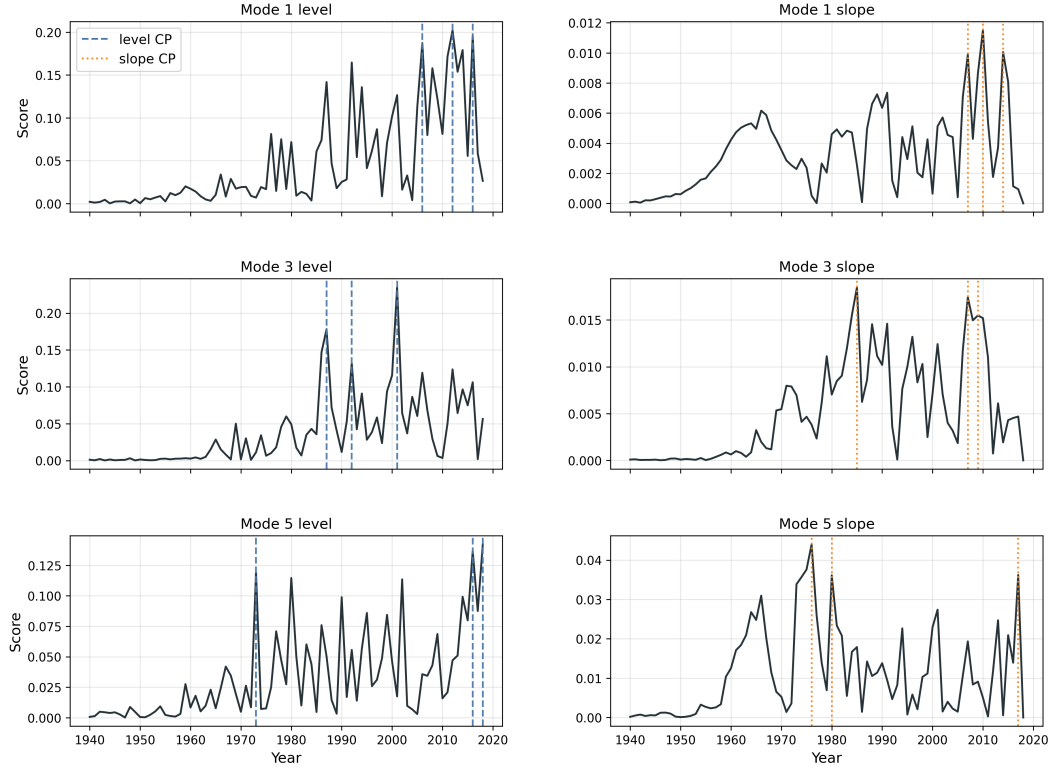


Figure I.20: Trajectories of the selected modes for the U.S. Court opinions data.

Nodes with large positive values of $\hat{a}_{i,k}(t, s)$ form the positive side of the mode at that time comparison, while nodes with large negative values form the negative side.

At each detected level change point, we identify the reporter citations with the largest positive and negative node attributions. These citations tell us which cases contribute most strongly to the movement of that mode at that time. We then ask whether the positive and negative sides correspond to recognizable legal clusters.

The analysis below focuses on level change attributions, corresponding to the 0th order scores plotted in the main text. The same attribution procedure can also be applied to slope change scores by applying it to changes in the trajectory increments rather than to level shifts. We do not interpret those slope attributions here because the main text case study is organized around level shifts. For both real-world dataset we set $d = 32$.

I.9.1 Mode 1

Table I.4: Mode 1 attribution table. For each change point, TOP rows report the most positively attributed reporter nodes and BOTTOM rows report the most negatively attributed reporter nodes.

CP rank	Year	Side	Reporter cite	Score	Case
1	2012	TOP	47 L.Ed.2d 128	0.08947	<i>Imbler v. Pachtman</i> , 424 U.S. 409 (1976)
1	2012	TOP	104 L.Ed.2d 443	0.08912	<i>Graham v. Connor</i> , 490 U.S. 386 (1989)
1	2012	TOP	96 S.Ct. 984	0.08782	<i>Imbler v. Pachtman</i> , 424 U.S. 409 (1976)
1	2012	TOP	3 L.Ed.2d 1217	0.08277	<i>Napue v. Illinois</i> , 360 U.S. 264 (1959)
1	2012	TOP	79 S.Ct. 1173	0.08237	<i>Napue v. Illinois</i> , 360 U.S. 264 (1959)
1	2012	TOP	112 S.Ct. 475	0.07287	<i>Estelle v. McGuire</i> , 502 U.S. 62 (1991)
1	2012	TOP	467 U.S. 431	0.07248	<i>Nix v. Williams</i> , 467 U.S. 431 (1984)
1	2012	TOP	64 L.Ed.2d 497	0.07098	<i>United States v. Mendenhall</i> , 446 U.S. 544 (1980)

Continued on next page

CP rank	Year	Side	Reporter cite	Score	Case
1	2012	TOP	100 S.Ct. 1870	0.07098	<i>United States v. Mendenhall</i> , 446 U.S. 544 (1980)
1	2012	TOP	116 L.Ed.2d 385	0.06818	<i>Estelle v. McGuire</i> , 502 U.S. 62 (1991)
1	2012	BOTTOM	45 S.Ct. 280	-0.04782	<i>Carroll v. United States</i> , 267 U.S. 132 (1925)
1	2012	BOTTOM	50 L.Ed.2d 450	-0.04905	<i>Village of Arlington Heights v. Metropolitan Housing Development Corp.</i> , 429 U.S. 252 (1977)
1	2012	BOTTOM	97 S.Ct. 555	-0.04924	<i>Village of Arlington Heights v. Metropolitan Housing Development Corp.</i> , 429 U.S. 252 (1977)
1	2012	BOTTOM	155 L.Ed.2d 144	-0.05175	<i>Lockyer v. Andrade</i> , 538 U.S. 63 (2003)
1	2012	BOTTOM	111 S.Ct. 1246	-0.05285	<i>Arizona v. Fulminante</i> , 499 U.S. 279 (1991)
1	2012	BOTTOM	113 L.Ed.2d 302	-0.05285	<i>Arizona v. Fulminante</i> , 499 U.S. 279 (1991)
1	2012	BOTTOM	499 U.S. 279	-0.05689	<i>Arizona v. Fulminante</i> , 499 U.S. 279 (1991)
1	2012	BOTTOM	412 U.S. 218	-0.05839	<i>Schneckloth v. Bustamonte</i> , 412 U.S. 218 (1973)
1	2012	BOTTOM	105 S.Ct. 2633	-0.06366	<i>Caldwell v. Mississippi</i> , 472 U.S. 320 (1985)
1	2012	BOTTOM	86 L.Ed.2d 231	-0.06366	<i>Caldwell v. Mississippi</i> , 472 U.S. 320 (1985)
2	2016	TOP	105 S.Ct. 3249	0.09473	<i>City of Cleburne v. Cleburne Living Center, Inc.</i> , 473 U.S. 432 (1985)
2	2016	TOP	6 L.Ed.2d 1081	0.08627	<i>Mapp v. Ohio</i> , 367 U.S. 643 (1961)
2	2016	TOP	104 L.Ed.2d 443	0.08290	<i>Graham v. Connor</i> , 490 U.S. 386 (1989)
2	2016	TOP	109 S.Ct. 1865	0.08283	<i>Graham v. Connor</i> , 490 U.S. 386 (1989)
2	2016	TOP	161 L.Ed.2d 1	0.07755	<i>Roper v. Simmons</i> , 543 U.S. 551 (2005)
2	2016	TOP	95 L.Ed.2d 697	0.07237	<i>United States v. Salerno</i> , 481 U.S. 739 (1987)
2	2016	TOP	364 U.S. 479	0.06613	<i>Shelton v. Tucker</i> , 364 U.S. 479 (1960)
2	2016	TOP	125 S.Ct. 1183	0.06515	<i>Roper v. Simmons</i> , 543 U.S. 551 (2005)
2	2016	TOP	48 L.Ed.2d 597	0.06411	<i>Washington v. Davis</i> , 426 U.S. 229 (1976)
2	2016	TOP	81 S.Ct. 1684	0.06394	<i>Mapp v. Ohio</i> , 367 U.S. 643 (1961)
2	2016	BOTTOM	103 S.Ct. 3469	-0.04945	<i>Michigan v. Long</i> , 463 U.S. 1032 (1983)
2	2016	BOTTOM	101 S.Ct. 690	-0.04961	<i>United States v. Cortez</i> , 449 U.S. 411 (1981)
2	2016	BOTTOM	32 L.Ed.2d 612	-0.05059	<i>Adams v. Williams</i> , 407 U.S. 143 (1972)
2	2016	BOTTOM	88 L.Ed.2d 662	-0.05081	<i>Daniels v. Williams</i> , 474 U.S. 327 (1986)
2	2016	BOTTOM	77 L.Ed.2d 1201	-0.05118	<i>Michigan v. Long</i> , 463 U.S. 1032 (1983)
2	2016	BOTTOM	106 S.Ct. 662	-0.05378	<i>Daniels v. Williams</i> , 474 U.S. 327 (1986)
2	2016	BOTTOM	374 U.S. 23	-0.05509	<i>Ker v. California</i> , 374 U.S. 23 (1963)
2	2016	BOTTOM	83 S.Ct. 1623	-0.05962	<i>Ker v. California</i> , 374 U.S. 23 (1963)
2	2016	BOTTOM	9 L.Ed.2d 799	-0.06539	<i>Gideon v. Wainwright</i> , 372 U.S. 335 (1963)
2	2016	BOTTOM	83 S.Ct. 792	-0.06780	<i>Gideon v. Wainwright</i> , 372 U.S. 335 (1963)
3	2006	TOP	473 U.S. 432	0.10705	<i>City of Cleburne v. Cleburne Living Center, Inc.</i> , 473 U.S. 432 (1985)
3	2006	TOP	105 S.Ct. 3249	0.10318	<i>City of Cleburne v. Cleburne Living Center, Inc.</i> , 473 U.S. 432 (1985)
3	2006	TOP	87 L.Ed.2d 313	0.10301	<i>City of Cleburne v. Cleburne Living Center, Inc.</i> , 473 U.S. 432 (1985)
3	2006	TOP	397 U.S. 337	0.06634	<i>Illinois v. Allen</i> , 397 U.S. 337 (1970)
3	2006	TOP	338 U.S. 25	0.06556	<i>Wolf v. Colorado</i> , 338 U.S. 25 (1949)
3	2006	TOP	69 S.Ct. 1359	0.06495	<i>Wolf v. Colorado</i> , 338 U.S. 25 (1949)
3	2006	TOP	93 L.Ed. 1782	0.06495	<i>Wolf v. Colorado</i> , 338 U.S. 25 (1949)
3	2006	TOP	523 U.S. 1	0.06156	<i>Spencer v. Kemna</i> , 523 U.S. 1 (1998)
3	2006	TOP	519 U.S. 33	0.05660	<i>Ohio v. Robinette</i> , 519 U.S. 33 (1996)
3	2006	TOP	501 U.S. 429	0.05525	<i>Florida v. Bostick</i> , 501 U.S. 429 (1991)
3	2006	BOTTOM	37 Cal.4th 428	-0.06259	<i>People v. Partida</i> , 37 Cal. 4th 428 (2005)
3	2006	BOTTOM	36 L.Ed.2d 439	-0.06302	<i>Preiser v. Rodriguez</i> , 411 U.S. 475 (1973)
3	2006	BOTTOM	388 U.S. 293	-0.06440	<i>Stovall v. Denno</i> , 388 U.S. 293 (1967)
3	2006	BOTTOM	80 L.Ed.2d 657	-0.08186	<i>United States v. Cronin</i> , 466 U.S. 648 (1984)
3	2006	BOTTOM	104 S.Ct. 2039	-0.08258	<i>United States v. Cronin</i> , 466 U.S. 648 (1984)
3	2006	BOTTOM	130 L.Ed.2d 808	-0.08436	<i>Schlup v. Delo</i> , 513 U.S. 298 (1995)
3	2006	BOTTOM	115 S.Ct. 851	-0.08436	<i>Schlup v. Delo</i> , 513 U.S. 298 (1995)
3	2006	BOTTOM	513 U.S. 298	-0.08450	<i>Schlup v. Delo</i> , 513 U.S. 298 (1995)
3	2006	BOTTOM	87 S.Ct. 1967	-0.09221	<i>Stovall v. Denno</i> , 388 U.S. 293 (1967)

Continued on next page

CP rank	Year	Side	Reporter cite	Score	Case
3	2006	BOTTOM	18 L.Ed.2d 1199	-0.09426	<i>Stovall v. Denno</i> , 388 U.S. 293 (1967)

Mode 1 has three leading level change points, in 2006, 2012, and 2016. The dates are relatively close to one another, and the same types of authorities recur across the three attribution blocks. We therefore read this mode as a medium term reweighting of citation neighborhoods during the mid 2000s to mid 2010s, rather than as a single isolated legal event.

The main contrast is between two groups of authorities. The positive side is broad, but it is dominated by cases that courts use to state general constitutional standards, rights frameworks, or limits on government action. For example, the 2006 positive block is led by *City of Cleburne v. Cleburne Living Center*, with additional weight on *Wolf v. Colorado*, *Ohio v. Robinette*, and *Florida v. Bostick*. The 2012 positive block shifts toward *Imbler v. Pachtman*, *Graham v. Connor*, *Napue v. Illinois*, *Estelle v. McGuire*, *Nix v. Williams*, and *United States v. Mendenhall*. The 2016 positive block again contains *Cleburne* and *Graham*, together with *Mapp v. Ohio*, *Roper v. Simmons*, *United States v. Salerno*, and *Washington v. Davis*. These cases span equal protection, Fourth Amendment seizure doctrine, excessive force, exclusionary rule incorporation, habeas review, prosecutorial misconduct, punishment, and preventive detention. Thus, the positive side should not be described as one narrow doctrine. What the table supports is a broader characterization: this side collects authorities that articulate constitutional standards and remedial limits across several areas of public-law and criminal-adjudication doctrine.

The negative side is more concentrated in criminal procedure and post-conviction review. In 2006, the largest negative attributions are *Stovall v. Denno*, *Schlup v. Delo*, *United States v. Cronin*, *Preiser v. Rodriguez*, and *People v. Partida*. These cases concern eyewitness identification, habeas gateways, right to counsel, the habeas/Section 1983 boundary, and evidentiary error preservation. In 2012, the negative side contains *Caldwell v. Mississippi*, *Schneekloth v. Bustamonte*, *Arizona v. Fulminante*, *Lockyer v. Andrade*, *Village of Arlington Heights*, and *Carroll v. United States*. In 2016, it contains *Gideon v. Wainwright*, *Ker v. California*, *Daniels v. Williams*, *Michigan v. Long*, *Adams v. Williams*, and *United States v. Cortez*. This side is therefore more visibly tied to criminal adjudication: right to counsel, search and seizure, consent, reasonable suspicion, coerced confessions, habeas review, and post-conviction standards.

The change point is understandable because the same broad opposition appears at all three peaks. Mode 1 does not simply pick up one famous case or one doctrinal category. Instead, it repeatedly places a broad constitutional standards group on the positive side and a more procedure specific criminal adjudication group on the negative side. The 2006 peak is driven especially by *Cleburne* on the positive side and *Stovall/Schlup/Cronic* on the negative side. The 2012 peak adds a different set of positive authorities involving prosecutorial immunity, excessive force, false testimony, habeas limits, and seizure doctrine, while the negative side emphasizes capital sentencing, consent searches, coerced confessions, and habeas proportionality review. The 2016 peak returns to the same larger contrast, with *Cleburne*, *Mapp*, *Graham*, and *Roper* on the positive side and *Gideon*, *Ker*, *Daniels*, *Long*, and *Cortez* on the negative side.

We therefore interpret Mode 1 as a broad reweighting between two citation neighborhoods: a positive neighborhood of general constitutional standards and authorities concerning rights and remedies, and a negative neighborhood more anchored in criminal procedure and post conviction doctrine. The timing of these changes is also consistent with the early and middle years of the Roberts Court, during which the Court repeatedly addressed the remedial and procedural consequences of constitutional criminal adjudication claims, including habeas review, exclusionary rule doctrine, ineffective assistance, sentencing, and collateral review. This context is relevant because many of these decisions did not simply ask whether a constitutional right existed in the abstract. They also asked whether an alleged violation justified suppression, reversal, collateral relief, or reopening of a criminal judgment. In that sense, the period placed greater emphasis on finality, deference to prior adjudication, harmless error, procedural default, and the limits of available remedies. We do not treat the mode as identifying the Roberts Court as a single causal source of the shift. Rather, the Roberts Court context helps explain why the criminal procedure and post-conviction side of this citation contrast may have become more salient during this period.

I.9.2 Mode 3

Table I.5: Mode 3 attribution table. For each change point, TOP rows report the most positively attributed reporter nodes and BOTTOM rows report the most negatively attributed reporter nodes.

CP rank	Year	Side	Reporter cite	Score	Case
1	2001	TOP	102 S.Ct. 2727	0.06780	<i>Harlow v. Fitzgerald</i> , 457 U.S. 800 (1982)
1	2001	TOP	73 L.Ed.2d 396	0.06778	<i>Harlow v. Fitzgerald</i> , 457 U.S. 800 (1982)
1	2001	TOP	448 U.S. 98	0.05388	<i>Rawlings v. Kentucky</i> , 448 U.S. 98 (1980)
1	2001	TOP	86 L.Ed.2d 411	0.05083	<i>Mitchell v. Forsyth</i> , 472 U.S. 511 (1985)
1	2001	TOP	105 S.Ct. 2806	0.05064	<i>Mitchell v. Forsyth</i> , 472 U.S. 511 (1985)
1	2001	TOP	428 U.S. 242	0.04152	<i>Proffitt v. Florida</i> , 428 U.S. 242 (1976)
1	2001	TOP	49 L.Ed.2d 913	0.04139	<i>Proffitt v. Florida</i> , 428 U.S. 242 (1976)
1	2001	TOP	96 S.Ct. 2960	0.04055	<i>Proffitt v. Florida</i> , 428 U.S. 242 (1976)
1	2001	TOP	59 L.Ed.2d 660	0.03933	<i>Delaware v. Prouse</i> , 440 U.S. 648 (1979)
1	2001	TOP	150 L.Ed.2d 272	0.03826	<i>Saucier v. Katz</i> , 533 U.S. 194 (2001)
1	2001	BOTTOM	462 U.S. 696	-0.03869	<i>United States v. Place</i> , 462 U.S. 696 (1983)
1	2001	BOTTOM	88 S.Ct. 1556	-0.03912	<i>Carafas v. LaVallee</i> , 391 U.S. 234 (1968)
1	2001	BOTTOM	13 L.Ed.2d 684	-0.03917	<i>United States v. Ventresca</i> , 380 U.S. 102 (1965)
1	2001	BOTTOM	20 L.Ed.2d 554	-0.03977	<i>Carafas v. LaVallee</i> , 391 U.S. 234 (1968)
1	2001	BOTTOM	85 S.Ct. 741	-0.03989	<i>United States v. Ventresca</i> , 380 U.S. 102 (1965)
1	2001	BOTTOM	92 L.Ed. 436	-0.04120	<i>Johnson v. United States</i> , 333 U.S. 10 (1948)
1	2001	BOTTOM	68 S.Ct. 367	-0.04148	<i>Johnson v. United States</i> , 333 U.S. 10 (1948)
1	2001	BOTTOM	442 U.S. 200	-0.04529	<i>Dunaway v. New York</i> , 442 U.S. 200 (1979)
1	2001	BOTTOM	102 S.Ct. 2157	-0.05316	<i>United States v. Ross</i> , 456 U.S. 798 (1982)
1	2001	BOTTOM	72 L.Ed.2d 572	-0.05335	<i>United States v. Ross</i> , 456 U.S. 798 (1982)
2	1987	TOP	100 S.Ct. 1870	0.05454	<i>United States v. Mendenhall</i> , 446 U.S. 544 (1980)
2	1987	TOP	64 L.Ed.2d 497	0.05372	<i>United States v. Mendenhall</i> , 446 U.S. 544 (1980)
2	1987	TOP	446 U.S. 544	0.05360	<i>United States v. Mendenhall</i> , 446 U.S. 544 (1980)
2	1987	TOP	415 U.S. 164	0.04358	<i>United States v. Matlock</i> , 415 U.S. 164 (1974)
2	1987	TOP	63 L.Ed.2d 639	0.04294	<i>Payton v. New York</i> , 445 U.S. 573 (1980)
2	1987	TOP	100 S.Ct. 1371	0.04294	<i>Payton v. New York</i> , 445 U.S. 573 (1980)
2	1987	TOP	461 U.S. 352	0.04262	<i>Kolender v. Lawson</i> , 461 U.S. 352 (1983)
2	1987	TOP	103 S.Ct. 1855	0.04186	<i>Kolender v. Lawson</i> , 461 U.S. 352 (1983)
2	1987	TOP	445 U.S. 573	0.04041	<i>Payton v. New York</i> , 445 U.S. 573 (1980)
2	1987	TOP	29 L.Ed.2d 564	0.04002	<i>Coolidge v. New Hampshire</i> , 403 U.S. 443 (1971)
2	1987	BOTTOM	94 S.Ct. 613	-0.04170	<i>United States v. Calandra</i> , 414 U.S. 338 (1974)
2	1987	BOTTOM	414 U.S. 338	-0.04187	<i>United States v. Calandra</i> , 414 U.S. 338 (1974)
2	1987	BOTTOM	38 L.Ed.2d 561	-0.04248	<i>United States v. Calandra</i> , 414 U.S. 338 (1974)
2	1987	BOTTOM	10 L.Ed.2d 726	-0.04630	<i>Ker v. California</i> , 374 U.S. 23 (1963)
2	1987	BOTTOM	6 S.Ct. 524	-0.04670	<i>Boyd v. United States</i> , 116 U.S. 616 (1886)
2	1987	BOTTOM	374 U.S. 23	-0.04972	<i>Ker v. California</i> , 374 U.S. 23 (1963)
2	1987	BOTTOM	83 S.Ct. 1623	-0.04972	<i>Ker v. California</i> , 374 U.S. 23 (1963)
2	1987	BOTTOM	100 S.Ct. 2556	-0.05570	<i>Rawlings v. Kentucky</i> , 448 U.S. 98 (1980)
2	1987	BOTTOM	65 L.Ed.2d 633	-0.05574	<i>Rawlings v. Kentucky</i> , 448 U.S. 98 (1980)
2	1987	BOTTOM	448 U.S. 98	-0.05624	<i>Rawlings v. Kentucky</i> , 448 U.S. 98 (1980)
3	1992	TOP	102 S.Ct. 2157	0.05455	<i>United States v. Ross</i> , 456 U.S. 798 (1982)
3	1992	TOP	72 L.Ed.2d 572	0.05443	<i>United States v. Ross</i> , 456 U.S. 798 (1982)
3	1992	TOP	456 U.S. 798	0.05280	<i>United States v. Ross</i> , 456 U.S. 798 (1982)
3	1992	TOP	89 S.Ct. 1394	0.04452	<i>Davis v. Mississippi</i> , 394 U.S. 721 (1969)
3	1992	TOP	22 L.Ed.2d 676	0.04446	<i>Davis v. Mississippi</i> , 394 U.S. 721 (1969)
3	1992	TOP	394 U.S. 721	0.04378	<i>Davis v. Mississippi</i> , 394 U.S. 721 (1969)
3	1992	TOP	83 S.Ct. 1381	0.04149	<i>Lopez v. United States</i> , 373 U.S. 427 (1963)
3	1992	TOP	10 L.Ed.2d 462	0.04149	<i>Lopez v. United States</i> , 373 U.S. 427 (1963)
3	1992	TOP	373 U.S. 427	0.04149	<i>Lopez v. United States</i> , 373 U.S. 427 (1963)
3	1992	TOP	115 L.Ed.2d 389	0.03994	<i>Florida v. Bostick</i> , 501 U.S. 429 (1991)
3	1992	BOTTOM	85 S.Ct. 741	-0.04382	<i>United States v. Ventresca</i> , 380 U.S. 102 (1965)
3	1992	BOTTOM	362 U.S. 257	-0.04417	<i>Jones v. United States</i> , 362 U.S. 257 (1960)

Continued on next page

CP rank	Year	Side	Reporter cite	Score	Case
3	1992	BOTTOM	13 L.Ed.2d 684	-0.04477	<i>United States v. Ventresca</i> , 380 U.S. 102 (1965)
3	1992	BOTTOM	80 S.Ct. 725	-0.04590	<i>Jones v. United States</i> , 362 U.S. 257 (1960)
3	1992	BOTTOM	4 L.Ed.2d 697	-0.04725	<i>Jones v. United States</i> , 362 U.S. 257 (1960)
3	1992	BOTTOM	94 S.Ct. 467	-0.05239	<i>United States v. Robinson</i> , 414 U.S. 218 (1973)
3	1992	BOTTOM	38 L.Ed.2d 427	-0.05239	<i>United States v. Robinson</i> , 414 U.S. 218 (1973)
3	1992	BOTTOM	414 U.S. 218	-0.05266	<i>United States v. Robinson</i> , 414 U.S. 218 (1973)
3	1992	BOTTOM	66 L.Ed.2d 621	-0.05578	<i>United States v. Cortez</i> , 449 U.S. 411 (1981)
3	1992	BOTTOM	101 S.Ct. 690	-0.05688	<i>United States v. Cortez</i> , 449 U.S. 411 (1981)

Mode 3 is a focused criminal procedure mode. Its three leading level change points occur in 1987, 1992, and 2001, and the high attribution nodes are concentrated in Fourth Amendment search and seizure doctrine and related police litigation doctrine. Unlike Mode 1, this mode does not span broad constitutional fields. The attribution table instead shows a more local structure inside police conduct law.

The positive side of Mode 3 generally contains cases about police citizen encounters, third party consent, home entry, automobile or field searches, bus sweep encounters, and qualified immunity. The negative side generally contains cases about Fourth Amendment standing, warrant review, custodial or investigative detention, exclusionary rule limits, search incident to arrest, and older search and seizure doctrine. The mode therefore separates different groups of cases used to define the legal boundary of police conduct.

The 1987 change point gives the first version of this separation. The positive side is led by *United States v. Mendenhall*, *United States v. Matlock*, *Payton v. New York*, *Kolender v. Lawson*, and *Coolidge v. New Hampshire*. These cases concern police citizen encounters, third party consent, home entry for arrest, stop and identify doctrine, and search and seizure limits. The negative side is led by *Rawlings v. Kentucky*, *Ker v. California*, *Boyd v. United States*, and *United States v. Calandra*. These cases emphasize Fourth Amendment standing, state search and seizure standards, older search and self incrimination doctrine, and limits on the exclusionary rule. Thus, the 1987 peak contrasts encounter, consent, and home entry cases with standing, older search doctrine, and exclusionary rule cases.

The 1992 change point remains within Fourth Amendment doctrine but shifts to a different set of police conduct cases. The positive side is dominated by *United States v. Ross*, *Davis v. Mississippi*, *Lopez v. United States*, and *Florida v. Bostick*. These cases involve automobile searches, investigative detention for fingerprinting, participant monitoring, and bus sweep seizure analysis. The negative side is dominated by *United States v. Cortez*, *United States v. Robinson*, *Jones v. United States*, and *United States v. Ventresca*, which concern reasonable suspicion, search incident to arrest, Fourth Amendment standing, and warrant affidavit review. The 1992 peak therefore contrasts automobile search and mobile encounter cases with reasonable suspicion, search incident, standing, and warrant review cases.

The 2001 change point adds an explicit police litigation component. The positive side is led by *Harlow v. Fitzgerald*, *Mitchell v. Forsyth*, *Rawlings v. Kentucky*, *Delaware v. Prouse*, and *Saucier v. Katz*, with *Proffitt v. Florida* appearing as a smaller capital sentencing component. This side combines qualified immunity doctrine with Fourth Amendment standing and automobile stop doctrine. The negative side is led by *United States v. Ross*, *Dunaway v. New York*, *Johnson v. United States*, *United States v. Ventresca*, *Carafas v. LaVallee*, and *United States v. Place*. These cases concern automobile searches, custodial detention, warrant requirements, warrant affidavit review, habeas mootness, and investigative detention of luggage. The 2001 peak therefore differs from the 1987 and 1992 peaks because qualified immunity cases become central to the positive side of the mode.

The timing of these peaks is legally plausible. The 1987 peak occurs in the same year as *Anderson v. Creighton*, where the Court applied qualified immunity to a Fourth Amendment warrantless search claim and held that the allegedly violated right must be clearly established at a factually specific level [31]. The 1992 peak is consistent with the reorganization of police encounter and automobile search doctrine around this period. Contemporary commentary described the Court as reshaping the boundary between regulated seizures and unregulated police citizen encounters [32], and the Court had recently clarified automobile search and bus encounter doctrine in *California v. Acevedo* and

Florida v. Bostick [33, 34]. The 2001 peak aligns with *Saucier v. Katz*, where the Court required courts to ask first whether the facts show a constitutional violation and then whether the right was clearly established [35]. Later scholarship describes this Wilson–Saucier sequencing rule as shaping how lower courts articulated constitutional rights in qualified immunity cases [36]. More broadly, Kinports characterizes the Supreme Court’s qualified immunity jurisprudence as a “quiet expansion,” which supports reading the 1987 and 2001 peaks as part of an incremental doctrinal development rather than as a response to a single triggering event [37].

This provides a network interpretation of the mode. Mode 3 is not simply detecting Fourth Amendment doctrine as a single block. Instead, it shows that different Fourth Amendment case groups are reorganized with different neighboring cases over time. In 1987, encounter, consent, and entry cases separate from standing, older search doctrine, and exclusionary rule cases. In 1992, automobile search and mobile encounter cases separate from reasonable suspicion, search incident, standing, and warrant review cases. By 2001, qualified immunity cases such as *Harlow*, *Mitchell*, and *Saucier* appear on the same side as Fourth Amendment police conduct cases such as *Rawlings* and *Prouse*. The resulting network change is that Fourth Amendment cases are no longer organized only around merits questions about searches and seizures; they also become linked to the civil litigation question whether the relevant right was clearly established enough to support damages liability against officers.

Overall, Mode 3 is best interpreted as a Fourth Amendment and police litigation reweighting. The positive side generally emphasizes encounter, consent, home entry, automobile search, field search, and qualified immunity precedents. The negative side generally emphasizes standing, warrant review, detention, exclusionary rule limits, search incident to arrest, and older search and seizure precedents. The main finding is that Mode 3 separates citation neighborhoods inside criminal procedure and shows how the network organization of police conduct doctrine changes: encounter and consent cases cluster apart from standing and warrant cases; automobile and mobile encounter cases cluster apart from reasonable suspicion and search incident cases; and, by 2001, Fourth Amendment police conduct cases are linked to qualified immunity cases governing the clearly established law requirement.

I.9.3 Mode 5

Table I.6: Mode 5 attribution table. For each change point, TOP rows report the most positively attributed reporter nodes and BOTTOM rows report the most negatively attributed reporter nodes.

CP rank	Year	Side	Reporter cite	Score	Case
1	2018	TOP	112 S.Ct. 475	0.04112	<i>Estelle v. McGuire</i> , 502 U.S. 62 (1991)
1	2018	TOP	103 L.Ed.2d 249	0.03544	<i>DeShaney v. Winnebago County Department of Social Services</i> , 489 U.S. 189 (1989)
1	2018	TOP	109 S.Ct. 998	0.03497	<i>DeShaney v. Winnebago County Department of Social Services</i> , 489 U.S. 189 (1989)
1	2018	TOP	116 L.Ed.2d 385	0.03422	<i>Estelle v. McGuire</i> , 502 U.S. 62 (1991)
1	2018	TOP	140 L.Ed.2d 1043	0.03008	<i>County of Sacramento v. Lewis</i> , 523 U.S. 833 (1998)
1	2018	TOP	3 L.Ed.2d 1217	0.02998	<i>Napue v. Illinois</i> , 360 U.S. 264 (1959)
1	2018	TOP	121 S.Ct. 2151	0.02985	<i>Saucier v. Katz</i> , 533 U.S. 194 (2001)
1	2018	TOP	150 L.Ed.2d 272	0.02980	<i>Saucier v. Katz</i> , 533 U.S. 194 (2001)
1	2018	TOP	107 S.Ct. 2095	0.02977	<i>United States v. Salerno</i> , 481 U.S. 739 (1987)
1	2018	TOP	95 L.Ed.2d 697	0.02895	<i>United States v. Salerno</i> , 481 U.S. 739 (1987)
1	2018	BOTTOM	8 L.Ed.2d 758	-0.02110	<i>Robinson v. California</i> , 370 U.S. 660 (1962)
1	2018	BOTTOM	99 S.Ct. 970	-0.02121	<i>Montana v. United States</i> , 440 U.S. 147 (1979)
1	2018	BOTTOM	96 L.Ed.2d 440	-0.02386	<i>Booth v. Maryland</i> , 482 U.S. 496 (1987)
1	2018	BOTTOM	71 L.Ed.2d 1	-0.02493	<i>Eddings v. Oklahoma</i> , 455 U.S. 104 (1982)
1	2018	BOTTOM	415 U.S. 452	-0.02547	<i>Steffel v. Thompson</i> , 415 U.S. 452 (1974)
1	2018	BOTTOM	99 S.Ct. 645	-0.02660	<i>Parklane Hosiery Co. v. Shore</i> , 439 U.S. 322 (1979)
1	2018	BOTTOM	58 L.Ed.2d 552	-0.02660	<i>Parklane Hosiery Co. v. Shore</i> , 439 U.S. 322 (1979)
1	2018	BOTTOM	102 S.Ct. 869	-0.02919	<i>Eddings v. Oklahoma</i> , 455 U.S. 104 (1982)

Continued on next page

CP rank	Year	Side	Reporter cite	Score	Case
1	2018	BOTTOM	56 L.Ed.2d 611	-0.03155	<i>Monell v. Department of Social Services</i> , 436 U.S. 658 (1978)
1	2018	BOTTOM	98 S.Ct. 2018	-0.03156	<i>Monell v. Department of Social Services</i> , 436 U.S. 658 (1978)
2	2016	TOP	161 L.Ed.2d 1	0.04108	<i>Roper v. Simmons</i> , 543 U.S. 551 (2005)
2	2016	TOP	96 S.Ct. 2978	0.03862	<i>Woodson v. North Carolina</i> , 428 U.S. 280 (1976)
2	2016	TOP	71 L.Ed.2d 1	0.03833	<i>Eddings v. Oklahoma</i> , 455 U.S. 104 (1982)
2	2016	TOP	428 U.S. 153	0.03504	<i>Gregg v. Georgia</i> , 428 U.S. 153 (1976)
2	2016	TOP	49 L.Ed.2d 944	0.03498	<i>Woodson v. North Carolina</i> , 428 U.S. 280 (1976)
2	2016	TOP	125 S.Ct. 1183	0.03289	<i>Roper v. Simmons</i> , 543 U.S. 551 (2005)
2	2016	TOP	485 U.S. 112	0.03227	<i>City of St. Louis v. Praprotnik</i> , 485 U.S. 112 (1988)
2	2016	TOP	478 U.S. 570	0.03139	<i>Rose v. Clark</i> , 478 U.S. 570 (1986)
2	2016	TOP	96 S.Ct. 2909	0.03015	<i>Gregg v. Georgia</i> , 428 U.S. 153 (1976)
2	2016	TOP	49 L.Ed.2d 859	0.03000	<i>Gregg v. Georgia</i> , 428 U.S. 153 (1976)
2	2016	BOTTOM	971 S.W.2d 402	-0.03203	<i>Maritime Overseas Corp. v. Ellis</i> , 971 S.W.2d 402 (Tex. 1998)
2	2016	BOTTOM	879 S.W.2d 10	-0.03219	<i>Transportation Insurance Co. v. Moriel</i> , 879 S.W.2d 10 (Tex. 1994)
2	2016	BOTTOM	92 S.Ct. 2294	-0.03223	<i>Grayned v. City of Rockford</i> , 408 U.S. 104 (1972)
2	2016	BOTTOM	50 L.Ed.2d 471	-0.03231	<i>Mt. Healthy City School District Board of Education v. Doyle</i> , 429 U.S. 274 (1977)
2	2016	BOTTOM	17 L.Ed.2d 374	-0.03241	<i>Hoffa v. United States</i> , 385 U.S. 293 (1966)
2	2016	BOTTOM	87 S.Ct. 408	-0.03241	<i>Hoffa v. United States</i> , 385 U.S. 293 (1966)
2	2016	BOTTOM	244 S.W.2d 660	-0.03367	<i>In re King's Estate</i> , 244 S.W.2d 660 (Tex. 1951)
2	2016	BOTTOM	650 S.W.2d 61	-0.03376	<i>Kindred v. Con/Chem, Inc.</i> , 650 S.W.2d 61 (Tex. 1983)
2	2016	BOTTOM	715 S.W.2d 629	-0.03630	<i>Pool v. Ford Motor Co.</i> , 715 S.W.2d 629 (Tex. 1986)
2	2016	BOTTOM	922 S.W.2d 126	-0.03719	<i>Clewis v. State</i> , 922 S.W.2d 126 (Tex. Crim. App. 1996)
3	1973	TOP	93 S.Ct. 1278	0.04852	<i>San Antonio Independent School District v. Rodriguez</i> , 411 U.S. 1 (1973)
3	1973	TOP	36 L.Ed.2d 16	0.04798	<i>San Antonio Independent School District v. Rodriguez</i> , 411 U.S. 1 (1973)
3	1973	TOP	411 U.S. 1	0.04597	<i>San Antonio Independent School District v. Rodriguez</i> , 411 U.S. 1 (1973)
3	1973	TOP	93 S.Ct. 1764	0.04308	<i>Frontiero v. Richardson</i> , 411 U.S. 677 (1973)
3	1973	TOP	411 U.S. 677	0.03881	<i>Frontiero v. Richardson</i> , 411 U.S. 677 (1973)
3	1973	TOP	36 L.Ed.2d 583	0.03850	<i>Frontiero v. Richardson</i> , 411 U.S. 677 (1973)
3	1973	TOP	411 U.S. 223	0.03843	<i>Brown v. United States</i> , 411 U.S. 223 (1973)
3	1973	TOP	93 S.Ct. 1565	0.03843	<i>Brown v. United States</i> , 411 U.S. 223 (1973)
3	1973	TOP	93 S.Ct. 2041	0.03679	<i>Schneckloth v. Bustamonte</i> , 412 U.S. 218 (1973)
3	1973	TOP	36 L.Ed.2d 854	0.03675	<i>Schneckloth v. Bustamonte</i> , 412 U.S. 218 (1973)
3	1973	BOTTOM	4 L.Ed.2d 1688	-0.02338	<i>Rios v. United States</i> , 364 U.S. 253 (1960)
3	1973	BOTTOM	355 U.S. 339	-0.02387	<i>Lawn v. United States</i> , 355 U.S. 339 (1958)
3	1973	BOTTOM	84 S.Ct. 1774	-0.02430	<i>Jackson v. Denno</i> , 378 U.S. 368 (1964)
3	1973	BOTTOM	308 U.S. 371	-0.02501	<i>Chicot County Drainage District v. Baxter State Bank</i> , 308 U.S. 371 (1940)
3	1973	BOTTOM	60 S.Ct. 317	-0.02501	<i>Chicot County Drainage District v. Baxter State Bank</i> , 308 U.S. 371 (1940)
3	1973	BOTTOM	2 L.Ed.2d 321	-0.02547	<i>Lawn v. United States</i> , 355 U.S. 339 (1958) (1958)
3	1973	BOTTOM	84 L.Ed. 329	-0.02666	<i>Chicot County Drainage District v. Baxter State Bank</i> , 308 U.S. 371 (1940)
3	1973	BOTTOM	67 S.Ct. 1672	-0.02807	<i>Adamson v. California</i> , 332 U.S. 46 (1947)
3	1973	BOTTOM	91 L.Ed. 1903	-0.02808	<i>Adamson v. California</i> , 332 U.S. 46 (1947)
3	1973	BOTTOM	332 U.S. 46	-0.02981	<i>Adamson v. California</i> , 332 U.S. 46 (1947)

Mode 5 is broader than Modes 1 and 3, but the attribution table still shows a coherent pattern. Its three leading level change points occur in 1973, 2016, and 2018. Unlike Mode 3, this mode is not

centered on Fourth Amendment police conduct. It instead groups cases about federal constitutional claims against government action: when such claims are reviewable, who can be held liable, and what limits apply to punishment or remedies.

The positive side of Mode 5 generally contains cases about habeas limits, substantive due process, state action, preventive detention, qualified immunity, capital punishment, equal protection, and selected criminal procedure rules. The negative side generally contains cases about municipal liability, preclusion, declaratory relief, punishment limits, incorporation, evidentiary sufficiency, and older constitutional criminal procedure. The mode therefore tracks how constitutional claims against government actors are routed through federal review, liability, remedy, and punishment doctrines.

The 1973 change point gives the earliest version of this structure. The positive side is led by *San Antonio Independent School District v. Rodriguez*, *Frontiero v. Richardson*, *Brown v. United States*, and *Schneckloth v. Bustamonte*. These cases combine equal protection, sex discrimination, Fourth Amendment standing, and consent searches. The negative side is led by *Adamson v. California*, *Chicot County Drainage District v. Baxter State Bank*, *Jackson v. Denno*, *Lawn v. United States*, and *Rios v. United States*. These cases involve incorporation, finality of judgments, Eighth Amendment punishment, confession voluntariness, criminal procedure, and search and seizure timing. The 1973 peak therefore contrasts then current equal protection and criminal procedure cases with older constitutional criminal and federal courts cases.

The 2016 change point makes the punishment component of Mode 5 much more visible. The positive side is dominated by *Roper v. Simmons*, *Woodson v. North Carolina*, *Eddings v. Oklahoma*, and *Gregg v. Georgia*. These are central Eighth Amendment and capital sentencing cases. The same side also includes *City of St. Louis v. Praprotnik*, a municipal liability case, and *Rose v. Clark*, a harmless error case. Thus, the positive side links capital punishment doctrine with government liability and criminal review. The negative side is more heterogeneous. It contains several Texas state law sufficiency and evidence review cases, together with *Hoffa v. United States*, *Mt. Healthy City School District Board of Education v. Doyle*, and *Grayned v. City of Rockford*. These cases involve factual sufficiency, informant evidence, retaliation, and First Amendment limits. The 2016 peak should therefore be read as a strong capital punishment and government liability signal on the positive side, against a more mixed procedural and evidentiary sufficiency neighborhood on the negative side.

The 2018 change point is the clearest recent expression of the mode. The positive side is led by *Estelle v. McGuire*, *DeShaney v. Winnebago County Department of Social Services*, *County of Sacramento v. Lewis*, *Napue v. Illinois*, *Saucier v. Katz*, and *United States v. Salerno*. These cases concern limits on federal habeas review, the absence of a general affirmative constitutional duty to protect, substantive due process, false testimony, qualified immunity, and preventive detention. This side is best read as a constitutional claim threshold neighborhood: it concerns when government conduct becomes constitutionally actionable and when federal courts will review or remedy it. The negative side is led by *Monell v. Department of Social Services*, *Eddings v. Oklahoma*, *Parklane Hosiery Co. v. Shore*, *Steffel v. Thompson*, *Booth v. Maryland*, *Montana v. United States*, and *Robinson v. California*. These cases concern municipal liability, capital sentencing, preclusion, declaratory relief, and punishment limits. The 2018 peak therefore separates one group of cases about federal review and constitutional claim thresholds from another group about liability, preclusion, remedies, and punishment doctrine.

This gives Mode 5 a network interpretation. The mode does not detect a single doctrinal field in the way Mode 3 detects Fourth Amendment and police litigation structure. Instead, it shows a changing citation neighborhood around federal constitutional claims against government actors. In 1973, newer equal protection and criminal procedure cases separate from older incorporation, finality, punishment, and confession cases. In 2016, capital punishment cases cluster with municipal liability and criminal review cases, while state law sufficiency and evidentiary review cases sit on the opposite side. By 2018, habeas, substantive due process, qualified immunity, and detention cases are grouped together, while municipal liability, preclusion, declaratory relief, and punishment cases form the opposing neighborhood.

Overall, Mode 5 is best interpreted as a mixed constitutional criminal and remedies mode. The positive side generally emphasizes federal review, constitutional claim thresholds, due process, detention, qualified immunity, capital punishment, and equal protection. The negative side generally emphasizes municipal liability, preclusion, federal court remedies, evidentiary sufficiency, incorpo-

ration, and punishment limits. The main finding is that Mode 5 captures a broader reorganization than Mode 3: it links constitutional claims against government action to the doctrines that determine reviewability, liability, remedies, and punishment.

I.10 Mode-wise change point analysis of the Enron email network

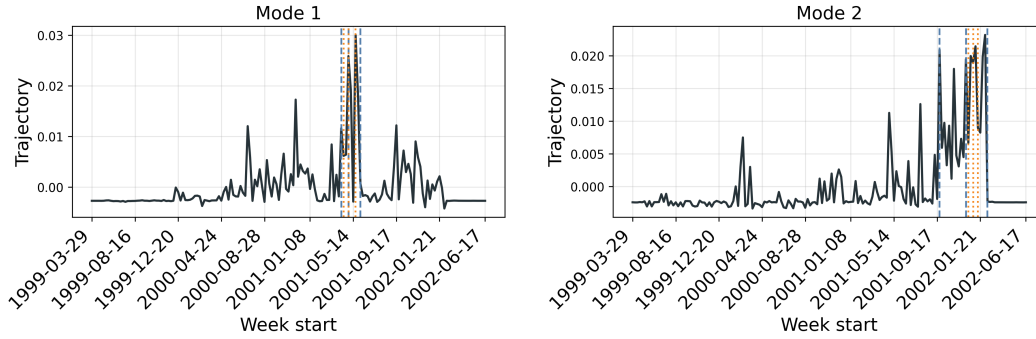


Figure I.21: Trajectories of Enron.

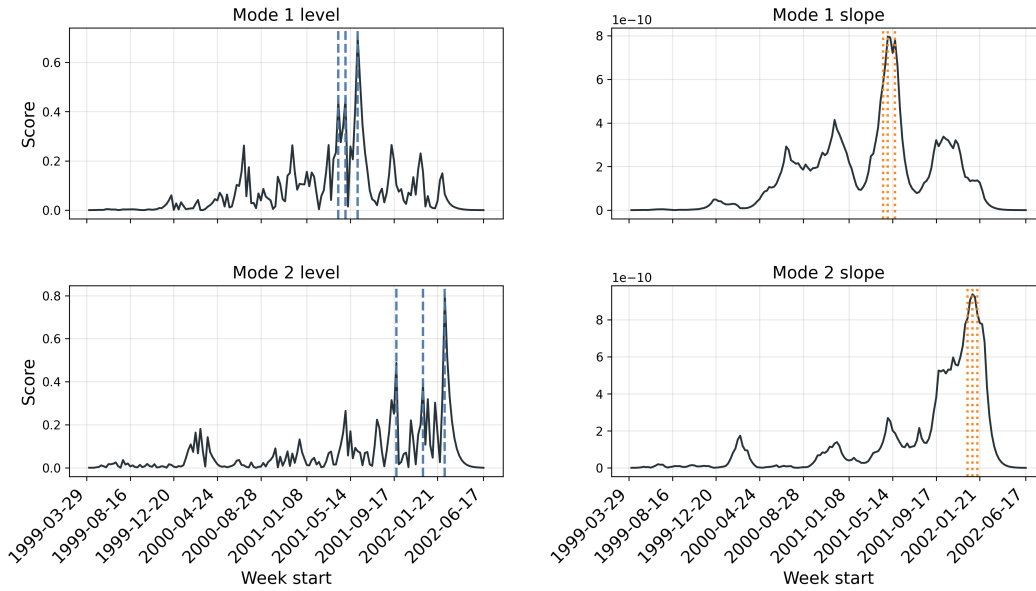


Figure I.22: Mode-wise level (i.e., 0th) and slope (i.e., 1st) order change point scores for the first two Enron e-mail network modes.

We also apply the same mode-wise change point analysis to the Enron email network. The network is constructed from the CMU version of the Enron email corpus [21]. Employee role labels are matched from the auxiliary employee metadata file `E-Mails-updated.csv` in Schulz’s Enron-mails repository [38]. We use these role labels only as auxiliary metadata, and we cite external sources when making more specific claims about individuals’ positions or functions. Because the dataset concerns real individuals, we report individual names only in the attribution tables needed to reproduce the analysis, and interpret the results as descriptive network patterns. Figure I.21 shows the first two estimated mode-wise trajectories, and Figure I.22 reports the corresponding 0th and 1st order change point scores. The interpretation below focuses on 0th order level changes, since Tables I.7 and I.8 report level change attributions.

Mode 1 captures an early shift in communication network structure during spring and early summer 2001. Its three largest level changes occur in the weeks of 2001-04-09, 2001-04-30, and 2001-06-04. These dates fall during Jeffrey Skilling’s short tenure as Enron CEO and precede the firm’s more

visible public collapse period later in 2001 [39, 40]. We therefore interpret Mode 1 as a descriptive signal of early internal communication reorganization, rather than as a direct response to bankruptcy or later public investigations.

The April 30 peak provides the clearest example for Mode 1. On the positive side, the table includes employees with roles listed as Director, CEO, President, Vice President, Manager, Employee, and Managing Director, together with one employee whose role is not listed. On the negative side, the table includes employees with roles listed as President, Manager, Director, CEO, Employee, and Trader, together with several employees whose roles are not listed. Among the names with external support, Lavorato is described in contemporary reporting as running Enron's energy trading business [41], while Arnold is described in later reporting as a former Enron natural gas trader and Shankman as a prominent trader [42]. Kuykendall is listed as a Trader in the role metadata [38]. Thus, we interpret the April 30 peak conservatively as a separation between two sets of highly attributed employee nodes, with some evidence that the negative side contains several trading or commercially connected figures.

The April 9 and June 4 peaks support the same cautious interpretation while also showing that the signs of the learned mode should not be treated as fixed employee labels. Several employees appear on different sides across the three peaks. For example, Arnold appears on the positive side on April 9 but on the negative side on April 30 and June 4; Shankman appears on the positive side on April 9 and June 4 but on the negative side on April 30; and Holst appears on the negative side on April 9 but on the positive side on April 30. We therefore interpret Mode 1 as a spring 2001 rotation in relative communication prominence among overlapping employee groups, rather than as a stable partition of employees. Its main value is that it identifies an internal communication shift that precedes the more visible crisis period events later in 2001.

Mode 2 captures a later crisis period direction. Its largest level change occurs in the week of 2002-02-11, with additional large changes in the weeks of 2001-09-24 and 2001-12-10. These dates align with Enron's public crisis timeline. Skilling resigned in August 2001, Enron's disclosures and investigations intensified in fall 2001, the firm filed for bankruptcy in December 2001, and congressional and regulatory scrutiny continued into early 2002 [40, 43, 44].

The September 24 peak provides the clearest prebankruptcy Mode 2 separation. On the negative side, the table includes employees with roles listed as Director, Vice President, Manager, and Employee. On the positive side, the table includes employees with roles listed as Vice President, Trader, President, and Employee, together with several employees whose roles are not listed. Among the names with external support, Grigsby is described in contemporary reporting as Enron's former Vice President for natural gas trading, and Arnold is described in later reporting as a former Enron natural gas trader [45, 42]. Thus, the September peak appears to separate two highly attributed employee groups, with the negative side containing several employees whose listed roles are senior or managerial and at least two externally supported trading or commercial figures. We interpret this separation descriptively as a communication network pattern, not as evidence of individual responsibility or misconduct.

The December 10 peak occurs immediately after Enron's bankruptcy filing. On the negative side, the table includes employees with roles listed as Manager, Director, Trader, Vice President, and Employee. On the positive side, the table includes employees with roles listed as Vice President, Employee, Manager, and Director, together with several employees whose roles are not listed. Steffes is the largest positive attribution at this peak and is listed as a Vice President in the role metadata [38]. We therefore interpret the December 10 peak as a crisis period shift between two highly attributed groups of employee nodes, rather than assigning a more specific organizational interpretation beyond what the table and cited metadata support.

The dominant Mode 2 event occurs on February 11, 2002. At this point, the positive side contains employees with roles listed as Employee, President, Vice President, CEO, and Manager. The bottom side has much smaller absolute scores and includes roles listed as Employee, President, Director, Trader, and Vice President, together with several employees whose roles are not listed. Because the positive side has substantially larger attribution magnitudes, the February peak is best interpreted as a post collapse concentration of communication change around the positively attributed employee group.

Taken together, the Enron results illustrate the usefulness of mode-wise attribution. The score curves identify when each learned direction changes, while the attribution tables identify which employee nodes define those changes. Mode 1 isolates an earlier spring 2001 communication reallocation during Skilling’s CEO period, whereas Mode 2 isolates a later crisis period reorganization around Enron’s public collapse, bankruptcy, and post collapse investigations. The supported claim is not that the method identifies the cause of Enron’s collapse, that each mode corresponds to a single department, or that highly attributed employees bear responsibility for events at Enron. Rather, the method separates distinct temporal directions of network change and attaches each direction to employee nodes whose listed roles can be checked in the attribution tables and auxiliary metadata.

Table I.7: Mode 1 level change-point attributions for the Enron email network. For each change point, TOP rows report the most positively attributed employee/mailbox nodes and BOTTOM rows report the most negatively attributed nodes. Employee/mailbox labels are the normalized node labels used in the Enron email network. Roles are matched from auxiliary employee metadata when available.

CP rank	Week	Side	Employee/mailbox	Role	Score
1	2001-06-04	Top	zipper-a	Vice President	+0.02285
1	2001-06-04	Top	taylor-m	Employee	+0.01607
1	2001-06-04	Top	donoho-l	Employee	+0.01497
1	2001-06-04	Top	shapiro-r	Vice President	+0.00981
1	2001-06-04	Top	williams-j	Vice President	+0.00924
1	2001-06-04	Top	watson-k		+0.00857
1	2001-06-04	Top	campbell-l	Employee	+0.00774
1	2001-06-04	Top	shankman-j	President	+0.00716
1	2001-06-04	Top	lokay-m	Employee	+0.00706
1	2001-06-04	Top	hayslett-r	Vice President	+0.00582
1	2001-06-04	Bottom	maggi-m	Director	-0.01849
1	2001-06-04	Bottom	tycholiz-b	Vice President	-0.01930
1	2001-06-04	Bottom	presto-k	Vice President	-0.01971
1	2001-06-04	Bottom	arnold-j	Manager	-0.02007
1	2001-06-04	Bottom	whalley-l		-0.02035
1	2001-06-04	Bottom	jones-t		-0.02110
1	2001-06-04	Bottom	quigley-d	Trader	-0.02132
1	2001-06-04	Bottom	lavorato-j	CEO	-0.02835
1	2001-06-04	Bottom	storey-g	Director	-0.03984
1	2001-06-04	Bottom	lenhart-m	Employee	-0.04147
2	2001-04-30	Top	holst-k	Director	+0.04364
2	2001-04-30	Top	sanchez-m		+0.03514
2	2001-04-30	Top	skilling-j	CEO	+0.02747
2	2001-04-30	Top	whalley-g	President	+0.02298
2	2001-04-30	Top	corman-s	Vice President	+0.02290
2	2001-04-30	Top	buy-r	Manager	+0.02138
2	2001-04-30	Top	grigsby-m	Manager	+0.02118
2	2001-04-30	Top	tycholiz-b	Vice President	+0.02000
2	2001-04-30	Top	beck-s	Employee	+0.01778
2	2001-04-30	Top	haedicke-m	Managing Director	+0.01702
2	2001-04-30	Bottom	scott-s		-0.02503
2	2001-04-30	Bottom	shankman-j	President	-0.02759
2	2001-04-30	Bottom	arnold-j	Manager	-0.03399
2	2001-04-30	Bottom	motley-m	Director	-0.03675
2	2001-04-30	Bottom	badeer-r	Director	-0.03991
2	2001-04-30	Bottom	lavorato-j	CEO	-0.04071
2	2001-04-30	Bottom	south-s		-0.04296
2	2001-04-30	Bottom	gay-r	Employee	-0.04679
2	2001-04-30	Bottom	lenhart-m	Employee	-0.05000
2	2001-04-30	Bottom	kuykendall-t	Trader	-0.05205

Continued on next page

CP rank	Week	Side	Employee/mailbox	Role	Score
3	2001-04-09	Top	taylor-m	Employee	+0.04103
3	2001-04-09	Top	shankman-j	President	+0.04080
3	2001-04-09	Top	mccarty-d	Vice President	+0.04004
3	2001-04-09	Top	shively-h	Vice President	+0.02783
3	2001-04-09	Top	shapiro-r	Vice President	+0.02733
3	2001-04-09	Top	haedicke-m	Managing Director	+0.02675
3	2001-04-09	Top	arnold-j	Manager	+0.02365
3	2001-04-09	Top	donoho-l	Employee	+0.02183
3	2001-04-09	Top	fossum-d	Vice President	+0.02183
3	2001-04-09	Top	lokay-m	Employee	+0.02135
3	2001-04-09	Bottom	mclaughlin-e	Employee	-0.01292
3	2001-04-09	Bottom	tholt-j	Vice President	-0.01292
3	2001-04-09	Bottom	wolfe-j		-0.01437
3	2001-04-09	Bottom	dasovich-j	Employee	-0.01590
3	2001-04-09	Bottom	reitmeyer-j	Employee	-0.01590
3	2001-04-09	Bottom	allen-p	Manager	-0.01634
3	2001-04-09	Bottom	staab-t	Employee	-0.01984
3	2001-04-09	Bottom	kitchen-l	President	-0.02156
3	2001-04-09	Bottom	lavorato-j	CEO	-0.02243
3	2001-04-09	Bottom	holst-k	Director	-0.04147

Table I.8: Mode 2 level change-point attributions for the Enron email network. For each change point, TOP rows report the most positively attributed employee/mailbox nodes and BOTTOM rows report the most negatively attributed nodes. Employee/mailbox labels are the normalized node labels used in the Enron email network. Roles are matched from auxiliary employee metadata when available.

CP rank	Week	Side	Employee/mailbox	Role	Score
1	2002-02-11	Top	sager-e	Employee	+0.06423
1	2002-02-11	Top	gilbertsmith-d	Employee	+0.06109
1	2002-02-11	Top	whalley-g	President	+0.06085
1	2002-02-11	Top	presto-k	Vice President	+0.05944
1	2002-02-11	Top	davis-d	Vice President	+0.05907
1	2002-02-11	Top	steffes-j	Vice President	+0.05835
1	2002-02-11	Top	zufferli-j	Vice President	+0.05771
1	2002-02-11	Top	lavorato-j	CEO	+0.05514
1	2002-02-11	Top	grigsby-m	Manager	+0.05480
1	2002-02-11	Top	tycholiz-b	Vice President	+0.05480
1	2002-02-11	Bottom	dickson-s	Employee	+0.00000
1	2002-02-11	Bottom	williams-w3		-0.00010
1	2002-02-11	Bottom	semperger-c	Employee	-0.00058
1	2002-02-11	Bottom	watson-k		-0.00131
1	2002-02-11	Bottom	horton-s	President	-0.00178
1	2002-02-11	Bottom	hyatt-k	Director	-0.00567
1	2002-02-11	Bottom	lokay-m	Employee	-0.00599
1	2002-02-11	Bottom	keiser-k	Employee	-0.01048
1	2002-02-11	Bottom	ybarbo-p	Trader	-0.02262
1	2002-02-11	Bottom	corman-s	Vice President	-0.02479
2	2001-09-24	Top	harris-s	Vice President	+0.01623
2	2001-09-24	Top	hayslett-r	Vice President	+0.01269
2	2001-09-24	Top	ybarbo-p	Trader	+0.01096
2	2001-09-24	Top	lokay-m	Employee	+0.00905
2	2001-09-24	Top	kitchen-l	President	+0.00886
2	2001-09-24	Top	ring-a		+0.00771

Continued on next page

CP rank	Week	Side	Employee/mailbox	Role	Score
2	2001-09-24	Top	mclaughlin-e	Employee	+0.00727
2	2001-09-24	Top	dasovich-j	Employee	+0.00451
2	2001-09-24	Top	fossum-d	Vice President	+0.00412
2	2001-09-24	Top	gang-l		+0.00321
2	2001-09-24	Bottom	maggi-m	Director	-0.05631
2	2001-09-24	Bottom	zipper-a	Vice President	-0.05795
2	2001-09-24	Bottom	tycholz-b	Vice President	-0.06100
2	2001-09-24	Bottom	arnold-j	Manager	-0.07963
2	2001-09-24	Bottom	davis-d	Vice President	-0.08071
2	2001-09-24	Bottom	gilbertsmith-d	Employee	-0.08082
2	2001-09-24	Bottom	neal-s	Vice President	-0.08083
2	2001-09-24	Bottom	presto-k	Vice President	-0.08090
2	2001-09-24	Bottom	grigsby-m	Manager	-0.09069
2	2001-09-24	Bottom	martin-t	Vice President	-0.09145
3	2001-12-10	Top	steffes-j	Vice President	+0.05076
3	2001-12-10	Top	rapp-b		+0.01941
3	2001-12-10	Top	geaccone-t	Employee	+0.00931
3	2001-12-10	Top	schoolcraft-d		+0.00599
3	2001-12-10	Top	griffith-j	Manager	+0.00562
3	2001-12-10	Top	maggi-m	Director	+0.00528
3	2001-12-10	Top	mckay-j	Director	+0.00285
3	2001-12-10	Top	bailey-s		+0.00264
3	2001-12-10	Top	lucci-p	Employee	+0.00142
3	2001-12-10	Top	forney-j	Manager	+0.00142
3	2001-12-10	Bottom	arnold-j	Manager	-0.04975
3	2001-12-10	Bottom	badeer-r	Director	-0.04984
3	2001-12-10	Bottom	motley-m	Director	-0.05034
3	2001-12-10	Bottom	swerzbin-m	Trader	-0.05034
3	2001-12-10	Bottom	davis-d	Vice President	-0.05034
3	2001-12-10	Bottom	buy-r	Manager	-0.05034
3	2001-12-10	Bottom	storey-g	Director	-0.05077
3	2001-12-10	Bottom	arora-h	Vice President	-0.05082
3	2001-12-10	Bottom	zufferli-j	Vice President	-0.05173
3	2001-12-10	Bottom	gilbertsmith-d	Employee	-0.05284

J Proofs

J.1 Overview of proof strategy

The purpose of this section is to connect the dynamic random dot product graph model

$$\mathbf{P}(t) = \mathbf{X}\mathbf{Y}(t)^\top$$

to the distance-based constructions developed in this paper.

The first goal is to show that the modified unfolded adjacency spectral embedding (UASE) recovers the time-varying latent positions $\mathbf{Y}(t)$ *uniformly over time*, up to a single orthogonal transformation. The second goal is to propagate this embedding error into uniform control of time pair dissimilarities and, ultimately, to consistency of the CMDS trajectory embedding of time.

Step 1: Population identification (what unfolding targets). We study the rank d singular value decomposition of the unfolded *population* matrix $\mathbf{P} = [\mathbf{P}(1) \mid \cdots \mid \mathbf{P}(T)]$. This analysis shows that the block of right singular vectors $\tilde{\mathbf{V}}(t)$ encodes $\mathbf{Y}(t)$ in a shared coordinate system, up to a time independent linear map. Assumption 3.2 fixes the population second-moment structure and thereby restores the identifiability from general linear transformations upto a single orthogonal factor. Concretely, we obtain an alignment of the form $\tilde{\mathbf{V}}(t)\tilde{\Sigma} \approx n^{1/2}\mathbf{Y}(t)\mathbf{W}_1$ with $\mathbf{W}_1 \in \mathbb{O}(d)$, uniformly in t .

Step 2: Empirical perturbation (how replacing \mathbf{P} by \mathbf{A} affects the embedding). We then compare the empirical unfolded adjacency matrix \mathbf{A} to its expectation \mathbf{P} . Using multilayer spectral perturbation bounds, we control the deviation between the empirical singular factors $(\mathbf{V}(t), \mathbf{\Sigma})$ and their population counterparts $(\tilde{\mathbf{V}}(t), \tilde{\mathbf{\Sigma}})$. This yields an orthogonal matrix $\mathbf{W}_2 \in \mathbb{O}(d)$ such that $\mathbf{V}(t)\mathbf{\Sigma} \approx \tilde{\mathbf{V}}(t)\tilde{\mathbf{\Sigma}}\mathbf{W}_2$ uniformly in t .

Combining the steps. Composing the two alignments with $\mathbf{W} = \mathbf{W}_1\mathbf{W}_2 \in \mathbb{O}(d)$ and applying the triangle inequality gives uniform operator norm consistency of the modified UASE embeddings:

$$\sup_{t \in \mathcal{T}} \|\hat{\mathbf{Y}}_{\text{mod}}(t) - \mathbf{Y}(t)\mathbf{W}\|_2 = \mathcal{O}(\log n) \quad \text{a.s.}$$

This is formalized in Theorem 3.3, which adapts the multilayer UASE analysis of Jones and Rubin-Delanchy [3] to the present isotropic setting.

Downstream implication for the paper. Once $\hat{\mathbf{Y}}_{\text{mod}}(t)$ is uniformly close to $\mathbf{Y}(t)\mathbf{W}$, orthogonal invariance ensures that the second-moment and distance quantities built from the embeddings are not subject to multiplicative geometric distortion. The remainder of the section converts the embedding bound into uniform control of squared dissimilarities, and then propagates this error through CMDS perturbation arguments to obtain consistency of the trajectory embedding of time.

J.2 Consistency of modified UASE

We now establish consistency of the modified unfolded adjacency spectral embedding. As discussed in the overview, the proof separates naturally into two components: a population identification step, which characterizes what the unfolded embedding recovers in the absence of noise, and an empirical perturbation step, which controls the deviation introduced by replacing the population matrix with its observed counterpart.

To prove Theorem 3.3, we rely on two intermediate results. The first result identifies the population right singular vectors of the unfolded probability matrix \mathbf{P} with the latent positions $\mathbf{Y}(t)$, up to an orthogonal transformation that is common across time. The second result shows that the corresponding empirical singular vectors concentrate around their population analogues at a controlled rate. Together, these results imply uniform consistency of the modified UASE embeddings over time.

Lemma J.1. *There exists a (possibly random) orthogonal matrix $\mathbf{W} \in \mathbb{O}(d)$ such that, for all $t \in \mathcal{T}$*

$$\left\| \tilde{\mathbf{V}}(t)\tilde{\mathbf{\Sigma}} - n^{1/2}\mathbf{Y}(t)\mathbf{W} \right\|_2 = \mathcal{O}\left(n^{1/2} \log n\right) \quad \text{a.s.}$$

Proof. This lemma establishes a population level alignment between the right singular vectors of the unfolded probability matrix and the latent positions. The argument begins by controlling finite sample second-moments of the latent positions. Concentration of $\mathbf{X}^\top \mathbf{X}$ and $\mathbf{Y}(t)^\top \mathbf{Y}(t)$ around their expectations ensures that both matrices are well conditioned and of full rank, which is required to invoke singular value decompositions at the population level.

First, by Hoeffding's inequality, we have

$$\begin{aligned} \left\| \mathbf{X}^\top \mathbf{X} - n\mathbb{E}[\chi\chi^\top] \right\|_2 &= \mathcal{O}(n^{1/2} \log n) \quad \text{a.s.} \\ \left\| \mathbf{Y}(t)^\top \mathbf{Y}(t) - n\mathbb{E}[\phi(t)\phi(t)^\top] \right\|_2 &= \mathcal{O}(n^{1/2} \log n) \quad \text{a.s.} \end{aligned}$$

Since $\mathbb{E}[\chi\chi^\top]$ and $\mathbb{E}[\phi(t)\phi(t)^\top]$ are invertible, \mathbf{X} and $\mathbf{Y}(t)$ are of rank d almost surely.

Assumption 3.2 fixes the scale and orientation of the population inner product structure. As a consequence, $(\mathbf{X}^\top \mathbf{X})^{1/2}$ concentrates around $n^{1/2}\mathbf{I}_d$, restoring identifiability from general linear transformations upto orthogonal ones. Formally,

$$\begin{aligned}
\left\| (\mathbf{X}^\top \mathbf{X})^{1/2} - n^{1/2} \mathbf{I}_d \right\|_2 &= \max_{k=1, \dots, d} \left| \lambda_k (\mathbf{X}^\top \mathbf{X})^{1/2} - n^{1/2} \right| \\
&\leq \max_{k=1, \dots, d} \frac{|\lambda_k (\mathbf{X}^\top \mathbf{X}) - n|}{\lambda_k (\mathbf{X}^\top \mathbf{X})^{1/2} + n^{1/2}} \\
&\leq \frac{1}{n^{1/2}} \left\| \mathbf{X}^\top \mathbf{X} - n \mathbf{I}_d \right\|_2 \\
&= \mathcal{O}(\log n) \quad \text{a.s.}
\end{aligned}$$

Similarly, we can bound $\|\mathbf{Y}(t)\|_2$ as

$$\begin{aligned}
\|\mathbf{Y}(t)\|_2 &\leq \left\| \mathbf{Y}(t)^\top \mathbf{Y}(t) \right\|_2^{1/2} \\
&\leq \left(\left\| \mathbf{Y}(t)^\top \mathbf{Y}(t) - n \mathbb{E} [\phi(t) \phi(t)^\top] \right\|_2 + n \left\| \mathbb{E} [\phi(t) \phi(t)^\top] \right\|_2 \right)^{1/2} \\
&= \mathcal{O}(n^{1/2}) \quad \text{a.s.}
\end{aligned}$$

Following the argument in Proposition 16 of Jones and Rubin-Delanchy [3], since \mathbf{X} and $\mathbf{Y}(t)$ are of rank d , there exists (possibly random) orthogonal matrices $\mathbf{Q}, \mathbf{Q}(t) \in \mathbb{O}(d)$ such that

$$\begin{aligned}
\tilde{\mathbf{U}} \tilde{\Sigma} &= \mathbf{X} \left(\sum_{t \in \mathcal{T}} \mathbf{Y}(t)^\top \mathbf{Y}(t) \right)^{1/2} \mathbf{Q}, \\
\tilde{\mathbf{V}}(t) \tilde{\Sigma} &= \mathbf{Y}(t) (\mathbf{X}^\top \mathbf{X})^{1/2} \mathbf{Q}(t),
\end{aligned}$$

almost surely. From the singular value decomposition $\mathbf{X} \mathbf{Y}(t)^\top = \tilde{\mathbf{U}} \tilde{\Sigma} \tilde{\mathbf{V}}(t)^\top$, we obtain

$$\mathbf{X} \left(\sum_{t \in \mathcal{T}} \mathbf{Y}(t)^\top \mathbf{Y}(t) \right)^{1/2} \mathbf{Q} \tilde{\Sigma}^{-1} \mathbf{Q}(t)^\top (\mathbf{X}^\top \mathbf{X})^{1/2} \mathbf{Y}(t)^\top = \mathbf{X} \mathbf{Y}(t)^\top.$$

Since \mathbf{X} and $\mathbf{Y}(t)$ are of rank d , this implies

$$\begin{aligned}
&\left(\sum_{t \in \mathcal{T}} \mathbf{Y}(t)^\top \mathbf{Y}(t) \right)^{1/2} \mathbf{Q} \tilde{\Sigma}^{-1} \mathbf{Q}(t)^\top (\mathbf{X}^\top \mathbf{X})^{1/2} = \mathbf{I}_d \\
&\Leftrightarrow (\mathbf{X}^\top \mathbf{X})^{1/2} \mathbf{Q}(t) = \left(\sum_{t \in \mathcal{T}} \mathbf{Y}(t)^\top \mathbf{Y}(t) \right)^{-1/2} \mathbf{Q} \tilde{\Sigma}
\end{aligned}$$

Therefore, $(\mathbf{X}^\top \mathbf{X})^{1/2} \mathbf{Q}(t)$ does not depend on t . Hence, there exists a (possibly random) orthogonal matrix $\mathbf{W} \in \mathbb{O}(d)$ such that

$$\tilde{\mathbf{V}}(t) \tilde{\Sigma} = \mathbf{Y}(t) (\mathbf{X}^\top \mathbf{X})^{1/2} \mathbf{W}$$

almost surely.

Finally, using submultiplicativity of the spectral norm and $\mathbf{W} \in \mathbb{O}(d)$, we have

$$\begin{aligned}
\left\| \tilde{\mathbf{V}}(t) \tilde{\Sigma} - n^{1/2} \mathbf{Y}(t) \mathbf{W} \right\|_2 &= \left\| \mathbf{Y}(t) (\mathbf{X}^\top \mathbf{X})^{1/2} \mathbf{W} - n^{1/2} \mathbf{Y}(t) \mathbf{W} \right\|_2 \\
&\leq \|\mathbf{Y}(t)\|_2 \left\| (\mathbf{X}^\top \mathbf{X})^{1/2} - n^{1/2} \mathbf{I}_d \right\|_2 \\
&= \mathcal{O}(n^{1/2} \log n) \quad \text{a.s.}
\end{aligned}$$

This completes the proof. \square

Lemma J.2. *There exists a (possibly random) orthogonal matrix $\mathbf{W} \in \mathbb{O}(d)$ such that, for all $t \in \mathcal{T}$,*

$$\left\| \mathbf{V}(t) \Sigma - \tilde{\mathbf{V}}(t) \tilde{\Sigma} \mathbf{W} \right\|_2 = \mathcal{O}(n^{1/2} (\log n)^{1/2}) \quad \text{a.s.}$$

Proof. By Theorem 2 and Proposition 15 of Jones and Rubin-Delanchy [3], there exists a (possibly random) orthogonal matrix $\mathbf{W} \in \mathbb{O}(d)$ such that

$$\begin{aligned} \left\| \mathbf{V}(t)\boldsymbol{\Sigma}^{1/2} - \tilde{\mathbf{V}}(t)\tilde{\boldsymbol{\Sigma}}^{1/2}\mathbf{W} \right\|_{2 \rightarrow \infty} &= \mathcal{O}\left(n^{-1/2}(\log n)^{1/2}\right) \quad \text{a.s.}, \\ \left\| \mathbf{W}\boldsymbol{\Sigma}^{1/2} - \tilde{\boldsymbol{\Sigma}}^{1/2}\mathbf{W} \right\|_F &= \mathcal{O}\left(n^{-1/2} \log n\right) \quad \text{a.s.}, \end{aligned}$$

where the two-to-infinity norm defined of a matrix $\mathbf{X} \in \mathbb{R}^{n \times d}$ is defined as $\|\mathbf{X}\|_{2 \rightarrow \infty} = \max_{i=1, \dots, n} \|\mathbf{X}_i\|$.

Moreover, by Propositions 7 and 10 of Jones and Rubin-Delanchy [3],

$$\|\boldsymbol{\Sigma}\|_2 = \mathcal{O}(n), \quad \|\tilde{\boldsymbol{\Sigma}}\|_2 = \mathcal{O}(n) \quad \text{a.s.}$$

To bound the spectral norm difference, we use the triangle inequality and submultiplicativity of the spectral norm,

$$\begin{aligned} &\left\| \mathbf{V}(t)\boldsymbol{\Sigma} - \tilde{\mathbf{V}}(t)\tilde{\boldsymbol{\Sigma}}\mathbf{W} \right\|_2 \\ &\leq \left\| \mathbf{V}(t)\boldsymbol{\Sigma}^{1/2} - \tilde{\mathbf{V}}(t)\tilde{\boldsymbol{\Sigma}}^{1/2}\mathbf{W} \right\|_2 \|\boldsymbol{\Sigma}\|_2^{1/2} + \left\| \tilde{\mathbf{V}}(t) \right\|_2 \|\tilde{\boldsymbol{\Sigma}}\|_2^{1/2} \left\| \mathbf{W}\boldsymbol{\Sigma}^{1/2} - \tilde{\boldsymbol{\Sigma}}^{1/2}\mathbf{W} \right\|_2 \\ &\leq \sqrt{n} \left\| \mathbf{V}(t)\boldsymbol{\Sigma}^{1/2} - \tilde{\mathbf{V}}(t)\tilde{\boldsymbol{\Sigma}}^{1/2}\mathbf{W} \right\|_{2 \rightarrow \infty} \|\boldsymbol{\Sigma}\|_2^{1/2} + \left\| \tilde{\mathbf{V}}(t) \right\|_2 \|\tilde{\boldsymbol{\Sigma}}\|_2^{1/2} \left\| \mathbf{W}\boldsymbol{\Sigma}^{1/2} - \tilde{\boldsymbol{\Sigma}}^{1/2}\mathbf{W} \right\|_F \end{aligned}$$

Since $\tilde{\mathbf{V}}(t)$ consists of rows of a column orthonormal matrix, its spectral norm is bounded by 1. Combining these facts, we conclude that

$$\left\| \mathbf{V}(t)\boldsymbol{\Sigma} - \tilde{\mathbf{V}}(t)\tilde{\boldsymbol{\Sigma}}\mathbf{W} \right\|_2 = \mathcal{O}\left(n^{1/2}(\log n)^{1/2}\right) \quad \text{a.s.}$$

□

We now combine these two arguments.

Proof of Theorem 3.3. The first lemma identifies the population right singular vectors with the latent positions $\mathbf{Y}(t)$ up to an orthogonal transformation. The second lemma controls the deviation between the estimated embedding and its population counterpart. Combining these two steps yields uniform consistency of the modified UASE embeddings across time.

By the preceding lemmas, there exist (possibly random) orthogonal matrices $\mathbf{W}_1, \mathbf{W}_2 \in \mathbb{O}(d)$ such that

$$\begin{aligned} \left\| \tilde{\mathbf{V}}(t)\tilde{\boldsymbol{\Sigma}} - n^{1/2}\mathbf{Y}(t)\mathbf{W}_1 \right\|_2 &= \mathcal{O}\left(n^{1/2} \log n\right) \quad \text{a.s.}, \\ \left\| \mathbf{V}(t)\boldsymbol{\Sigma} - \tilde{\mathbf{V}}(t)\tilde{\boldsymbol{\Sigma}}\mathbf{W}_2 \right\|_2 &= \mathcal{O}\left(n^{1/2}(\log n)^{1/2}\right) \quad \text{a.s.} \end{aligned}$$

Let $\mathbf{W} = \mathbf{W}_1\mathbf{W}_2$, which is again an orthogonal matrix. Then, by the triangle inequality,

$$\begin{aligned} \left\| \hat{\mathbf{Y}}_{\text{mod}}(t) - \mathbf{Y}(t)\mathbf{W} \right\|_2 &= \frac{1}{n^{1/2}} \left\| \mathbf{V}(t)\boldsymbol{\Sigma} - n^{1/2}\mathbf{Y}(t)\mathbf{W} \right\|_2 \\ &\leq \frac{1}{n^{1/2}} \left(\left\| \tilde{\mathbf{V}}(t)\tilde{\boldsymbol{\Sigma}} - n^{1/2}\mathbf{Y}(t)\mathbf{W}_1 \right\|_2 + \left\| \mathbf{V}(t)\boldsymbol{\Sigma} - \tilde{\mathbf{V}}(t)\tilde{\boldsymbol{\Sigma}}\mathbf{W}_2 \right\|_2 \right). \end{aligned}$$

Substituting the established bounds and taking the union over $t \in \mathcal{T}$ yields

$$\sup_{t \in \mathcal{T}} \left\| \hat{\mathbf{Y}}_{\text{mod}}(t) - \mathbf{Y}(t)\mathbf{W} \right\|_2 = \mathcal{O}(\log n) \quad \text{a.s.}$$

□

J.3 From embedding error to dissimilarity control

We next show how embedding level consistency translates into uniform control of pairwise dissimilarities and matrix level dissimilarity errors. Proposition E.3 combines the two stages at the dissimilarity level by showing that squared dissimilarities computed from estimated embeddings uniformly approximate population squared dissimilarities up to a controlled error, leading to a Frobenius norm control of the entire squared dissimilarity matrix, which is the natural input to CMDS.

Proof of Proposition E.3. The argument is a direct application of the triangle inequality, combining population approximation error with embedding error.

Now, observe that

$$\begin{aligned} & \sup_{t,s \in \mathcal{T}} \left| \hat{d}(\hat{\mathbf{Y}}(t), \hat{\mathbf{Y}}(s))^2 - d(\phi(t), \phi(s))^2 \right| \\ & \leq \sup_{t,s \in \mathcal{T}} \left(\left| \hat{d}(\hat{\mathbf{Y}}(t), \hat{\mathbf{Y}}(s))^2 - \hat{d}(\mathbf{Y}(t), \mathbf{Y}(s))^2 \right| + \left| \hat{d}(\mathbf{Y}(t), \mathbf{Y}(s))^2 - d(\phi(t), \phi(s))^2 \right| \right) \\ & \leq \sup_{t,s \in \mathcal{T}} \left| \hat{d}(\hat{\mathbf{Y}}(t), \hat{\mathbf{Y}}(s))^2 - \hat{d}(\mathbf{Y}(t), \mathbf{Y}(s))^2 \right| + \sup_{t,s \in \mathcal{T}} \left| \hat{d}(\mathbf{Y}(t), \mathbf{Y}(s))^2 - d(\phi(t), \phi(s))^2 \right|. \end{aligned}$$

By Assumptions E.1 and E.2,

$$\begin{aligned} \sup_{t,s \in \mathcal{T}} \left| \hat{d}(\mathbf{Y}(t), \mathbf{Y}(s))^2 - d(\phi(t), \phi(s))^2 \right| &= \mathcal{O}(f(n)) \quad \text{a.s.} \\ \sup_{t,s \in \mathcal{T}} \left| \hat{d}(\hat{\mathbf{Y}}(t), \hat{\mathbf{Y}}(s))^2 - \hat{d}(\mathbf{Y}(t), \mathbf{Y}(s))^2 \right| &= \mathcal{O}(g(n)) \quad \text{a.s.} \end{aligned}$$

Therefore, we have

$$\sup_{t,s \in \mathcal{T}} \left| \hat{d}(\hat{\mathbf{Y}}(t), \hat{\mathbf{Y}}(s))^2 - d(\phi(t), \phi(s))^2 \right| = \mathcal{O}(f(n) + g(n)) \quad \text{a.s.}$$

Since T is fixed, a uniform entrywise bound implies the same order in Frobenius norm. \square

J.4 CMDS perturbation and node-level to trajectory-level control

We propagate the dissimilarity control obtained above through CMDS using standard CMDS perturbation arguments. CMDS can be viewed as a spectral procedure applied to the centered Gram matrix associated with the squared dissimilarity matrix; therefore, a perturbation bound for the squared dissimilarity matrix translates into a perturbation bound for the CMDS output coordinates.

Proof of Proposition E.4. Let $\nu := \|\mathbf{D}_\phi^{(2)} - \hat{\mathbf{D}}_{\hat{\mathbf{Y}}}^{(2)}\|_F$. Then

$$\|\mathbf{E}_\phi - \hat{\mathbf{E}}_{\hat{\mathbf{Y}}}\|_F \leq \frac{\nu}{2}.$$

Since \mathbf{E}_ϕ and $\hat{\mathbf{E}}_{\hat{\mathbf{Y}}}$ are symmetric, let $\mathbf{U}, \hat{\mathbf{U}}$ denote the matrices whose columns are the eigenvectors corresponding to the a -th through b -th largest eigenvalues, and let $\mathbf{S}, \hat{\mathbf{S}}$ denote the corresponding diagonal matrices of eigenvalues. Then

$$\left(\sum_{t=1}^T \|\hat{\psi}(t; a, b) - \mathbf{R}\psi(t; a, b)\|^2 \right)^{1/2} = \|\hat{\mathbf{U}}\hat{\mathbf{S}}^{1/2} - \mathbf{U}\mathbf{S}^{1/2}\mathbf{R}\|_F.$$

We first control the deviation between the eigenspaces. By the Davis–Kahan theorem [46],

$$\|\sin \Theta(\mathbf{U}, \hat{\mathbf{U}})\|_F \leq \frac{2\|\mathbf{E}_\phi - \hat{\mathbf{E}}_{\hat{\mathbf{Y}}}\|_F}{\text{gap}(a, b)} \leq \frac{\nu}{\text{gap}(a, b)}.$$

To align the two eigenspaces, consider the singular value decomposition

$$\mathbf{U}^\top \hat{\mathbf{U}} = \mathbf{W}_1 \boldsymbol{\Sigma} \mathbf{W}_2^\top,$$

and define $\mathbf{R} := \mathbf{W}_1 \mathbf{W}_2^\top \in \mathbb{O}(b-a+1)$. Writing σ_i for the singular values and $\theta_i := \cos^{-1}(\sigma_i)$ for the principal angles, we obtain

$$\begin{aligned} \|\mathbf{U}^\top \hat{\mathbf{U}} - \mathbf{R}\|_F &= \|\boldsymbol{\Sigma} - \mathbf{I}_{b-a+1}\|_F = \left(\sum_{i=1}^{b-a+1} (1 - \cos \theta_i)^2 \right)^{1/2} \\ &\leq \sum_{i=1}^{b-a+1} (1 - \cos \theta_i) \leq \sum_{i=1}^{b-a+1} (1 - \cos^2 \theta_i) \\ &= \sum_{i=1}^{b-a+1} \sin^2 \theta_i = \|\sin \Theta(\mathbf{U}, \hat{\mathbf{U}})\|_F^2 \\ &\leq \frac{\nu^2}{\text{gap}(a, b)^2}. \end{aligned}$$

Moreover, since the nonzero eigenvalues of $\mathbf{U}\mathbf{U}^\top - \hat{\mathbf{U}}\hat{\mathbf{U}}^\top$ are $\pm \sin \theta_i$, we have

$$\|\mathbf{U}\mathbf{U}^\top - \hat{\mathbf{U}}\hat{\mathbf{U}}^\top\|_F = \left(2 \sum \sin^2 \theta_i \right)^{1/2} = 2^{1/2} \|\sin \Theta(\mathbf{U}, \hat{\mathbf{U}})\|_F \leq \frac{2^{1/2} \nu}{\text{gap}(a, b)}.$$

Next, we control the perturbation of the eigenvalues. By Weyl's inequality,

$$\begin{aligned} \|\hat{\mathbf{S}}\|_2 &\leq \|\mathbf{S}\|_2 + \|\mathbf{E}_\phi - \hat{\mathbf{E}}_{\hat{\mathbf{Y}}}\|_2 \leq \lambda_a + \frac{\nu}{2}, \\ \|\hat{\mathbf{S}}\|_2^{1/2} &\leq \|\mathbf{S}\|_2^{1/2} + \frac{|\|\hat{\mathbf{S}}\|_2 - \|\mathbf{S}\|_2|}{2\|\mathbf{S}\|_2^{1/2}} \leq \lambda_a^{1/2} + \frac{\nu}{4\lambda_a^{1/2}}. \end{aligned}$$

Using the triangle inequality,

$$\begin{aligned} \|\mathbf{R}\hat{\mathbf{S}} - \mathbf{S}\mathbf{R}\|_F &\leq \|(\mathbf{R} - \mathbf{U}^\top \hat{\mathbf{U}})\hat{\mathbf{S}}\|_F + \|\mathbf{U}^\top (\hat{\mathbf{E}}_{\hat{\mathbf{Y}}} - \mathbf{E}_\phi)\hat{\mathbf{U}}\|_F + \|\mathbf{S}(\mathbf{U}^\top \hat{\mathbf{U}} - \mathbf{R})\|_F \\ &\leq \|\mathbf{U}^\top \hat{\mathbf{U}} - \mathbf{R}\|_F (\|\hat{\mathbf{S}}\|_2 + \|\mathbf{S}\|_2) + \|\mathbf{E}_\phi - \hat{\mathbf{E}}_{\hat{\mathbf{Y}}}\|_F \\ &\leq \frac{\nu^2}{\text{gap}(a, b)^2} (2\lambda_a + \frac{\nu}{2}) + \frac{\nu}{2} \\ &= \frac{\nu}{2} + O(\nu^2) \quad (\nu \rightarrow 0). \end{aligned}$$

To pass to square roots, we use an entrywise argument, which yields

$$\begin{aligned} \|\mathbf{R}\hat{\mathbf{S}}^{1/2} - \mathbf{S}^{1/2}\mathbf{R}\|_F &\leq \frac{\|\mathbf{R}\hat{\mathbf{S}} - \mathbf{S}\mathbf{R}\|_F}{\lambda_b^{1/2}} \\ &= \frac{\nu}{2\lambda_b^{1/2}} + O(\nu^2) \quad (\nu \rightarrow 0). \end{aligned}$$

Decomposing the main term and applying the previously established bounds, we obtain

$$\begin{aligned} \|\hat{\mathbf{U}}\hat{\mathbf{S}}^{1/2} - \mathbf{U}\mathbf{S}^{1/2}\mathbf{R}\|_F &\leq \|(\hat{\mathbf{U}}\hat{\mathbf{U}}^\top - \mathbf{U}\mathbf{U}^\top)\hat{\mathbf{U}}\hat{\mathbf{S}}^{1/2}\|_F + \|\mathbf{U}(\mathbf{U}^\top \hat{\mathbf{U}} - \mathbf{R})\hat{\mathbf{S}}^{1/2}\|_F + \|\mathbf{U}(\mathbf{R}\hat{\mathbf{S}}^{1/2} - \mathbf{S}^{1/2}\mathbf{R})\|_F \\ &\leq (\|\hat{\mathbf{U}}\hat{\mathbf{U}}^\top - \mathbf{U}\mathbf{U}^\top\|_F + \|\mathbf{U}^\top \hat{\mathbf{U}} - \mathbf{R}\|_F) \|\hat{\mathbf{S}}\|_2^{1/2} + \|\mathbf{R}\hat{\mathbf{S}}^{1/2} - \mathbf{S}^{1/2}\mathbf{R}\|_F \\ &= \frac{2^{1/2} \nu}{\text{gap}(a, b)} \cdot \lambda_a^{1/2} + \frac{\nu}{2\lambda_b^{1/2}} + O(\nu^2) \quad (\nu \rightarrow 0). \end{aligned}$$

The leading terms can be bounded as

$$\frac{2^{1/2}\nu}{\text{gap}(a, b)} \cdot \lambda_a^{1/2} + \frac{\nu}{2\lambda_b^{1/2}} \leq \left(\frac{2^{1/2}\lambda_a^{1/2}}{\text{gap}(a, b)} + \frac{\lambda_a^{1/2}}{2\lambda_b} \right) \nu \leq \frac{2\lambda_a^{1/2}}{\min(\text{gap}(a, b), \lambda_b)} \nu = \frac{2\kappa(a, b)}{\lambda_a^{1/2}} \nu$$

Combining these bounds yields the desired result. \square

Combining Proposition E.3 and Proposition E.4 immediately yeilds Theorem E.5.

J.5 Verification for MV/TV/mode-wise variation distances

We now verify that the abstract assumptions used in Theorem E.5 hold for the MV, TV, and mode-wise variation distances. Before proving that Assumption E.1 holds for the MV, TV, and mode-wise variation distances, we first establish the consistency of the second-moment matrices.

Lemma J.3. *The following statements hold:*

1. For all $t, s \in \mathcal{T}$, $\|\mathbf{M}(\phi(t), \phi(s))\|_2$ is finite.

2.

$$\sup_{t, s \in \mathcal{T}} \left\| \hat{\mathbf{M}}(\mathbf{Y}(t), \mathbf{Y}(s)) - \mathbf{M}(\phi(t), \phi(s)) \right\|_2 = \mathcal{O}(n^{-1/2} \log n) \quad a.s.$$

3.

$$\sup_{t, s \in \mathcal{T}} \left\| \hat{\mathbf{M}}(\mathbf{Y}(t), \mathbf{Y}(s)) \right\|_2 = \mathcal{O}(1) \quad a.s.$$

Proof. We prove each statement in turn.

(1) Since χ and $\phi(t)$ have bounded support, there exists a constant $\beta > 0$ such that $\|\phi(t)\| \leq \beta$ almost surely for all $t \in \mathcal{T}$. By the triangle inequality,

$$\begin{aligned} \left\| \mathbb{E} [(\phi(t) - \phi(s))(\phi(t) - \phi(s))^\top] \right\|_2 &\leq \mathbb{E} \left[\left\| (\phi(t) - \phi(s))(\phi(t) - \phi(s))^\top \right\|_2 \right] \\ &= \mathbb{E} \left[\|\phi(t) - \phi(s)\|^2 \right] \\ &\leq \mathbb{E} [(\|\phi(t)\| + \|\phi(s)\|)^2] \\ &\leq 4\beta^2. \end{aligned}$$

Thus, $\|\mathbf{M}(\phi(t), \phi(s))\|_2$ is finite.

(2) Fix $t, s \in \mathcal{T}$. Define

$$\begin{aligned} \mathbf{A}(i) &:= (\mathbf{Y}_{i:}(t) - \mathbf{Y}_{i:}(s))(\mathbf{Y}_{i:}(t) - \mathbf{Y}_{i:}(s))^\top - \mathbf{M}(\phi(t), \phi(s)) \quad (i = 1, \dots, n), \\ \mathcal{A} &:= \sum_{i=1}^n \mathbf{A}(i). \end{aligned}$$

Then $\mathbb{E}[\mathbf{A}(i)] = 0$, and

$$\hat{\mathbf{M}}(\mathbf{Y}(t), \mathbf{Y}(s)) - \mathbf{M}(\phi(t), \phi(s)) = \frac{1}{n} \sum_{i=1}^n \mathbf{A}(i).$$

Hence, it suffices to show that

$$\|\mathcal{A}\|_2 = \mathcal{O}(n^{1/2} \log n) \quad a.s.$$

Since T is fixed, Applying a union bound over $t, s \in \mathcal{T}$ yields the desired result.

By the triangle inequality and the bounded support assumption (i.e., $\|\phi(t)\| \leq \beta$ almost surely, and similarly for $\mathbf{Y}_{i:}(t)$), we have

$$\|\mathbf{A}(i)\|_2 \leq 8\beta^2 \quad \text{almost surely,} \quad \max \left\{ \left\| \mathbb{E}[\mathcal{A}\mathcal{A}^\top] \right\|_2, \left\| \mathbb{E}[\mathcal{A}^\top \mathcal{A}] \right\|_2 \right\} \leq 64\beta^4 n.$$

Therefore, we may apply the Matrix Bernstein inequality [47] to obtain the stated bound.

(3) By the triangle inequality,

$$\left\| \hat{\mathbf{M}}(\mathbf{Y}(t), \mathbf{Y}(s)) \right\|_2 \leq \left\| \hat{\mathbf{M}}(\mathbf{Y}(t), \mathbf{Y}(s)) - \mathbf{M}(\phi(t), \phi(s)) \right\|_2 + \|\mathbf{M}(\phi(t), \phi(s))\|_2.$$

Taking the supremum over $t, s \in \mathcal{T}$ and combining (1) and (2) yields the claim. \square

Using Lemma J.3, we obtain Proposition F.2.

Proof of Proposition F.2. From Lemma J.3,

$$d_{\text{MV}}(\phi(t), \phi(s)) = \|\mathbf{M}(\phi(t), \phi(s))\|_2^{1/2}$$

is finite for all $t, s \in \mathcal{T}$. By the triangle inequality, we have

$$\begin{aligned} \left| \hat{d}_{\text{MV}}(\mathbf{Y}(t), \mathbf{Y}(s))^2 - d_{\text{MV}}(\phi(t), \phi(s))^2 \right| &= \left| \left\| \hat{\mathbf{M}}(\mathbf{Y}(t), \mathbf{Y}(s)) \right\|_2^2 - \|\mathbf{M}(\phi(t), \phi(s))\|_2^2 \right| \\ &\leq \left\| \hat{\mathbf{M}}(\mathbf{Y}(t), \mathbf{Y}(s)) - \mathbf{M}(\phi(t), \phi(s)) \right\|_2. \end{aligned}$$

Combining this inequality with Lemma J.3 yields the desired result. \square

Next, in order to verify Assumption E.2 for the modified UASE, we again establish consistency of the second-moment matrices. By Theorem 3.3, we derive the following corollary.

Corollary J.4. *Assume Assumption 3.2 holds. Let the modified UASE embeddings $\hat{\mathbf{Y}}(t)$ be defined as Proposition F.3. Then, there exist (possibly random) matrix $\mathbf{W} \in \mathbb{O}(d)$ such that*

$$\sup_{t, s \in \mathcal{T}} \left\| \hat{\mathbf{M}}(\hat{\mathbf{Y}}(t), \hat{\mathbf{Y}}(s)) - \hat{\mathbf{M}}(\mathbf{Y}(t)\mathbf{W}, \mathbf{Y}(s)\mathbf{W}) \right\|_2 = \mathcal{O}\left(n^{-1/2} \log n\right) \quad \text{a.s.}$$

Proof. For notational convenience, define

$$\hat{\Delta}(t, s) = \hat{\mathbf{Y}}(t) - \hat{\mathbf{Y}}(s), \quad \Delta(t, s) = \mathbf{Y}(t) - \mathbf{Y}(s).$$

By Lemma J.3, we have

$$\|\Delta(t, s)\|_2 = n^{1/2} \left\| \hat{\mathbf{M}}(\mathbf{Y}(t), \mathbf{Y}(s)) \right\|_2^{1/2} = \mathcal{O}\left(n^{1/2}\right) \quad \text{a.s.}$$

From Theorem 3.3 and the triangle inequality, we have

$$\sup_{t, s \in \mathcal{T}} \left\| \hat{\Delta}(t, s) - \Delta(t, s)\mathbf{W} \right\|_2 \leq 2 \sup_{t \in \mathcal{T}} \left\| \hat{\mathbf{Y}}(t) - \mathbf{Y}(t)\mathbf{W} \right\|_2 = \mathcal{O}(\log n) \quad \text{a.s.}$$

By the triangle inequality and the submultiplicativity of the spectral norm, we have

$$\begin{aligned} &\left\| \hat{\mathbf{M}}(\hat{\mathbf{Y}}(t), \hat{\mathbf{Y}}(s)) - \hat{\mathbf{M}}(\mathbf{Y}(t)\mathbf{W}, \mathbf{Y}(s)\mathbf{W}) \right\|_2 \\ &= \frac{1}{n} \left\| \hat{\Delta}(t, s)^\top \hat{\Delta}(t, s) - (\Delta(t, s)\mathbf{W})^\top (\Delta(t, s)\mathbf{W}) \right\|_2 \\ &\leq \frac{1}{n} \left(\left\| \hat{\Delta}(t, s)^\top \hat{\Delta}(t, s) - \hat{\Delta}(t, s)^\top (\Delta(t, s)\mathbf{W}) \right\|_2 \right. \\ &\quad \left. + \left\| \hat{\Delta}(t, s)^\top (\Delta(t, s)\mathbf{W}) - (\Delta(t, s)\mathbf{W})^\top (\Delta(t, s)\mathbf{W}) \right\|_2 \right) \\ &\leq \frac{1}{n} \left(\left\| \hat{\Delta}(t, s) - \Delta(t, s)\mathbf{W} \right\|_2 + 2 \|\Delta(t, s)\|_2 \right) \left\| \hat{\Delta}(t, s) - \Delta(t, s)\mathbf{W} \right\|_2 \end{aligned}$$

Thus, we have

$$\sup_{t, s \in \mathcal{T}} \left\| \hat{\mathbf{M}}(\hat{\mathbf{Y}}(t), \hat{\mathbf{Y}}(s)) - \hat{\mathbf{M}}(\mathbf{Y}(t)\mathbf{W}, \mathbf{Y}(s)\mathbf{W}) \right\|_2 = \mathcal{O}\left(n^{-1/2} \log n\right) \quad \text{a.s.}$$

\square

Using Corollary J.4, we obtain Proposition F.3.

Proof of Proposition F.3. By the triangle inequality,

$$\begin{aligned} \left| \hat{d}_{\text{MV}}(\hat{\mathbf{Y}}(t), \hat{\mathbf{Y}}(s))^2 - \hat{d}_{\text{MV}}(\mathbf{Y}(t), \mathbf{Y}(s))^2 \right| &= \left| \left\| \hat{\mathbf{M}}(\hat{\mathbf{Y}}(t), \hat{\mathbf{Y}}(s)) \right\|_2 - \left\| \hat{\mathbf{M}}(\mathbf{Y}(t), \mathbf{Y}(s)) \right\|_2 \right| \\ &\leq \left\| \hat{\mathbf{M}}(\hat{\mathbf{Y}}(t), \hat{\mathbf{Y}}(s)) - \hat{\mathbf{M}}(\mathbf{Y}(t)\mathbf{W}, \mathbf{Y}(s)\mathbf{W}) \right\|_2. \end{aligned}$$

Here we used that $\mathbf{W} \in \mathbb{O}(d)$ preserves the spectral norm.

Combining this bound with Corollary J.4, we conclude that the embeddings $\hat{\mathbf{Y}}(t)$ satisfy Assumption E.2 with $g(n) = n^{-1/2} \log n$. \square

We obtain the node-level to trajectory-level control for MV based trajectories as a direct consequence of the strain bound for CMDS.

Proof of Theorem F.5. Let $\mathbf{Z}_{\text{MV}} := (\hat{\psi}_{\text{MV}}(1), \dots, \hat{\psi}_{\text{MV}}(T))^\top \in \mathbb{R}^{T \times c}$. By the strain bound for CMDS, we have

$$\left\| \hat{\mathbf{E}}_{\text{MV}} - \mathbf{Z}_{\text{MV}} \mathbf{Z}_{\text{MV}}^\top \right\|_F = \left(\sum_{i=c+1}^T \lambda_i \left(\hat{\mathbf{E}}_{\text{MV}} \right)^2 \right)^{1/2}.$$

For any indices $t \neq s$, squared Euclidean distances can be written in terms of inner products as

$$\begin{aligned} \|\hat{\psi}_{\text{MV}}(t) - \hat{\psi}_{\text{MV}}(s)\|^2 &= (\mathbf{Z}_{\text{MV}} \mathbf{Z}_{\text{MV}}^\top)_{tt} + (\mathbf{Z}_{\text{MV}} \mathbf{Z}_{\text{MV}}^\top)_{ss} - 2(\mathbf{Z}_{\text{MV}} \mathbf{Z}_{\text{MV}}^\top)_{ts}, \\ \hat{d}_{\text{MV}}(\hat{\mathbf{Y}}(t), \hat{\mathbf{Y}}(s))^2 &= (\hat{\mathbf{E}}_{\text{MV}})_{tt} + (\hat{\mathbf{E}}_{\text{MV}})_{ss} - 2(\hat{\mathbf{E}}_{\text{MV}})_{ts}. \end{aligned}$$

Taking the difference and applying the triangle inequality yields

$$\begin{aligned} \left| \|\hat{\psi}_{\text{MV}}(t) - \hat{\psi}_{\text{MV}}(s)\|^2 - \hat{d}_{\text{MV}}(\hat{\mathbf{Y}}(t), \hat{\mathbf{Y}}(s))^2 \right| \\ \leq |(\mathbf{Z}_{\text{MV}} \mathbf{Z}_{\text{MV}}^\top - \hat{\mathbf{E}}_{\text{MV}})_{tt}| + |(\mathbf{Z}_{\text{MV}} \mathbf{Z}_{\text{MV}}^\top - \hat{\mathbf{E}}_{\text{MV}})_{ss}| + 2|(\mathbf{Z}_{\text{MV}} \mathbf{Z}_{\text{MV}}^\top - \hat{\mathbf{E}}_{\text{MV}})_{ts}|. \end{aligned}$$

Applying the Cauchy–Schwarz inequality and combining with the strain bound yields

$$\begin{aligned} \left| \|\hat{\psi}_{\text{MV}}(t) - \hat{\psi}_{\text{MV}}(s)\|^2 - \hat{d}_{\text{MV}}(\hat{\mathbf{Y}}(t), \hat{\mathbf{Y}}(s))^2 \right| &\leq 2 \|\mathbf{Z}_{\text{MV}} \mathbf{Z}_{\text{MV}}^\top - \hat{\mathbf{E}}_{\text{MV}}\|_F \\ &\leq 2 \left(\sum_{i=c+1}^T \lambda_i \left(\hat{\mathbf{E}}_{\text{MV}} \right)^2 \right)^{1/2}. \end{aligned}$$

For $s = t$, both squared distances vanish, and the inequality holds trivially.

Finally, recall that

$$\hat{d}_{\text{MV}}(\hat{\mathbf{Y}}(t), \hat{\mathbf{Y}}(s))^2 = \left\| \hat{\mathbf{M}}(\hat{\mathbf{Y}}(t), \hat{\mathbf{Y}}(s)) \right\|_2 = \frac{1}{n} \left\| \hat{\mathbf{Y}}(t) - \hat{\mathbf{Y}}(s) \right\|_2^2$$

Using the variational characterization of the spectral norm, we obtain

$$\hat{d}_{\text{MV}}(\hat{\mathbf{Y}}(t), \hat{\mathbf{Y}}(s))^2 = \frac{1}{n} \sup_{\|\mathbf{u}\|=1} \sum_{i=1}^n \left\{ \left(\hat{\mathbf{Y}}_{i:}(t) - \hat{\mathbf{Y}}_{i:}(s) \right)^\top \mathbf{u} \right\}^2.$$

Moreover, by the standard relation between the spectral and Frobenius norms,

$$\frac{1}{nd} \sum_{i=1}^n \left\| \hat{\mathbf{Y}}_{i:}(t) - \hat{\mathbf{Y}}_{i:}(s) \right\|^2 \leq \hat{d}_{\text{MV}}(\hat{\mathbf{Y}}(t), \hat{\mathbf{Y}}(s))^2 \leq \frac{1}{n} \sum_{i=1}^n \left\| \hat{\mathbf{Y}}_{i:}(t) - \hat{\mathbf{Y}}_{i:}(s) \right\|^2.$$

Combining these bounds completes the proof. \square

We can also obtain a node-level to trajectory-level control for the trajectories based on TV and mode-wise distances.

Proof Sketch of Theorem H.1. As in the proof of Theorem F.5, applying the strain bound for CMDS gives

$$\left| \|\hat{\psi}_{\text{TV}}(t) - \hat{\psi}_{\text{TV}}(s)\|^2 - \hat{d}_{\text{TV}}(\hat{\mathbf{Y}}(t), \hat{\mathbf{Y}}(s))^2 \right| \leq 2 \left(\sum_{i=c+1}^T \lambda_i (\hat{\mathbf{E}}_{\text{TV}})^2 \right)^{1/2}$$

Combining this with the node-level decomposition yields the result. \square

Proof Sketch of Theorem H.2. As in the proof of Theorem F.5, applying the strain bound for CMDS gives

$$\left| \|\hat{\psi}_k(t) - \hat{\psi}_k(s)\|^2 - \hat{d}_k(\hat{\mathbf{Y}}(t), \hat{\mathbf{Y}}(s))^2 \right| \leq 2 \left(\sum_{i=c+1}^T \lambda_i (\hat{\mathbf{E}}_k)^2 \right)^{1/2}$$

Combining this with the node-level decomposition yields the result. \square

Moreover, we establish a tighter bound for the aggregated error.

Proof of Theorem H.3. Let $\mathbf{Z}_{\text{TV}} := (\hat{\psi}_{\text{TV}}(1), \dots, \hat{\psi}_{\text{TV}}(T))^\top \in \mathbb{R}^{T \times c}$. By the same argument as in Theorem F.5, for any indices $t \neq s$,

$$\begin{aligned} & \left| \|\hat{\psi}_{\text{TV}}(t) - \hat{\psi}_{\text{TV}}(s)\|^2 - \hat{d}_{\text{TV}}(\hat{\mathbf{Y}}(t), \hat{\mathbf{Y}}(s))^2 \right| \\ & \leq |(\mathbf{Z}_{\text{TV}} \mathbf{Z}_{\text{TV}}^\top - \hat{\mathbf{E}}_{\text{TV}})_{tt}| + |(\mathbf{Z}_{\text{TV}} \mathbf{Z}_{\text{TV}}^\top - \hat{\mathbf{E}}_{\text{TV}})_{ss}| + 2|(\mathbf{Z}_{\text{TV}} \mathbf{Z}_{\text{TV}}^\top - \hat{\mathbf{E}}_{\text{TV}})_{ts}|. \end{aligned}$$

Let $\mathcal{E} := \mathbf{Z}_{\text{TV}} \mathbf{Z}_{\text{TV}}^\top - \hat{\mathbf{E}}_{\text{TV}}$. Then, by the CauchySchwarz inequality, the squared error satisfies

$$\begin{aligned} \left| \|\hat{\psi}_{\text{TV}}(t) - \hat{\psi}_{\text{TV}}(s)\|^2 - \hat{d}_{\text{TV}}(\hat{\mathbf{Y}}(t), \hat{\mathbf{Y}}(s))^2 \right|^2 & \leq \left(|\mathcal{E}_{tt}| + |\mathcal{E}_{ss}| + |\mathcal{E}_{ts}| + |\mathcal{E}_{st}| \right)^2 \\ & \leq 4 \left(|\mathcal{E}_{tt}|^2 + |\mathcal{E}_{ss}|^2 + |\mathcal{E}_{ts}|^2 + |\mathcal{E}_{st}|^2 \right). \end{aligned}$$

Taking the sum over $t < s$, we get

$$\begin{aligned} & \sum_{t < s} \left| \|\hat{\psi}_{\text{TV}}(t) - \hat{\psi}_{\text{TV}}(s)\|^2 - \hat{d}_{\text{TV}}(\hat{\mathbf{Y}}(t), \hat{\mathbf{Y}}(s))^2 \right|^2 \\ & = \frac{1}{2} \sum_{t \neq s} \left| \|\hat{\psi}_{\text{TV}}(t) - \hat{\psi}_{\text{TV}}(s)\|^2 - \hat{d}_{\text{TV}}(\hat{\mathbf{Y}}(t), \hat{\mathbf{Y}}(s))^2 \right|^2 \\ & \leq 2 \sum_{t \neq s} \left(|\mathcal{E}_{tt}|^2 + |\mathcal{E}_{ss}|^2 + |\mathcal{E}_{ts}|^2 + |\mathcal{E}_{st}|^2 \right) \\ & = 2 \left(\sum_{t \neq s} |\mathcal{E}_{tt}|^2 + \sum_{t \neq s} |\mathcal{E}_{ss}|^2 + \sum_{t \neq s} |\mathcal{E}_{ts}|^2 + \sum_{t \neq s} |\mathcal{E}_{st}|^2 \right) \\ & = 4(T-1) \sum_t |\mathcal{E}_{tt}|^2 + 4 \sum_{t \neq s} |\mathcal{E}_{ts}|^2 \\ & \leq 4(T-1) \|\mathbf{Z}_{\text{TV}} \mathbf{Z}_{\text{TV}}^\top - \hat{\mathbf{E}}_{\text{TV}}\|_F^2, \end{aligned}$$

where we used $T \geq 2$.

Combining with the strain bound and the node-level decomposition yields the result. \square

Proof Sketch of Theorem H.4. The argument follows the same steps as in the proof of Theorem H.3, and the result follows directly. \square

We next verify that the two abstract assumptions required for Theorem E.5 hold for the TV distance.

Proof of Proposition G.2. We first note that

$$d_{\text{TV}}(\phi(t), \phi(s)) = \text{tr} [\mathbf{M}(\phi(t), \phi(s))]^{1/2} \leq d^{1/2} \|\mathbf{M}(\phi(t), \phi(s))\|_2^{1/2}.$$

Combining this with Lemma J.3, we conclude that $d_{\text{TV}}(\phi(t), \phi(s))$ is finite for all $t, s \in \mathcal{T}$. By the triangle inequality,

$$\begin{aligned} & \left| \hat{d}_{\text{TV}}(\mathbf{Y}(t), \mathbf{Y}(s))^2 - d_{\text{TV}}(\phi(t), \phi(s))^2 \right| \\ &= \left| \text{tr} \left[\hat{\mathbf{M}}(\mathbf{Y}(t), \mathbf{Y}(s)) \right] - \text{tr} \left[\mathbf{M}(\phi(t), \phi(s)) \right] \right| \\ &\leq \left| \text{tr} \left[\hat{\mathbf{M}}(\mathbf{Y}(t), \mathbf{Y}(s)) - \mathbf{M}(\phi(t), \phi(s)) \right] \right| \\ &\leq d \left\| \hat{\mathbf{M}}(\mathbf{Y}(t), \mathbf{Y}(s)) - \mathbf{M}(\phi(t), \phi(s)) \right\|_2. \end{aligned}$$

Combining this bound with Lemma J.3 yields the desired result. \square

Proof Sketch of Proposition G.3. By the triangle inequality,

$$\begin{aligned} & \left| \hat{d}_{\text{TV}}(\hat{\mathbf{Y}}(t), \hat{\mathbf{Y}}(s))^2 - \hat{d}_{\text{TV}}(\mathbf{Y}(t), \mathbf{Y}(s))^2 \right| \\ &= \left| \text{tr} \left[\hat{\mathbf{M}}(\hat{\mathbf{Y}}(t), \hat{\mathbf{Y}}(s)) \right] - \text{tr} \left[\hat{\mathbf{M}}(\mathbf{Y}(t), \mathbf{Y}(s)) \right] \right| \\ &= \left| \text{tr} \left[\hat{\mathbf{M}}(\hat{\mathbf{Y}}(t), \hat{\mathbf{Y}}(s)) \right] - \text{tr} \left[\hat{\mathbf{M}}(\mathbf{Y}(t)\mathbf{W}, \mathbf{Y}(s)\mathbf{W}) \right] \right| \\ &= \left| \text{tr} \left[\hat{\mathbf{M}}(\hat{\mathbf{Y}}(t), \hat{\mathbf{Y}}(s)) - \hat{\mathbf{M}}(\mathbf{Y}(t)\mathbf{W}, \mathbf{Y}(s)\mathbf{W}) \right] \right| \\ &\leq d \left\| \hat{\mathbf{M}}(\hat{\mathbf{Y}}(t), \hat{\mathbf{Y}}(s)) - \hat{\mathbf{M}}(\mathbf{Y}(t)\mathbf{W}, \mathbf{Y}(s)\mathbf{W}) \right\|_2. \end{aligned}$$

Here we used that $\mathbf{W} \in \mathbb{O}(d)$ preserves the trace.

Combining this bound with Corollary J.4, we conclude that the embeddings $\hat{\mathbf{Y}}(t)$ satisfy Assumption E.2 with $g(n) = n^{-1/2} \log n$. \square

We also verify that the two abstract assumptions required for Theorem E.5 hold for the mode-wise variation distance. The verification parallels the TV case, with the additional feature that $d_k(\cdot, \cdot)$ depends on a direction (an eigenvector) extracted from an aggregated second-moment matrix.

Accordingly, the proof proceeds in three steps: (1) show finiteness of $d_k(\phi(t), \phi(s))$ by comparing it to the operator norm of $\mathbf{M}(\phi(t), \phi(s))$; (2) control the eigenvector error $\hat{\mathbf{u}}_{\mathbf{Y}}$ versus \mathbf{u}_ϕ via Davis–Kahan once $\hat{\mathcal{M}}_{\mathbf{Y}}$ is close to \mathcal{M}_ϕ ; and (3) combine these ingredients to bound the difference between $\hat{d}_k(\mathbf{Y}(t), \mathbf{Y}(s))^2$ and $d_k(\phi(t), \phi(s))^2$ uniformly.

Proof of Proposition G.7. For notational convenience, define

$$\mathcal{M}_\phi = \sum_{(t,s) \in \mathcal{S}} \mathbf{M}(\phi(t), \phi(s)), \quad \hat{\mathcal{M}}_{\mathbf{Y}} = \sum_{(t,s) \in \mathcal{S}} \hat{\mathbf{M}}(\mathbf{Y}(t), \mathbf{Y}(s)).$$

Let \mathbf{u}_ϕ and $\hat{\mathbf{u}}_{\mathbf{Y}}$ denote the eigenvectors corresponding to the k th largest eigenvalues of \mathcal{M}_ϕ and $\hat{\mathcal{M}}_{\mathbf{Y}}$, respectively. Since both matrices are real symmetric, the eigenvectors are taken to be orthonormal.

First, note that

$$d_k(\phi(t), \phi(s)) = (\mathbf{u}_\phi^\top \mathbf{M}(\phi(t), \phi(s)) \mathbf{u}_\phi)^{1/2} \leq \|\mathbf{M}(\phi(t), \phi(s))\|_2^{1/2},$$

where we used $\|\mathbf{u}_\phi\| = 1$. Combining this with Lemma J.3, we conclude that $d_k(\phi(t), \phi(s))$ is finite for all $t, s \in \mathcal{T}$. By the Davis–Kahan theorem [46],

$$\min_{q=\pm 1} \|\hat{\mathbf{u}}_{\mathbf{Y}} - q\mathbf{u}_\phi\| \leq \frac{2^{3/2} \|\hat{\mathcal{M}}_{\mathbf{Y}} - \mathcal{M}_\phi\|_2}{\min(\lambda_{k-1}(\mathcal{M}_\phi) - \lambda_k(\mathcal{M}_\phi), \lambda_k(\mathcal{M}_\phi) - \lambda_{k+1}(\mathcal{M}_\phi))},$$

with $\lambda_0(\mathcal{M}_\phi) = \infty$, $\lambda_{d+1}(\mathcal{M}_\phi) = -\infty$. By the triangle inequality,

$$\|\hat{\mathcal{M}}_{\mathbf{Y}} - \mathcal{M}_\phi\|_2 \leq \sum_{(t,s) \in \mathcal{S}} \left\| \hat{\mathbf{M}}(\mathbf{Y}(t), \mathbf{Y}(s)) - \mathbf{M}(\phi(t), \phi(s)) \right\|.$$

Lemma J.3 implies that

$$\|\hat{\mathcal{M}}_{\mathbf{Y}} - \mathcal{M}_\phi\|_2 = \mathcal{O}(n^{-1/2} \log n) \quad \text{a.s.}$$

Consequently,

$$\min_{q=\pm 1} \|\hat{\mathbf{u}}_{\mathbf{Y}} - q\mathbf{u}_\phi\| = \mathcal{O}(n^{-1/2} \log n) \quad \text{a.s.}$$

Finally, we bound the discrepancy between the empirical and population quadratic forms defining the k mode distance. By the triangle inequality,

$$\begin{aligned} & \left| \hat{d}_k(\mathbf{Y}(t), \mathbf{Y}(s))^2 - d_k(\phi(t), \phi(s))^2 \right| \\ &= \left| \hat{\mathbf{u}}_{\mathbf{Y}}^\top \hat{\mathbf{M}}(\mathbf{Y}(t), \mathbf{Y}(s)) \hat{\mathbf{u}}_{\mathbf{Y}} - \mathbf{u}_\phi^\top \mathbf{M}(\phi(t), \phi(s)) \mathbf{u}_\phi \right| \\ &\leq \left\| \hat{\mathbf{M}}(\mathbf{Y}(t), \mathbf{Y}(s)) - \mathbf{M}(\phi(t), \phi(s)) \right\|_2 \\ &\quad + \left(\|\mathbf{M}(\phi(t), \phi(s))\|_2 + \left\| \hat{\mathbf{M}}(\mathbf{Y}(t), \mathbf{Y}(s)) \right\|_2 \right) \min_{q=\pm 1} \|\hat{\mathbf{u}}_{\mathbf{Y}} - q\mathbf{u}_\phi\|, \end{aligned}$$

where we used $\|\mathbf{u}_\phi\| = 1$, $\|\hat{\mathbf{u}}_{\mathbf{Y}}\| = 1$.

The first term captures the direct second-moment estimation error, and the second term captures the effect of using $\hat{\mathbf{u}}_{\mathbf{Y}}$ instead of \mathbf{u}_ϕ in the quadratic form; it is scaled by operator norm sizes of the relevant second-moment matrices. Combining these bounds with Lemma J.3 yields the desired result. \square

The next proposition checks the second abstract assumption (Assumption E.2) for the modified UASE embeddings under the mode-wise variation distance. The structure trajectories the MV and TV arguments: we compare the squared k mode dissimilarities by (i) replacing $\hat{\mathbf{Y}}(t)$ with its population aligned counterpart $\mathbf{Y}(t)\mathbf{W}$ inside the second-moment matrices using Corollary J.4, and (ii) controlling the resulting change in the k th eigenvector through Davis–Kahan, using that the associated eigengap stays open under the perturbation.

Proof of Proposition G.8. For notational convenience, define

$$\hat{\mathcal{M}}_{\hat{\mathbf{Y}}} = \sum_{(t,s) \in \mathcal{S}} \hat{\mathbf{M}}(\hat{\mathbf{Y}}(t), \hat{\mathbf{Y}}(s)).$$

Let $\hat{\mathbf{u}}_{\hat{\mathbf{Y}}}$ denote the eigenvectors corresponding to the k th largest eigenvalues of $\hat{\mathcal{M}}_{\hat{\mathbf{Y}}}$. Since $\hat{\mathcal{M}}_{\hat{\mathbf{Y}}}$ is real symmetric, the eigenvectors are taken to be orthonormal.

Since $\mathbf{W} \in \mathbb{O}(d)$, it follows that the eigenvectors corresponding to the k th largest eigenvalues of

$$\sum_{(t,s) \in \mathcal{S}} \hat{\mathbf{M}}(\mathbf{Y}(t)\mathbf{W}, \mathbf{Y}(s)\mathbf{W}) = \mathbf{W}^\top \hat{\mathcal{M}}_{\mathbf{Y}} \mathbf{W}$$

can be chosen as $\mathbf{W}^\top \hat{\mathbf{u}}_{\mathbf{Y}}$, which therefore also form an orthonormal basis. This observation allows us to compare quadratic forms built from $\hat{\mathbf{u}}_{\hat{\mathbf{Y}}}$ and from the rotated vector $\mathbf{W}^\top \hat{\mathbf{u}}_{\mathbf{Y}}$, while keeping the relevant matrices in comparable coordinates.

By the triangle inequality,

$$\begin{aligned} & \left| \hat{d}_k(\hat{\mathbf{Y}}(t), \hat{\mathbf{Y}}(s))^2 - \hat{d}_k(\mathbf{Y}(t), \mathbf{Y}(s))^2 \right| \\ &= \left| \hat{\mathbf{u}}_{\hat{\mathbf{Y}}}^\top \hat{\mathbf{M}}(\hat{\mathbf{Y}}(t), \hat{\mathbf{Y}}(s)) \hat{\mathbf{u}}_{\hat{\mathbf{Y}}} - \hat{\mathbf{u}}_{\mathbf{Y}}^\top \hat{\mathbf{M}}(\mathbf{Y}(t), \mathbf{Y}(s)) \hat{\mathbf{u}}_{\mathbf{Y}} \right| \\ &\leq \left| \hat{\mathbf{u}}_{\hat{\mathbf{Y}}}^\top \hat{\mathbf{M}}(\hat{\mathbf{Y}}(t), \hat{\mathbf{Y}}(s)) \hat{\mathbf{u}}_{\hat{\mathbf{Y}}} - (\mathbf{W}^\top \hat{\mathbf{u}}_{\mathbf{Y}})^\top \hat{\mathbf{M}}(\mathbf{Y}(t)\mathbf{W}, \mathbf{Y}(s)\mathbf{W}) (\mathbf{W}^\top \hat{\mathbf{u}}_{\mathbf{Y}}) \right|. \end{aligned}$$

Here we used that $\mathbf{W} \in \mathbb{O}(d)$. The right hand side compares two quadratic forms: one based on the empirical pair $(\hat{\mathbf{u}}_{\hat{\mathbf{Y}}}, \hat{\mathbf{M}}(\hat{\mathbf{Y}}(t), \hat{\mathbf{Y}}(s)))$ and one based on the population aligned pair $(\mathbf{W}^\top \hat{\mathbf{u}}_{\mathbf{Y}}, \hat{\mathbf{M}}(\mathbf{Y}(s)\mathbf{W}, \mathbf{Y}(t)\mathbf{W}))$.

As in the proof of Proposition G.8, we have

$$\begin{aligned} & \left| \hat{d}_k(\hat{\mathbf{Y}}(t), \hat{\mathbf{Y}}(s))^2 - \hat{d}_k(\mathbf{Y}(t), \mathbf{Y}(s))^2 \right| \\ & \leq \left\| \hat{\mathbf{M}}(\hat{\mathbf{Y}}(t), \hat{\mathbf{Y}}(s)) - \hat{\mathbf{M}}(\mathbf{Y}(t)\mathbf{W}, \mathbf{Y}(s)\mathbf{W}) \right\|_2 \\ & \quad + \left(\left\| \hat{\mathbf{M}}(\mathbf{Y}(t)\mathbf{W}, \mathbf{Y}(s)\mathbf{W}) \right\|_2 + \left\| \hat{\mathbf{M}}(\hat{\mathbf{Y}}(t), \hat{\mathbf{Y}}(s)) \right\|_2 \right) \min_{q=\pm 1} \|\hat{\mathbf{u}}_{\hat{\mathbf{Y}}} - q\mathbf{W}^\top \hat{\mathbf{u}}_{\mathbf{Y}}\|. \end{aligned}$$

This is the same decomposition as in Proposition G.7: a direct matrix perturbation term, plus a term accounting for the perturbation of the eigenvector direction in the quadratic form.

From the proof of Proposition G.7,

$$\|\hat{\mathcal{M}}_{\mathbf{Y}} - \mathcal{M}_\phi\|_2 = \mathcal{O}(n^{-1/2} \log n) \quad \text{a.s.}$$

Hence, by Weyl's inequality, the eigenvalues of $\hat{\mathcal{M}}_{\mathbf{Y}}$ remain strictly separated almost surely. Since $\hat{\mathcal{M}}_{\mathbf{Y}}$ and $\mathbf{W}^\top \hat{\mathcal{M}}_{\mathbf{Y}} \mathbf{W}$ have identical eigenvalues, the eigenvalues of $\mathbf{W}^\top \hat{\mathcal{M}}_{\mathbf{Y}} \mathbf{W}$ also remain strictly separated almost surely. This separation is exactly what is needed to apply Davis–Kahan to compare $\hat{\mathbf{u}}_{\hat{\mathbf{Y}}}$ and $\mathbf{W}^\top \hat{\mathbf{u}}_{\mathbf{Y}}$ once we have an operator norm bound on $\hat{\mathcal{M}}_{\mathbf{Y}} - \mathbf{W}^\top \hat{\mathcal{M}}_{\mathbf{Y}} \mathbf{W}$.

Furthermore, by Lemma J.3,

$$\sup_{t, s \in \mathcal{T}} \left\| \hat{\mathbf{M}}(\mathbf{Y}(t)\mathbf{W}, \mathbf{Y}(s)\mathbf{W}) \right\|_2 = \sup_{t, s \in \mathcal{T}} \left\| \hat{\mathbf{M}}(\mathbf{Y}(t), \mathbf{Y}(s)) \right\|_2 = \mathcal{O}(1) \quad \text{a.s.}$$

Again by Corollary J.4,

$$\sup_{t, s \in \mathcal{T}} \left\| \hat{\mathbf{M}}(\hat{\mathbf{Y}}(t), \hat{\mathbf{Y}}(s)) - \hat{\mathbf{M}}(\mathbf{Y}(t)\mathbf{W}, \mathbf{Y}(s)\mathbf{W}) \right\|_2 = \mathcal{O}(n^{-1/2} \log n) \quad \text{a.s.}$$

Therefore,

$$\begin{aligned} & \sup_{t, s \in \mathcal{T}} \left\| \hat{\mathbf{M}}(\hat{\mathbf{Y}}(t), \hat{\mathbf{Y}}(s)) \right\|_2 = \mathcal{O}(1) \quad \text{a.s.} \\ & \|\mathcal{M}_{\hat{\mathbf{Y}}} - \mathbf{W}^\top \hat{\mathcal{M}}_{\mathbf{Y}} \mathbf{W}\|_2 = \mathcal{O}(n^{-1/2} \log n) \quad \text{a.s.} \end{aligned}$$

Combining these bounds with the Davis–Kahan theorem [46], as in the proof of Proposition G.7, the embeddings $\hat{\mathbf{Y}}(t)$ satisfy Assumption E.2 with $g(n) = n^{-1/2} \log n$. \square

J.6 Change point localization

We control the localization error of the estimated change point by comparing the estimated and population objective functions. Under Assumption H.8, which ensures a linear separation of the population objective around the true change point, together with uniqueness, the localization error of the estimated change point can be controlled. The proof of Theorem 3.9 follows a standard comparison argument: first relate $\hat{Q}(k)$ to $Q(k)$ through the ℓ^2 error between $\hat{\psi}$ and ψ ; then use that \hat{t} minimizes \hat{Q} to compare $Q(\hat{t})$ and $Q(t^*)$; finally invoke Assumption H.8 to convert the result into a bound on $|\hat{t} - t^*|$.

Proof of Theorem 3.9. Fix $k \in \mathcal{K}$ and define

$$\begin{aligned} \theta_k^* & \in \arg \min_{\theta} \sum_{t=1}^T (\psi(t) - \Psi(t; k, \theta))^2 \\ \hat{\theta}_k & \in \arg \min_{\theta} \sum_{t=1}^T (\hat{\psi}(t) - \Psi(t; k, \theta))^2 \end{aligned}$$

By the triangle inequality,

$$\begin{aligned}
& \hat{Q}(k)^{1/2} - Q(k)^{1/2} \\
& \leq \left(\sum_{t=1}^T (\hat{\psi}(t) - \Psi(t; k, \theta_k^*))^2 \right)^{1/2} - \left(\sum_{t=1}^T (\psi(t) - \Psi(t; k, \theta_k^*))^2 \right)^{1/2} \\
& \leq \left(\sum_{t=1}^T (\hat{\psi}(t) - \psi(t))^2 \right)^{1/2}.
\end{aligned}$$

By symmetry,

$$\begin{aligned}
& Q(k)^{1/2} - \hat{Q}(k)^{1/2} \\
& \leq \left(\sum_{t=1}^T (\psi(t) - \Psi(t; k, \hat{\theta}_k))^2 \right)^{1/2} - \left(\sum_{t=1}^T (\hat{\psi}(t) - \Psi(t; k, \hat{\theta}_k))^2 \right)^{1/2} \\
& \leq \left(\sum_{t=1}^T (\psi(t) - \hat{\psi}(t))^2 \right)^{1/2}.
\end{aligned}$$

Hence, for all $k \in \mathcal{K}$,

$$\left| Q(k)^{1/2} - \hat{Q}(k)^{1/2} \right| \leq \left(\sum_{t=1}^T (\hat{\psi}(t) - \psi(t))^2 \right)^{1/2}.$$

This shows that the square root objectives $Q(k)^{1/2}$ and $\hat{Q}(k)^{1/2}$ are uniformly close, with discrepancy controlled by the global ℓ^2 error in the trajectory coordinates.

Since \hat{t} minimizes \hat{Q} , we have

$$\hat{Q}(\hat{t}) \leq \hat{Q}(t^*).$$

Combining the above inequalities yields

$$\begin{aligned}
Q(\hat{t})^{1/2} - Q(t^*)^{1/2} & \leq \left(\hat{Q}(\hat{t})^{1/2} + \left(\sum_{t=1}^T (\hat{\psi}(t) - \psi(t))^2 \right)^{1/2} \right) \\
& \quad - \left(\hat{Q}(t^*)^{1/2} - \left(\sum_{t=1}^T (\hat{\psi}(t) - \psi(t))^2 \right)^{1/2} \right) \\
& \leq 2 \left(\sum_{t=1}^T (\hat{\psi}(t) - \psi(t))^2 \right)^{1/2}.
\end{aligned}$$

Thus, the suboptimality of \hat{t} under the population criterion is controlled by the same ℓ^2 error term.

Next, by the triangle inequality and Assumption H.8, for all $k \in \mathcal{K}$,

$$\begin{aligned}
& Q(k)^{1/2} \\
& = \min_{\theta} \left(\sum_{t=1}^T (\psi(t) - \Psi(t; k, \theta))^2 \right)^{1/2} \\
& \geq \min_{\theta} \left[\left(\sum_{t=1}^T (\Psi(t; t^*, \theta^*) - \Psi(t; k, \theta))^2 \right)^{1/2} - \left(\sum_{t=1}^T (\psi(t) - \Psi(t; t^*, \theta^*))^2 \right)^{1/2} \right] \\
& \geq (\alpha D(\theta^*) |k - t^*|)^{1/2} - Q(t^*)^{1/2}
\end{aligned}$$

The last step uses Assumption H.8 to lower bound the best achievable discrepancy between the true template $\Psi(\cdot; t^*, \theta^*)$ and any misspecified template $\Psi(\cdot; k, \theta)$ in terms of $|k - t^*|$.

Applying this bound at $k = \hat{t}$ and rearranging gives

$$(\alpha D(\theta^*) |\hat{t} - t^*|)^{1/2} - 2Q(t^*)^{1/2} \leq 2 \left(\sum_{t=1}^T (\hat{\psi}(t) - \psi(t))^2 \right)^{1/2},$$

which implies

$$|\hat{t} - t^*| \leq \frac{4}{\alpha D(\theta^*)} \left\{ \left(\sum_{t=1}^T (\hat{\psi}(t) - \psi(t))^2 \right)^{1/2} + Q(t^*)^{1/2} \right\}^2.$$

□

We now verify that Assumption H.8 is satisfied for both 0th and 1st order change points. The proofs of Propositions H.9 and H.10 proceed by fixing a candidate split point k and explicitly minimizing the squared error between the true signal $\Psi(\cdot; t^*, \theta^*)$ and the best approximating template with split at k . In each case, the minimization can be carried out in closed form, and the resulting minimum is bounded below by a constant multiple of $D(\theta^*)|k - t^*|$; the constant is uniform over k because the relevant index sets are finite and the derived expressions are strictly positive.

Proof of Proposition H.9. Fix $k \in \mathcal{K}^{(0)}$ and consider separately the cases $k = t^*$, $k < t^*$ and $k > t^*$.

For $k = t^*$, the inequality holds for any constant $\alpha > 0$.

For $k < t^*$,

$$\begin{aligned} & \min_{\theta} \sum_{t=1}^T \left(\Psi^{(0)}(t; t^*, \theta^*) - \Psi^{(0)}(t; k, \theta) \right)^2 \\ &= \min_{a_L} \sum_{t=1}^{k-1} (a_L^* - a_L)^2 + \min_{a_R} \sum_{t=k}^T \left(\Psi^{(0)}(t; t^*, \theta^*) - a_R \right)^2 \\ &= \min_{a_R} \left[\sum_{t=k}^{t^*-1} (a_L^* - a_R)^2 + \sum_{t=t^*}^T (a_R^* - a_R)^2 \right] \\ &= \frac{(t^* - k)(T - t^* + 1)}{T - k + 1} |a_L^* - a_R^*|^2 \\ &\geq \frac{T - t^* + 1}{T - 1} D(\theta^*) |k - t^*|. \end{aligned}$$

For $k > t^*$,

$$\begin{aligned} & \min_{\theta} \sum_{t=1}^T \left(\Psi^{(0)}(t; t^*, \theta^*) - \Psi^{(0)}(t; k, \theta) \right)^2 \\ &= \min_{a_L} \sum_{t=1}^{k-1} \left(\Psi^{(0)}(t; t^*, \theta^*) - a_L \right)^2 + \min_{a_R} \sum_{t=k}^T (a_R^* - a_R)^2 \\ &= \min_{a_L} \left[\sum_{t=1}^{t^*-1} (a_L^* - a_L)^2 + \sum_{t=t^*}^{k-1} (a_R^* - a_L)^2 \right] \\ &= \frac{(t^* - 1)(k - t^*)}{k - 1} |a_L^* - a_R^*|^2 \\ &\geq \frac{t^* - 1}{T - 1} D(\theta^*) |k - t^*|. \end{aligned}$$

Therefore, Assumption H.8 holds with

$$\alpha := \frac{\min(t^* - 1, T - t^* + 1)}{T - 1} > 0.$$

□

Proof of Proposition H.10. Fix $k \in \mathcal{K}^{(1)}$ and consider separately the cases $k = t^*$, $k < t^*$ and $k > t^*$.

For $k = t^*$, the inequality holds for any constant $\alpha > 0$.

For $k < t^*$,

$$\begin{aligned}
& \min_{\theta} \sum_{t=1}^T \left(\Psi^{(1)}(t; t^*, \theta^*) - \Psi^{(1)}(t; k, \theta) \right)^2 \\
& \geq \min_{a, b_L, b_R} \sum_{t=1}^{k-1} (a^* + b_L^* t - a - b_L t)^2 + \min_{a, b_L, b_R} \sum_{t=k}^T \left(\Psi^{(1)}(t; t^*, \theta^*) - a - b_L k - b_R(t-k) \right)^2 \\
& = \min_{a, b} \left[\sum_{t=k}^{t^*} (a^* + b_L^* t - a - bt)^2 + \sum_{t=t^*+1}^T (a^* + b_L^* t^* + b_R^*(t-t^*) - a - bt)^2 \right] \\
& = \min_{a, b} \left[\sum_{t=k}^{t^*} ((b_L^* - b_R^*)t - a - bt)^2 + \sum_{t=t^*+1}^T ((b_L^* - b_R^*)t^* - a - bt)^2 \right]
\end{aligned}$$

Solving the optimization problem yields the lower bound

$$\frac{x_1 y_1 (y_1 + 1) (2x_1 y_1 + x_1 - y_1 + 1)}{6z_1 (z_1^2 - 1)} D(\theta^*) |t^* - k|,$$

where

$$\begin{aligned}
x_1 &= t^* - k + 1 \geq 2, \\
y_1 &= T - t^* \geq 1, \\
z_1 &= T - k + 1 \geq 3.
\end{aligned}$$

For fixed $t^* \in \{3, \dots, T-1\}$, define

$$\alpha_1 := \min_{2 \leq k \leq t^*} \frac{x_1 y_1 (y_1 + 1) (2x_1 y_1 + x_1 - y_1 + 1)}{6z_1 (z_1^2 - 1)}$$

Since the index set is finite and the expression is strictly positive, we have $\alpha_1 > 0$.

For $k > t^*$,

$$\begin{aligned}
& \min_{\theta} \sum_{t=1}^T \left(\Psi^{(1)}(t; t^*, \theta^*) - \Psi^{(1)}(t; k, \theta) \right)^2 \\
& \geq \min_{a, b_L, b_R} \sum_{t=1}^k \left(\Psi^{(1)}(t; t^*, \theta^*) - a - b_L t \right)^2 \\
& \quad + \min_{a, b_L, b_R} \sum_{t=k+1}^T (a^* + b_L^* t^* + b_R^*(t-t^*) - a - b_L k - b_R(t-k))^2 \\
& = \min_{a, b} \left[\sum_{t=1}^{t^*} (a^* + b_L^* t - a - bt)^2 + \sum_{t=t^*+1}^k (a^* + b_L^* t^* + b_R^*(t-t^*) - a - bt)^2 \right] \\
& = \min_{a, b} \left[\sum_{t=1}^{t^*} ((b_L^* - b_R^*)t - a - bt)^2 + \sum_{t=t^*+1}^k ((b_L^* - b_R^*)t^* - a - bt)^2 \right]
\end{aligned}$$

Solving the optimization problem yields the lower bound

$$\frac{x_2 y_2 (y_2 + 1) (2x_2 y_2 + x_2 - y_2 + 1)}{6z_2 (z_2^2 - 1)} D(\theta^*) |t^* - k|,$$

where

$$\begin{aligned}x_2 &= t^* \geq 2, \\y_2 &= k - t^* \geq 1, \\z_2 &= k \geq 3.\end{aligned}$$

For fixed $t^* \in \{2, \dots, T-2\}$, define

$$\alpha_2 := \min_{t^*+1 \leq k \leq T-1} \frac{x_2 y_2 (y_2 + 1) (2x_2 y_2 + x_2 - y_2 + 1)}{6z_2 (z_2^2 - 1)}$$

Since the index set is finite and the expression is strictly positive, we have $\alpha_2 > 0$.

Therefore, Assumption H.8 holds with

$$\alpha := \begin{cases} \alpha_2, & t^* = 2, \\ \min\{\alpha_1, \alpha_2\}, & 2 < t^* < T-1, \\ \alpha_1, & t^* = T-1. \end{cases}$$

□